Quantum Effects in Classical Backgrounds: Dark Matter Superfluidity and Coherent States

Giordano Cintia

München 2023

Quantum Effects in Classical Backgrounds: Dark Matter Superfluidity and Coherent States

Giordano Cintia

Dissertation
an der Fakultät für Physik
der Ludwig–Maximilians–Universität
München

vorgelegt von
Giordano Cintia
aus Marsciano, Italien

München, den 23. Oktober 2023

Erstgutachter: Prof. Dr. Gia Dvali
Zweitgutachter: Priv.-Doz. Dr. Ralph Blumenhagen
Tag der mündlichen Prüfung: 6. Dezember 2023

This thesis is based on the author's work carried out at the Max Planck Institute for Physics (Werner-Heisenberg-Institut) in Munich under the day-to-day supervision of Dr Lasha Berezhiani. Parts of this thesis are based on the following papers:

1. "Core fragmentation in simplest superfluid dark matter scenario",
   L. Berezhiani, G. Cintia and M. Warkentin, Phys. Lett. B **819** (2021)'

2. "Background-field method and initial-time singularity for coherent states",
   L. Berezhiani, G. Cintia and M. Zantedeschi, Phys. Rev. D **105** (2022) no.4

3. "Thermalization, Fragmentation and Tidal Disruption: The Complex Galactic Dynamics of Dark Matter Superfluidity",
   L. Berezhiani, G. Cintia and J. Khoury, Phys. Rev. D **107** (2023), no.12

4. L. Berezhiani, G. Cintia and M. Zantedeschi, *in prep.*

The authors of these papers share the principal authorship and are listed alphabetically as it is conventional in high-energy physics.

Other articles, which are in preparation and which content was produced during the doctoral period, are

1. L. Berezhiani, G. Cintia, V. De Luca and J. Khoury, *in prep.*

2. L. Berezhiani, G. Cintia, *in prep.*

Contents

List of Figures

Zusammenfassung

Klassische Feldkonfigurationen sind in der Grundlagenphysik häufig anzutreffen. Obwohl die ultimative Beschreibung eines Systems quantenbasiert ist, sind klassische Hintergründe recht genau für die Beschreibung von Zuständen mit hoher Belegung und sie sind von zentraler Bedeutung für eine Vielzahl von Phänomenen, von der Kosmologie des frühen Universums bis zur Astrophysik. Daher ist diese Arbeit der umfassenden Untersuchung verschiedener phänomenologischer und theoretischer Aspekte im Zusammenhang mit dieser Klasse von Systemen gewidmet.

Im ersten Teil dieser Arbeit untersuchen wir die Auswirkungen einer supraflüssigen Phase der dunklen Materie auf die Entstehung und Entwicklung von Halos aus dunkler Materie. Obwohl das Standardparadigma der kalten dunklen Materie (Cold Dark Matter, CDM) erfolgreich auf großräumige Beobachtungen eingeht, tauchen mehrere offene Probleme auf, wenn der Rahmen auf die Dynamik von Galaxien angewendet wird. Die Diskrepanz zwischen den Eigenschaften von galaktischen Halos, die aus CDM-Simulationen gewonnen werden, und den und den aus Beobachtungen abgeleiteten Eigenschaften ist allgemein als *small-scale problems* bekannt. Motiviert durch diese Probleme untersuchen wir die Phänomenologie der einfachsten Modells superflüssiger dunkler Materie, die Theorie eines Skalarfeldes mit abstoßenden quartischen Selbstwechselwirkungen ist. Wenn die dunkle Materie aus sub-eV Skalarbosonen besteht, zeigen wir, dass neue emergente kollektive Phänomene diese Diskrepanzen verkleinern können.

Der zweite Teil der Arbeit ist dem Verständnis kohärenter Zustände in wechselwirkenden Quantenfeldtheorien gewidmet. Dieser Teil zielt darauf ab, eine Verbindung zwischen der semiklassischen Näherung, die üblicherweise zur Untersuchung hochbesetzter Systeme verwendet wird, und der vollständigen Quantendynamik herzustellen. Indem wir uns auf die Theorie eines skalaren Feldes mit quartischen Wechselwirkungen konzentrieren, untersuchen wir die Auswirkungen, die kumulative Quanteneffekte auf die Dynamik kohärenter Zustände haben können. Wir zeigen, dass die klassischen Hintergründe dieser Theorie keine Gleichgewichtskonfigurationen sind, da sie dazu neigen, durch die Annihilation von Quantenbestandteilen mit Nullimpuls in relativistische Teilchen erschöpft zu werden. Dieses Ergebnis wird durch die Berechnung der zeitlichen Entwicklung der Ein-Punkt-Funktion des Feldoperators für nicht gequetschte kohärente Zustände, die homogene Konfigurationen beschreiben, gefunden. Während diese Ergebnisse zuvor mit Hilfe der S-Matrix-Analyse abgeleitet wurden, bestätigen wir sie in diesem Teil mit Hilfe des Schwinger-Keldish-Formalismus.

Außerdem diskutieren wir das Problem der anfänglichen Zeitsingularitäten, die kohärente Zustände beeinflussen. Dabei handelt es sich um eine Reihe von Divergenzen, die in den Korrelationsfunktionen auftreten und die nicht durch Renormierung der Theorie beseitigt wer-

den können. Die wichtigste Auswirkung dieser Pathologien ist, dass nicht gequetschte kohärente Zustände als konsistente Zustände in wechselwirkenden Quantenfeldtheorien abgetan werden müssen, zumindest bei perturbativen Berechnungen. Schließlich zeigen wir, dass dieselben Schlussfolgerungen auch für kohärente Zustände mit *Quetschungen* gelten. Obwohl diese Zustände die anfängliche Zeitsingularität bei der ersten Schleifenordnung in der semiklassischen Expansion beheben, aber bei höheren Ordnungen gelingt ihnen dies nicht. Nur durch die Betrachtung nicht-gaußscher Zustände kann diese Klasse von Divergenzen beseitigt werden.

Abstract

Classical field configurations are frequently encountered in fundamental physics. Although the ultimate description of a system is quantum, classical backgrounds are quite accurate for describing states of high occupancy and they are of central importance in a variety of phenomena, from early universe cosmology to astrophysics. Therefore, this thesis is dedicated to the comprehensive investigation of various phenomenological and theoretical aspects associated with this class of systems.

In the first part of this thesis, we study the effects that a superfluid phase of dark matter has on the formation and evolution of dark matter halos. Although the standard Cold Dark Matter (CDM) paradigm successfully addresses large-scale observations, several open problems emerge when the framework is applied to the dynamics of galaxies. The mismatch between the properties of galactic halos obtained from CDM simulations and the ones inferred from observations is commonly known as *small-scale problems*. Motivated by these issues, we study the phenomenology of the simplest dark matter superfluid, which is the theory of a scalar field with repulsive quartic self-interactions. If dark matter is comprised of sub-eV scalar bosons, we show that new emergent collective phenomena can ameliorate these challenges.

The second part of the thesis is devoted to understanding coherent states in interacting quantum field theories. By focusing on the theory of a *real* scalar field with quartic interactions, we investigate the implications that cumulative quantum effects can have on the dynamics of coherent states. We show that the classical backgrounds of this theory are not equilibrium configurations, as they are prone to be depleted by the annihilation of zero momentum quantum constituents into relativistic particles. This result is found by computing the time-evolution of the one-point function of the field operator, for non-squeezed coherent states describing homogeneous configurations. While these findings were previously derived using the S-matrix analysis, in this part we confirm them using the Schwinger-Keldish formalism.

Also, we discuss the issue of initial time singularities that affect coherent states. These are a set of divergences that appear in the correlation functions and that cannot be removed by renormalizing the theory. The main implication of these pathologies is that non-squeezed coherent states have to be dismissed as consistent states in interacting quantum field theories, at least in perturbative computations. Finally, we show that the same conclusions apply to *squeezed* coherent states. Although these states can address the initial time singularity at the one-loop order in the semiclassical expansion, they fail to do that at higher orders. Only by considering non-gaussian states, this class of divergences can be removed.

Chapter 1

Dark Matter and Small Scale Structures

Cosmological and astrophysical observations show that 26% of the energy density in our Universe consists of Cold Dark Matter [1]. The ΛCDM model, in which dark matter is introduced as a cosmological pressure-less fluid, is in very good agreement with observations, enabling the accurate modelling of large-scale structure formation [2] and of the temperature anisotropies in the Cosmic Microwave Background [1].

Nevertheless, several problems are encountered when the framework is applied to galactic scales, where certain puzzles emerge when predictions from N-body simulations of collisionless dark matter are compared to observations. Before delving into the possible solutions to these discrepancies, we dedicate this section to explaining two of the main problems we are going to discuss in the rest of this thesis: the core-cusp problem and the excess of substructures predicted by ΛCDM [3].

1.1 The Core-cusp problem

In the ΛCDM model, quantum primordial fluctuations generated during cosmic inflation are stretched on cosmological scales, becoming the seeds of the inhomogeneous structure we detect today. Once these fluctuations reenter the horizon, they recollapse. The outcome of this process on small scales are *Virialized halos*, which are overdense regions with an enclosed mass of

$$M = \frac{4\pi}{3} R_{\rm vir}^3 \delta \, \rho_m. \tag{1.1}$$

Here, $\delta \sim 200$ is the virial overdensity parameter, which defines the average density of the halo once compared to the background cosmological density. It is important to note that the definition (1.1) carries a degree of arbitrariness, as it relies on the specific value of the parameter δ. The value $\delta \sim 200$ is chosen to match the theoretical virialized overdensity obtained from an ideal spherical collapse of a dark matter region [4]. Additionally, this relation provides the

conventional definition of the "virial radius," denoted as $R_{\rm vir}$, which is typically regarded as the characteristic size of the halo.

The formation of small-scale structures is a highly non-linear problem, which is usually approached numerically. N-body simulations of collisionless dark matter predict that the density distribution of dark matter halos is expected to have an almost linear scaling in inner regions, according to the phenomenological law [5]

$$\rho(r) \sim r^{-\gamma}, \qquad \text{with} \qquad \gamma \sim 0.8 - 1.4 \tag{1.2}$$

and gets steeper outside. Different phenomenological density distributions can interpolate between the scaling of inner and outer regions. The most famous one is the Navarro-Frank-White profile [6]

$$\rho_{\rm nfw}(r) = \frac{\rho_0}{\frac{r}{r_s}\left(1+\frac{r}{r_s}\right)^2}. \tag{1.3}$$

Here, ρ_0 is the characteristic density parameter of the halo and r_s is the scale radius. The latter is usually connected to the virial radius by the concentration parameter $c = R_{\rm vir}/r_s$, which in turn is connected to ρ_0 by the phenomenological mass-to-concentration relation [7]. Although the profile (1.3) provides a fairly good fit for the density distribution of simulated halos, several alternatives [8–11] can be considered as well. However, for the sake of the discussion in this thesis, the NFW profile is sufficient for providing a qualitative picture of the phenomenology of small-scale structures.

While simulations can accurately describe clusters and large galaxies, they often exhibit significant discrepancies when it comes to dwarf galaxies, where they overpredict the central density of halos and incorrectly depict the slope of the dark matter density distribution, particularly in central regions. It is usually stated that simulations tend to favour dark matter halos which are dense and cuspy, although observations often indicate that certain density distributions are better described by central cores. An example illustrating this can be found in Figure 1.1, which presents the rotation curves of various dwarf galaxies [12]. The coloured dots represent the observed data points, while the black (coloured) solid lines depict the corresponding simulated rotation curves obtained from cosmological hydrodynamical simulations, without (with) baryons. The panel showcases a group of dwarf galaxies whose density distribution from simulations deviates significantly from the observed data. We see that the reconstructed rotation curves display diverse shapes compared to simulations. Also, simulated halos show a consistent overabundance of dark matter at small radii [12].

Finally, let us briefly discuss possible solutions to these discrepancies that can be found within the ΛCDM model itself. It is claimed that the feedback from the collective baryonic effects in galaxies can drastically change the density profile of halos, compared to dark-matter-only simulations. Hydrodynamical simulations have shown the importance of these effects in modelling the central region of halos, where supernovae energy [13–16] and density fluctuations induced by star formation [17–20] can stimulate the formation of cores. In fact, the ejection of baryonic matter reduces the gravitational force, consequently allowing the halo to expand, resulting in a shallow central core. Halos with an efficient star formation are notably impacted, exhibiting significant deviations from simulations of standard cold dark matter. In contrast, halos

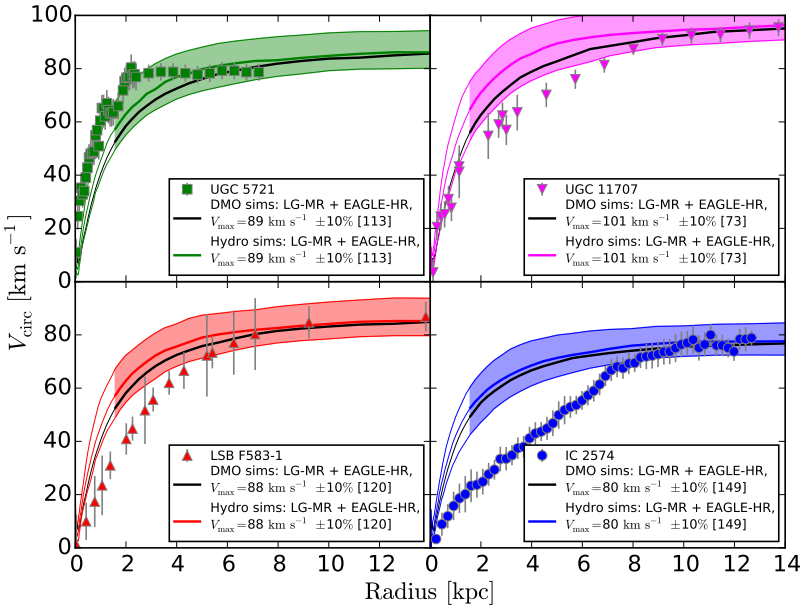

Figure 1.1: Rotation curves of four irregular dwarf galaxies [12]. Coloured dots represent data points, while solid lines are rotation curves obtained from hydrodynamical simulation, with the black (coloured) lines representing simulation without (with) baryons. As we can see, there is a mismatch of simulated rotation curves with respect to the observed ones.

with minimal baryonic content tend to evolve in alignment with the predictions of standard cold dark matter simulations. Therefore, the main signature of these effects is the correlation between the properties of the core and the cumulative mass of stars formed in the halo [21, 22]. However, in light of this correlation, it seems difficult to explain the dynamics of Low Surface Brightness galaxies, which are galaxies mostly comprised of dark matter. Although poor in baryons, these galaxies present density distributions which deviates significantly from CDM predictions, as in the case of the dwarf galaxy IC2574 depicted in Fig. 3.5.

1.2 Missing satellites and "too big-to-fail"

The halo mass function quantifies the number of halos $dN_{\rm halo}$ within a specific mass interval $dM_{\rm halo}$ and it provides a robust prediction of simulations within ΛCDM. A noteworthy feature is that, as we increase the mass of resolved subhalos, the mass function consistently exhibits a monotonic decrease across all discernible mass ranges. In particular, it predicts that a Milky-Way-like galaxy should be the host of $\sim 10^3$ subhalos, with a mass bigger than $M \gtrsim 10^7 M_\odot$ [23–25] (See also black and grey lines of Figure 1.2).

However, this property is in discrepancy with the observed number of satellites orbiting in the Milky Way, where approximately 50 satellites within the first 300 kpc from the galactic centre have been detected, with the lighter resolved one with a mass of $M \sim 300 M_\odot$ [27]. This mismatch gives the name to the famous *Missing Satellite Problem*, namely that the inferred mass

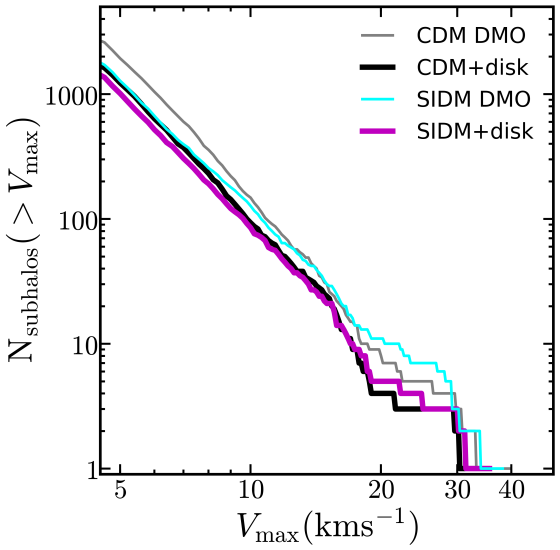

Figure 1.2: Figure from [26]: number of subhalos at redshift $z = 0$ above a given maximum subhalo circular velocity $V_{\rm max}$, as a function of $V_{\rm max}$. Notice that the square of the maximum circular velocity can be linearly related to the mass of the subhalo. The grey and black lines provide the number of subhalo from simulations of Cold Dark matter, without and with baryons respectively. Cyan and Magenta lines represent the subhalo abundance in models of Self-interacting Dark Matter, without and with the effect of baryons respectively.

function is not as steep as the one predicted by simulations. Although in recent years more faint satellites have been discovered and it remains plausible that a lot more can be detected in the next years, it is unlikely that this huge discrepancy in the abundance can be fully reconciled without a further understanding of the model.

In this direction, an important point to consider is that less massive subhalos might be highly inefficient in forming stars, rendering them completely dark. This possibility is supported by semi-analytic models of galaxy formation, where supernova feedback and ultraviolet (UV) background from reionization are extremely efficient in limiting the formation of stars in low-mass halos [28–33]. In the first case, if the supernova energy couples to the galactic medium, it can remove the baryonic content from the centre of the halo, regulating, or even quenching, star formation [34, 35]. Concerning the latter instead, UV-background originated during the phase of reionization of the universe can heat up the baryonic content, preventing its collapse [36–41]. Therefore, in this context, the issue of missing satellites can be reframed as the challenge of understanding under what conditions the simulated subhalos can efficiently support star formation and, by extension, become detectable.

However, in the past years, this approach also highlighted a third shortcoming of the ΛCDM model. High-resolution N-body simulations of Milky Way-like galaxies reveal that the most massive dark matter subhalos within the host galaxy exhibit central densities which are significantly higher than those associated with the satellites inhabiting the Milky Way. In other words, this result suggests that galaxies should be able to form in less massive halos, such as the ones found

in the Milky Way, but fail to do so in the most massive halos, hence the name *too-big-to-fail* problem [42, 43].

1.3 Alternative models of dark matter

Although a better understanding of the physics of baryons is important to characterize the evolution of dark matter halos, it is still unclear if this can be enough to overcome the problems highlighted before. This is particularly true for certain tight phenomenological scaling relations that do exist between the dark matter and baryon properties of halos. An example of this is the baryonic Tully-Fisher relation [44], which correlates the baryonic content of the halo with its asymptotic circular velocity, as

$$M_{\rm bar} \sim V_{\rm max}^4. \tag{1.4}$$

The peculiarity of this relation is that it holds for an extremely wide range of halo masses, from clusters down to extremely faint sub-halos which are dark matter-dominated. Although it was claimed that certain scaling relations between dark matter and baryons should be present also for ΛCDM [45], the extension to low-mass halos is still challenging to reproduce.

Motivated by this, in this thesis we explore a complementary approach to ameliorate or overcome the aforementioned small-scale problems. In contrast to focusing on the baryonic sector, we highlight that introducing additional properties to dark matter, which are effective at galactic scales, can lead to a more favourable galactic-scale behaviour. The main assumption we want to challenge is that the collision-less and pressure-less fluid approximation remains valid down to galactic scales. Specifically, if dark matter can source a positive pressure that is effective only on scales smaller than a few kiloparsecs, this has the potential to significantly influence the dynamics of dark matter in dense regions of halos, such as the core, and to damp the formation of substructures.

The way these effects are introduced depends on the model at hand. One of the most popular proposals is Self-Interacting Dark Matter (SIDM) [46], where the standard weakly interacting massive paradigm is modified by introducing self-interactions among dark matter particles. By choosing a scattering cross section of order $\sigma/m \lesssim 1\ \mathrm{cm}^2/g$, scatterings may drive a dark matter redistribution from inner to outer regions, alleviating the central cusp of the NFW profile. While maintaining the successes of Cold Dark Matter on large scales, Self-Interacting Dark Matter is capable of reproducing certain shapes of rotation curves observed in dwarf galaxies [47–49]. It also ameliorates the too-big-too-fail problem observed in the Milky Way, Andromeda, and the Local Group [26] and, in the absence of baryons, it can suppress the formation of subhalos in dark-matter-only simulations (as depicted in Fig.1.2).

A second widely studied possibility is that the wave nature of particles becomes important at galactic scales so that the approximation of dark matter as a classical fluid breaks down. This case is described by models of Fuzzy Dark Matter (FDM) [50, 51]. By introducing a dark matter field with a mass of $m \simeq 10^{-21}$ eV, the wave properties of particles become important on the kpc-scale. In particular, due to the Heisenberg uncertainty principle, it becomes inefficient confining particles below their de Broglie wavelength $\lambda_{\rm db} \sim (mv)^{-1}$. The manifestation of this property is the *quantum pressure*, a statistical pressure of quantum origin which quantifies these effects. We

discuss more in detail this class of model in Chapter 3. The main phenomenological implication of Fuzzy Dark Matter is the suppression of substructures below the scale $\lambda_{\rm db}$, as well as the formation of cores in inner regions of halos of the same peculiar size. See [52, 53] for recent numerical studies.

However, in this thesis, we focus on a third scenario, which lies at the intersection between these two. In particular, we study the phenomenology of a sub-eV dark matter candidate with self-interactions, capable of undergoing a superfluid phase transition in galactic halos [54–56]. We discuss how a sub-eV dark matter field, if assisted by self-interactions, is capable of generating an interesting phenomenology at galactic scales, which can ameliorate the core-cusp problem and also the excess of substructures, similar to the model of SIDM and FDM. However, before discussing this scenario in Chapter 3, we dedicate the next chapter to reviewing the theory of superfluidity.

Chapter 2

Superfluidity

This chapter is dedicated to reviewing the effective field theory of Superfluidity, a crucial tool that we use in the next chapter for understanding the behaviour of a superfluid phase of dark matter in the galactic environment.

Superfluidity is a set of remarkable hydrodynamic properties that certain fluids exhibit when cooled below a certain critical temperature. One of its most notable features is the phenomenon of *superflow*, which was observed for the first time in 1937 by P. Kapitza [57] and independently by J.F. Allen and A.D. Misener [58] in liquid helium. They observed that when helium is cooled below 2.17 K, it develops a frictionless flow, allowing it to move seamlessly through narrow capillaries without dissipating energy.

This chapter provides a comprehensive overview of the low-energy dynamics of superfluids at zero temperature. Specifically, we describe how the macroscopic properties of a superfluid arise from its low-energy spectrum of perturbations, the *phonon spectrum*, according to Landau's theory of superfluidity. In turn, we review how the nature of these perturbations is a collective quantum effect, with phonons emerging as the gapless excitations of the interacting Bose-Einstein condensate that the superfluid constituents form below a certain critical temperature.

2.1 A macroscopic description: the two-fluid model

The pioneering work of Fritz London was the first to connect the frictionless phenomenology of a superfluid to the microscopic behaviour of its constituents [59]. London proposed that the macroscopic phenomenology of superfluids could be the result of the Bose-Einstein condensation of Helium atoms at a microscopic level. This idea was based on the observation that quantum fluctuations become the dominant contribution to the kinetic energy of liquid Helium below the superfluid critical point. Although this initial attempt did not explain the emergence of dissipationless flow, it laid the groundwork for understanding superfluidity as a macroscopic quantum effect [60].

The idea of Bose-Einstein condensation was further developed in the *two-fluid model of superfluidity*, first proposed by L. Tisza [61]. At temperatures below a critical point T_c, a portion $n_{\rm sf}$

of the total number density of Helium atoms undergoes condensation into the ground state via a Bose-Einstein condensation, while the remaining density n_{norm} is distributed among excited states. The ratio of these two components is a function of the temperature

$$\frac{n_{\text{norm}}}{n_{\text{sf}}} = \left(\frac{T}{T_c}\right)^s . \tag{2.1}$$

The value of s depends on the specific system of interest, with $s = 3/2$ reproducing the temperature dependence of the normal component for an ideal gas, while larger values of s are expected for strongly interacting systems. Equation (2.1) suggests that the system can be effectively treated as a mixture of two fluids, with a normal component of density n_{norm} and a superfluid component of density n_{sf}. Only the normal component would experience a dissipative motion while the superfluid component, being effectively at zero temperature, is collisionless.

In 1941, L. Landau [62] introduced a revised and corrected version of the two-fluid model. Landau's main objection to Tisza's model was that liquid helium could not be regarded as an ideal gas. He argued that self-interactions play a significant role in the dynamics of the two fluids. For example, the non-interacting approximation is inadequate in explaining why the superfluid component does not encounter friction when flowing through a capillary, considering that relative motion typically results in interactions between the helium atoms in the condensed phase and the walls of the capillary.

By giving up any microscopic interpretation, Landau proposed a description of superfluidity in terms of *phonons*, the low-energy excitations of the superfluid component[1]. While retaining Tisza's conceptual framework of a coexisting normal component and a superfluid component in finite-temperature superfluid helium, Landau described the dynamics of the system only in terms of the low-energy excitation of the superfluid. In other words, according to Landau's picture, the minimal excitation of a superfluid is not a single Helium atom, but a long-wavelength excitation of the system. With this substitution, Landau was able to qualitatively account for the self-interacting nature of the helium fluid. It is worth noting that Landau's model does not require condensation as a fundamental ingredient. The treatment is done by quantizing the long-wavelength perturbations of the fluid and the dispersion of those perturbations is taken as input from experiments. However, Bose-Einstein condensation provides a theoretical basis for why phonons have the experimentally observed spectrum, as shown by N.N Bogolyubov [63] in 1946.

For the upcoming discussions, the qualitative intuition from the two-fluid model is sufficient, as the superfluids discussed in the following sections can be approximated to have zero temperature. We redirect the reader to the following review [64] for a more quantitative discussion of the two-fluid model. Before moving to the description of superfluidity in terms of the modern effective field theory language, let us derive the frictionless behaviour of the superfluid component from the phenomenology of its low-energy perturbations, according to Landau's approach. A fluid moving in a capillary with a velocity $\vec{v}_s$ carries, in the rest frame of the capillary itself, an energy

$$E = E_{\text{kin}} + \omega_k + \vec{k} \cdot \vec{v}_s, \tag{2.2}$$

[1] Landau's two-fluid model describes the normal fluid component in terms of *phonon* and *roton* degrees of freedom since it was applied to explain superfluidity of liquid helium.

where ω_k and $\vec{k}$ are the energy and momentum of an excitation, while $E_{\rm kin}$ is the kinetic energy of the fluid. In order to have a frictionless motion, the relative velocity has to satisfy the condition

$$v_s < \min_k \frac{\omega_k}{k}. \tag{2.3}$$

In this way, the combination $\omega_k + \vec{k} \cdot \vec{v}_s$ is always positively defined and no dissipation can take place in the fluid. In order for the system to experience superfluidity, condition (2.3) implies that any energy excitation has to satisfy

$$\lim_{k\to 0} \omega_k \simeq \gamma k^m, \qquad \text{with} \quad m \leq 1. \tag{2.4}$$

If this condition is not satisfied, any arbitrary small v_c can excite an arbitrary weak perturbation of the condensate, allowing a dissipation. It is straightforward to check that the perturbations of superfluid Helium (See Fig. 2.1) satisfy the condition (2.3). In particular, the phonon dispersion relation reads

$$\omega_k \simeq c_s k, \qquad c_s = \frac{\partial P}{\partial \rho}, \tag{2.5}$$

where c_s is the sound speed of the system. In terms of them, condition (2.3) reads

$$v_s < c_s \qquad \rightarrow \qquad \text{no dissipation.} \tag{2.6}$$

This is the famous *Landau's criterion for superfluidity*, which states that a superfluid experiences a superflow if the relative velocity of the external perturbation and the fluid is smaller than the sound speed of the system.

2.2 The low energy effective field description of superfluidity

While providing a qualitative picture of a superfluid in terms of its *long-wavelength perturbations*, the two-fluid model does not address either the origin of the spectrum of the perturbations or the role that the *constituent particles of the system* have in the phase transition itself.

The rest of this chapter is devoted to understanding superfluidity from the quantum field theory point of view. At the microscopic level superfluidity is deeply connected to the concept of *Bose-Einstein condensation*. Given a system of bosons, a superfluid can be described by a field configuration which spontaneously breaks time-translation and the $U(1)$ symmetry of the system[2]. Also, constituent particles must interact through repulsive interactions for the system to experience superfluidity. Only in this way, phonons can be identified as the *Goldstone boson* of the spontaneously broken symmetries of the system and the macroscopic superfluid phenomenology can be reproduced correctly.

[2]Here, we have in mind a system of complex scalar bosons. However, the same result can be obtained by considering real bosons, since in the non-relativistic limit the number of particles is conserved.

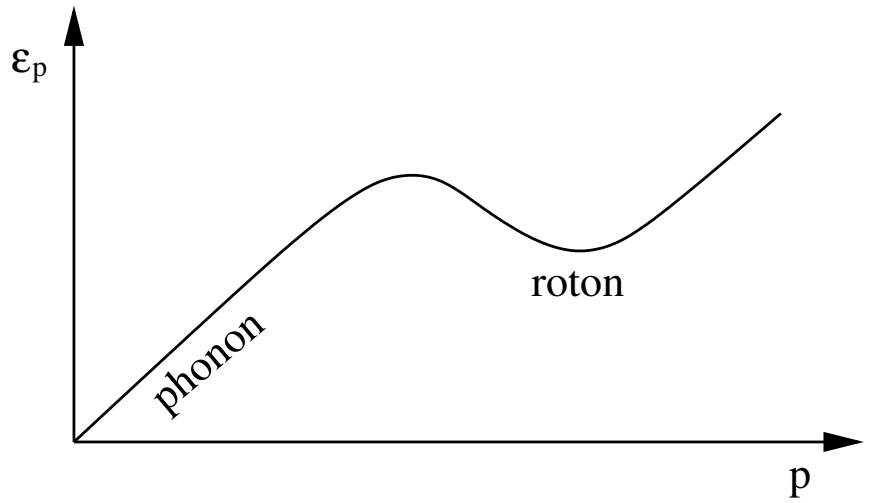

Figure 2.1: Figure from the review [64], which shows the spectrum of perturbations of Superfluid Helium as a function of the transferred momentum p. On the left of the maximum, there is the phonon part of the spectrum, characterized by linear dependence on momentum. The region around the minimum is the roton part of the spectrum, which is quadratically dependent on the momentum.

2.2.1 A pedagogical example: quartic superfluids

The simplest example of a superfluid is a system of two-body interacting scalar bosons. Following the review of [64, 65], we introduce a complex scalar field Φ endowed by a quartic potential

$$\mathcal{L} = \partial_\mu \Phi^+ \partial^\mu \Phi - m^2 |\Phi|^2 - \frac{\lambda}{2} |\Phi|^4 . \tag{2.7}$$

Notice that interactions have to be *repulsive* for the system to experience superfluidity. The field configuration corresponding to the superfluid solution is hence given by

$$\Phi = V e^{i\mu t}, \tag{2.8}$$

where the parameter μ is the *relativistic chemical potential of the system*. In particular, the configuration (2.8) is a solution of the field equation as long as μ satisfies the relation

$$\mu^2 = m^2 + \lambda V^2. \tag{2.9}$$

The parameter V is the *order parameter* of the solution. It is connected to the total number of particles of the system by the relation

$$n = 2\mu V^2, \tag{2.10}$$

derived by evaluating the non-relativistic U(1) charge along the solution (2.8). Here, n is the number density of the system. Two symmetries are spontaneously broken by the superfluid solution: time translations and $U(1)$. However, the following linear combination of generators is preserved by the configuration (2.8)

$$\bar{H} = H - \mu Q \tag{2.11}$$

and therefore only one massless Goldstone boson emerges in the theory, which is identified with the phonon field.

To derive the properties of the Goldstone, we perturb the classical solution

$$\Phi = (V + h)\, e^{i(\mu t + \pi)}. \tag{2.12}$$

We can plug-in the field decomposition in the original Lagrangian (2.7) and write down the Lagrangian for the angular field π and the radial field h

$$\mathcal{L}_{\rm pert} = \dot{h}^2 - (\nabla h)^2 + \left\{ \dot{\pi}^2 - (\nabla\pi)^2 + 2\mu\dot{\pi} - \frac{\lambda}{2}(V+h)^2 + \lambda V^2 \right\} (V+h)^2 \,. \tag{2.13}$$

At this point, we would like to derive the Lagrangian density of the angular mode π. However, by a close inspection of the Lagrangian (2.14), we see that this is not an easy task, because the radial and angular modes are kinetically mixed by the relativistic chemical potential. Several approximations can be adopted to simplify this procedure. First of all, because we are interested in *non-relativistic* condensates, we can ignore $\dot{h}^2$ and $\dot{\pi}^2$.

The second approximation we can take is a leading order description in spacial derivatives. As one would notice by performing a fully-fledged relativistic analysis of the spectrum [66], the theory has a gapped and a gapless mode, obtained as linear combinations of π and h. Because the gap is $\sqrt{2m^2}$ and we are interested in low-energy physics, the massive mode is non-dynamical at the energy scales of interest. This implies we can drop spacial derivatives acting on the radial mode h. Still, one has to be careful on this point. Due to the kinetic mixing, corrections that are brought in by the aforementioned terms are suppressed only by factors of k/mc_s, where k is the typical transferred momentum of the problem and c_s is the sound speed of the condensate. This implies, as we will see in the next sections, that these corrections can also be important in the non-relativistic regime if momenta bigger than mc_s are involved.

With these approximations, the low-energy Lagrangian is determined by

$$\mathcal{L}_{\rm pert} = \left\{ -(\nabla\pi)^2 + 2\mu\dot{\pi} - \frac{\lambda}{2}(V+h)^2 + \lambda V^2 \right\} (V+h)^2 \,, \tag{2.14}$$

which is a polynomial function of the radial field h. In particular, the latter can be integrated out *exactly* and the low-energy Lagrangian for π reads

$$\mathcal{L}_\pi = \frac{1}{2\lambda} \left\{ 2\mu\dot{\pi} - \left(\vec{\nabla}\pi\right)^2 + \lambda V^2 \right\}^2 \tag{2.15}$$

By deriving the quadratic part of this Lagrangian and by canonically normalizing the phonon field π, it is straightforward to see that the field is gapless

$$\mathcal{L}^{(2)}_\pi = \frac{1}{2}\dot{\pi}^2 - \frac{1}{2}c_s^2 \left(\vec{\nabla}\pi\right)^2, \qquad \text{where} \qquad c_s^2 = \frac{\lambda n}{4m^3}, \tag{2.16}$$

where the canonical rescaling $\pi \to \frac{\sqrt{\lambda}}{2m}\pi$ has been performed. Here, we approximated the relativistic chemical potential μ with the scalar field mass. As we can see, there is a massless boson in the spectrum of perturbation as expected, with a linear dispersion relation

$$\omega_k = c_s k. \tag{2.17}$$

Therefore, π can be identified with the phonon field, the low-energy and long-wavelength gapless perturbation of the superfluid.

2.2.2 The *P(X)* description

The previous example shows that the phonon field emerges in the low-energy effective description as the Goldstone boson of the spontaneously broken $U(1)$ charge and time translation. One could wonder how much the previous derivation depends on the choice of the initial lagrangian density (2.7). To investigate this, let us go back to the phonon Lagrangian obtained from the $\lambda\Phi^4$ theory and let us rearrange it into

$$\mathcal{L}_\pi = \frac{2m^2}{\lambda}\left\{\dot\pi - \frac{\left(\vec\nabla\pi\right)^2}{2m} + mc_s^2\right\}^2 \equiv \frac{2m^2}{\lambda}X^2. \tag{2.18}$$

Here, we defined the *perturbed chemical potential* X, which is the non-relativistic chemical potential $\mu_{\rm NR} = mc_s^2$ corrected by incorporating the effect of the collective fluctuations of the condensate.

What we learn from (2.18) is that the leading order low-energy description of the fluctuations of a superfluid is given by a function of the perturbed chemical potential. This property is general and can be derived from symmetry principles [67]. The potential, which mediates self-interactions, fixes the functional dependence of theory on X (e.g. $\lambda\Phi^4$ is equivalent to a X^2 theory, while $\lambda\Phi^6$ to $X^{3/2}$), but it does not determine the form of X, which is constrained by symmetries.

Let us derive this explicitly by building the general effective field theory of phonons in a zero-temperature superfluid. As it is customary while building an EFT, we have to fix the degrees of freedom content of the theory and its symmetries. Concerning the first, we understood that phonons are Goldstone bosons and therefore can be parameterized by the phase of the condensate wavefunction θ. The underlying assumption is that this degree of freedom is the *only degree of freedom of the low-energy dynamics of the system*. Concerning symmetries, because θ is connected to the phase of a $U(1)$ invariant system, the Lagrangian has to be invariant under a shift symmetry

$$\theta \;\to\; \theta + a. \tag{2.19}$$

Therefore, θ can only enter in the Lagrangian through derivatives, that is as $\partial_\mu\theta$. Nevertheless, we want a Lorentz invariant theory, therefore we conclude that the most general low-energy Lagrangian is given by

$$\mathcal{L} = P(X_{\rm rel}), \qquad \text{where} \qquad X_{\rm rel} = \partial_\mu\theta\partial^\mu\theta. \tag{2.20}$$

In this case, $X_{\rm rel}$ is the only Lorentz invariant quantity (at the lowest order in derivatives) that can be built from θ and that satisfies the shift-invariance.

We keep constraining the form of the phase θ by studying the charge associated with the spontaneously broken $U(1)$ and the energy-momentum tensor of the theory. By computing the former, we find that the number density stored in the configuration is

$$n = P'(X_{\rm rel})\,\dot\theta. \tag{2.21}$$

To have a non-zero and constant number density for the superfluid background, we need the background value of $\dot{\bar{\theta}}$ to be constant, which implies that $\bar{\theta} = \mu_{\rm rel} t$. Here $\mu_{\rm rel}$ is the relativistic chemical potential. If we introduce fluctuations of the phase, we find

$$\theta = \mu_{\rm rel} t + \pi, \tag{2.22}$$

where π is the phonon field. If we consider the non-relativistic limit of $X_{\rm rel}$, we find

$$X_{\rm rel} = \partial_\mu \theta \partial^\mu \theta \simeq m^2 + 2m \left\{ \mu_{\rm NR} + \dot{\pi} - \frac{(\vec{\nabla}\pi)^2}{2m} \right\} = m^2 + 2m\, X. \tag{2.23}$$

This proves that the non-relativistic and low-energy theory of phonons depends only on the perturbed chemical potential X.

Finally, we may provide an interpretation for the function P. By deriving the pressure of the system from the energy-momentum tensor that the background configuration sources, we find that

$$T_{ij} = \delta_{ij} P(\mu_{\rm NR}) \tag{2.24}$$

at the leading order in derivatives. Therefore, the function P is the *equation of state of the superfluid* evaluated on the background chemical potential μ. It is straightforward to check that, by choosing $P(X) = X^2$, the lagrangian (2.18) is found up to a normalization factor. This shows that the theory of the long-wavelength perturbations of a superfluid is obtained by considering the equation of state for the background and replacing the density with the non-relativistic chemical potential, according to (2.23).

It is also possible to couple the superfluid to an external field χ. Again, the coupling has to be a function of X. If we want to couple the number density of the external probe to the number density of the configuration, the only possibility is to write down the Lagrangian

$$\mathcal{L} = P(X) + g n(X) \chi^2. \tag{2.25}$$

In general, interaction vertices can be obtained by expanding the Lagrangian density (2.25) around the unperturbed chemical potential $\mu_{\rm NR}$. For example, terms quadratic in perturbations are found by expanding up to the second order

$$\mathcal{L}^{(2)}_\pi = \frac{1}{2}\dot{\pi}^2 + \frac{1}{2} c_s^2 \pi \Delta \pi \qquad \text{where} \qquad c_s^2 = \frac{P''}{\mu P'}. \tag{2.26}$$

As we can see, π is indeed the phonon field, since it is gapless and it has a linear dispersion relation. Interaction vertices can be found by further expanding the Lagrangian around $X = \mu_{\rm NR}$. In general, coefficients of this series are given by the derivatives of the pressure with respect to the chemical potential, which can be fixed by measuring the equation of state of the system.

To conclude this part, the $P(X)$ formalism is a useful tool that offers a leading-order description of the low-energy degrees of freedom in a superfluid, requiring only the equation of state of the unperturbed condensate. However, this formalism is limited to zero-temperature superfluids. Although the cosmological and astrophysical systems discussed in the next chapters are

essentially at zero temperature, we briefly mention that this formalism can be extended to include finite-temperature corrections. This can be done by following the derivation of [68], in which finite temperature effects are incorporated by including a second fluid component, carrying its own degrees of freedom, equivalently to Tisza's two-fluid model.

2.3 Beyond the leading order description

Effective field theories have a cutoff which determines their regime of validity. For example, the leading order description of the previous section becomes ill-defined for energy scales bigger than

$$\Lambda = mc_s^2. \tag{2.27}$$

Shortcomings of this cutoff can immediately be seen from (2.25), in particular, if we want to study the effect that a point particle χ with a non-relativistic velocity $v \gg c_s$ can have on the system. What takes place, in this case, is that the probe particle can interact with the superfluid background and excite a *hard phonon* with momentum $k > mc_s$. This limit lies beyond the regime of validity of the $P(X)$ description and higher-order corrections need to be considered. In particular, it was shown that certain effects (e.g. dissipation effects of a supersonic probe moving in the superfluid background [69]) can correctly be captured only if higher-order corrections in spacial derivatives are taken into account.

This is the topic of this section. Let us go back to the Lagrangian (2.14) and this time let us keep track of higher-order terms

$$\mathcal{L}_{\text{pert}} = -(\nabla h)^2 + \left\{ -(\nabla\pi)^2 + 2\mu\dot{\pi} - \frac{\lambda}{2}(V+h)^2 + \lambda V^2 - g|\chi|^2 \right\} (V+h)^2 . \tag{2.28}$$

Here, we also introduced an external complex probe χ, coupled to the original microscopic degree of freedom of the theory Φ by

$$\mathcal{L} = -g|\chi|^2|\Phi|^2. \tag{2.29}$$

We can proceed by integrating out the h field, by solving its equation of motion perturbatively in π. First, we start by solving the equation of motion for h at the linear order. A consistent solution is determined by

$$h = \frac{2V\mu}{-\Delta + 2\lambda V^2}\dot{\pi}. \tag{2.30}$$

By plugging in this solution in the Lagrangian for perturbation (2.28), we can derive the quadratic lagrangian[3]

$$\mathcal{L}^{(2)} = \frac{1}{2}\left(\dot{\pi}^2 + c_s^2 \pi\Delta\pi - \pi\frac{\Delta^2}{4m^2}\pi \right). \tag{2.32}$$

[3]Here, we canonically normalized the phonon field by applying the field redefinition

$$\pi \to \sqrt{\frac{-\Delta + 2\lambda V^2}{8V^2\mu^2}}\pi. \tag{2.31}$$

As we can see, by including higher order derivative corrections, the dispersion relation of the phonon field is extended with a term quadratic in momentum

$$\omega_k^2 = c_s^2 k^2 + \frac{k^4}{4m^2}. \tag{2.33}$$

As expected, the second term of the right-hand side dominates over the first one for momenta $k \gg 2mc_s$. In this regime, the dispersion relation of the phonon field reduces to the dispersion relation of a free non-relativistic particle. This identification becomes exact in the $c_s \to 0$ limit and it suggests that, in a $\lambda\Phi^4$ theory, a hard phonon ($k \gg 2mc_s$) can be identified with propagating free constituent Φ. Although this can be generalized to any power-law potential, let us stress that long-range self-interactions can invalidate this identification. An example of this is represented by Superfluid Helium, in which long-range forces between atoms generate a much richer phenomenology above the cutoff $2mc_s$, such as maxons and rotons.

Let us sum up the picture. When it is unperturbed, a zero-temperature superfluid is described by a classical field configuration of finite charge density. It represents a highly occupied state of constituent particles Φ, which are off-shell due to self-interactions. When the superfluid is perturbed, for example by a propagating external probe χ coupled to the original degree of freedom Φ, phonons are excited. The connection between these collective excitations and the original degrees of freedom of the system depends on the energy that the perturber dumps in the system. If $k \ll 2mc_s$, repulsive self-interactions are efficient enough to stabilize the system. In this case, if a constituent is excited out of the condensed phase, the momentum it acquires is not high enough to win over self-interactions. Therefore, it starts dumping energy to neighbour particles, which in turn are excited out of the condensed phase. This perturbation propagates as a sound wave in the superfluid bulk. In contrast, if the transferred momentum is such that a phonon with $k \gg 2mc_s$ can be excited, the constituent has enough energy to win over self-interactions and it propagates in the superfluid bulk as an almost on-shell particle. Notice that, in Bogoliubov approximation, this point is quite straightforward, since Bogoliubov transformations become trivial in this limit.

2.3.1 Higher order processes in the hard-phonon limit

(Part of this section, in particular the analysis $1 \to 3$ decay processes and the following three subsections is based on to this thesis, presented partially also in [70])

We keep investigating the relation between phonons π and constituent particles Φ by going beyond the quadratic theory. Let us still consider a $\lambda\Phi^4$ theory and focus on the cubic Lagrangian for perturbations. This can still be derived by plugging in the linear solution (2.30) in the lagrangian density (2.28). By including also interactions of the probe particle χ with the bulk, the cubic Lagrangian reads [69]

$$\begin{aligned}\mathcal{L}^{(3)} =& -\sqrt{2}gV|\chi|^2 \frac{\dot\pi}{\sqrt{-\Delta + 4m^2c_s^2}} - \frac{1}{4\mu^2}\frac{\dot\pi}{\sqrt{-\Delta + 4m^2c_s^2}}\left(\sqrt{-\Delta + 4m^2c_s^2}\,\vec\nabla\pi\right)^2 \\ &+ \frac{1}{2\sqrt{2}V}\left(\frac{\dot\pi}{\sqrt{-\Delta + 4m^2c_s^2}}\right)^2 \frac{-\Delta}{\sqrt{-\Delta + 4m^2c_s^2}}\dot\pi,\end{aligned} \tag{2.34}$$

where the phonon field has been canonically normalized.

Now, we can test if the discussion of the previous section is correct by computing the decay rate of the process

$$\chi(p_i) \to \chi(p_f) + \pi(k). \tag{2.35}$$

If a hard phonon π can be associated with a moving constituent Φ, we expect that the process (2.35) is describing the scattering of a probe particle on a zero-momentum superfluid constituent, which is then kicked out from the condensed phase by the event. Therefore the decay rate of the (2.35) should be equivalent to a 2-body scattering rate after the limit $p_i \gg mc_s$ is taken.

Let us show this by following the derivation of [69]. From the Lagrangian density (2.34), the amplitude of the process (2.35) reads

$$\mathcal{A}_{\chi\to\chi+\pi} = -i\frac{gV}{\sqrt{2}m}k, \tag{2.36}$$

where we also set on-shell the final radiated phonon. By computing the decay rate, we find

$$\lim_{(mc_s)/(Mv_i)\to 0} \Gamma_{\chi\to\chi+\pi} = \left(\frac{g^2}{16\pi\,(m+M)^2}\right) n_{\rm sf}\, v_i, \tag{2.37}$$

where v_i and M are the initial velocity and mass of the probe χ. Here, we considered the double-scaling limit $v_i \to \infty$ and c_s constant, since the sound speed also depends on the parameter of the theory. The decay rate (2.37) matches the 2-body scattering rate of the process

$$\chi(p_1) + \Phi(0) \to \chi(p_3) + \Phi(p_4) \tag{2.38}$$

if we identify the 2-body scattering cross section $\sigma = g^2/16\pi\,(m+M)^2$. This confirms that hard phonons can be associated with propagating constituents. It is also possible to show that the same applies to the process

$$\pi(p_i) \to \pi(p_f) + \pi(k). \tag{2.39}$$

This case is intriguing because, in the limit of $p_i/mc_s \to \infty$, the interaction rate vanishes too since the superfluid reduces to a non-interacting Bose-Einstein condensate. However, if we keep the first subleading correction, the rate (2.39) becomes equivalent to a two-body scattering rate in which all initial and final particles have the same mass m.

We keep pushing forward the identification of phonons as moving particles by computing the process

$$\chi(p_i) \to \chi(p_f) + \pi(k_1) + \pi(k_2). \tag{2.40}$$

We anticipate that the rate of the scattering process involving one χ particle and two Φ particles goes to zero as the sound speed approaches zero since the $|\Phi|^2|\chi|^2$ potential alone cannot account for a single χ particle to excite two constituent Φ particles unless we reintroduce collective effects, and therefore c_s^2 corrections. On the other hand, if we consider a $|\chi|^2|\Phi|^4$ potential, the interaction vertex should allow for three-to-three scatterings and the interaction rate is expected to be non-zero also in the limit of vanishing sound speed.

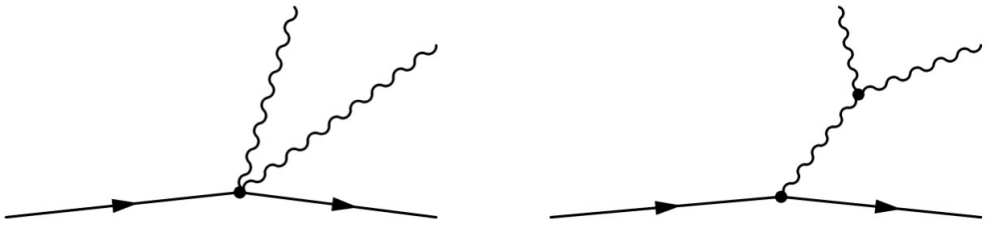

Figure 2.2: Feynmann diagrams describing a probe χ radiating two phonons in the shift-invariant parametrization. In the limit of vanishing sound speed, this is equivalent to a prob particle χ scattering on a superfluid constituent and kicking it out from the condensate phase.

Let us show this in a general way, by replacing the $|\chi|^2|\Phi|^2$ coupling with the general power-law vertex

$$\mathcal{L} \supset -\frac{g}{n-1}|\chi|^2|\Phi|^{2n-2} \qquad n \geq 2, \tag{2.41}$$

where $n = 2$ is the case we have been considering so far. According to what we said, only in this case the rate (2.40) is expected to vanish. To compute the interaction rate of a perturber χ radiating two phonons while moving in the superfluid bulk, we need the cubic and quartic Lagrangian obtained from the potential (2.41). This is obtained by integrating out the radial field h up to the second order in perturbations and therefore we have to solve its quadratic equation of motion. In this case, the second-order solution is determined by

$$h^{(2)} = \frac{1}{-\Delta}\left(4m^2V\dot{\pi}\frac{1}{-\Delta}\dot{\pi} - (\vec{\nabla}\pi)^2 - g|\chi|^2V^{2n-3}\right) \tag{2.42}$$

Here, we dropped c_s^2 terms since we are interested in zero-order contribution in the sound speed. By plugging in the solution in the lagrangian density we find

$$\begin{aligned}\mathcal{L} =& \frac{gV^{2n-4}}{4m^2}|\chi|^2\frac{1}{-\Delta}(\sqrt{-\Delta}\partial_i\pi)^2 - \frac{(2n-3)gV^{2n-4}}{2}|\chi|^2\left(\frac{\dot{\pi}}{\sqrt{-\Delta}}\right)^2 \\ & - gV^{2n-4}|\chi|^2\frac{1}{-\Delta}\left[\left(\sqrt{-\Delta}\dot{\pi}\right)\frac{\dot{\pi}}{\sqrt{-\Delta}}\right].\end{aligned} \tag{2.43}$$

Phonon self-interactions, which we need up to the cubic order, are unchanged by the new interaction (2.41). In Fig.2.2, we may find the Feynmann diagrams the contribute to the two-phonon radiation process. Partial amplitudes read

$$\mathcal{A}_1 = \frac{gv^{2n-4}}{2m^2}k_1k_2\left(\frac{2k_1k_2\cos\theta}{k_1^2+2k_1k_2\cos\theta+k_2^2} - n + 1\right) \tag{2.44}$$

$$\mathcal{A}_2 = \frac{gv^{2n-4}}{2m^2}\frac{k_1k_2(k_1^2+k_2^2)}{k_1^2+k_2^2+2k_1k_2\cos\theta}, \tag{2.45}$$

where $\mathcal{A}_1$ and $\mathcal{A}_2$ are, respectively, the amplitude of the left and right diagram of Fig. 2.2. Here, k_1 and k_2 are the momenta of final emitted phonons, while θ is the relative angle between them. Also, we imposed the energy-momentum conservation on the virtual phonon. The sum of the two amplitudes reads

$$\mathcal{A}_1 + \mathcal{A}_2 = -\frac{g v^{2n-4}(n-2)}{2m^2} k_1 k_2. \tag{2.46}$$

As we may see, the sum (2.46) vanishes for $n = 2$, as predicted. In this case, the potential (2.41) cannot generate a three-body point-like scattering without taking into account the self-interactions of Φ.

2.3.2 Hard-phonon limit in linear parametrization

If the sound speed of the condensate is kept finite, the shift-invariant parametrization (2.12) is quite convenient to study the dynamics of perturbations of the finite charge solution. Nevertheless, when the $c_s \to 0$ limit is considered, there does exist a more suitable parametrization of fluctuations, which is the *linear parametrization*

$$\Phi = (V + h + i\pi)\, e^{i\mu t}. \tag{2.47}$$

To show this, let us re-derive the theory of perturbations starting from the lagrangian density

$$\mathcal{L} = \partial_\mu \Phi^+ \partial^\mu \Phi - m^2 \left|\Phi\right|^2 - g|\Phi|^2|\chi|^2. \tag{2.48}$$

Here, we drop self-interactions since we are interested in the $c_s \to 0$ limit of the theory. The advantage of this parametrization is that, in the limit of vanishing sound speed, phonon self-interactions vanish too. Because of this, it is possible to compute *all* vertexes involving the $|\chi|^2$ operator times an arbitrary number of π fields, by simply solving the equation of motion for h at the linear order in perturbations. Higher order corrections would only source higher order terms in χ, such as $|\chi|^4, |\chi|^6$, etc.

By following the same derivation of the previous sections, we derive the following Lagrangian for perturbations

$$\mathcal{L} = \frac{1}{2}\dot{\pi}^2 + \pi\frac{\Delta^2}{4m^2}\pi - \sqrt{2}gv|\chi|^2\frac{\dot{\pi}}{\sqrt{-\Delta}} - \frac{g}{2}|\chi|^2\left[\left(\frac{\dot{\pi}}{\sqrt{-\Delta}}\right)^2 + \left(\frac{\sqrt{-\Delta}}{2m}\pi\right)^2\right]. \tag{2.49}$$

The dispersion relation of the phonon mode misses the term linear in momentum as expected, since we dropped self-interactions. Therefore, the system behaves like a non-interacting Bose-Einstein condensate. Now, we can focus on interactions of the probe particle χ and with the phonon field. The term linear in the phonon field matches the one obtained from the shift-invariant parametrization. In contrast, the term quadratic in the phonon field is different and more compact. In this case, we only have a point-like vertex and the second diagram of Fig. 2.2 is missing. Nevertheless, the result is equivalent: the amplitude of the process (2.40) derived from (2.49) vanishes once the two final phonons are put on-shell.

Finally, if we do the same for a $\frac{g}{2}|\chi|^2|\Phi|^4$ interaction vertex, the interaction Lagrangian for perturbation reads

$$\begin{aligned}\mathcal{L} \supset & -\sqrt{2}gv^3|\chi|^2\frac{\dot{\pi}}{\sqrt{-\Delta}} - \frac{gV^2}{2}|\chi|^2\left[3\left(\frac{\dot{\pi}}{\sqrt{-\Delta}}\right)^2 + \left(\frac{\sqrt{-\Delta}}{2m}\pi\right)^2\right] + \\ & - 2gV|\chi|^2\left[\left(\frac{\dot{\pi}}{\sqrt{-\Delta}}\right)^3 + \left(\frac{\dot{\pi}}{\sqrt{-\Delta}}\right)\left(\frac{\sqrt{-\Delta}}{2m}\pi\right)^2\right] \\ & - \frac{g|\chi|^2}{8}\left[\left(\frac{\dot{\pi}}{\sqrt{-\Delta}}\right)^4 + 2\left(\frac{\dot{\pi}}{\sqrt{-\Delta}}\right)^2\left(\frac{\sqrt{-\Delta}}{2m}\pi\right)^2 + \left(\frac{\sqrt{-\Delta}}{2m}\pi\right)^4\right] \end{aligned} \tag{2.50}$$

We may now read the amplitude of a χ perturber radiating one/two/three and four phonons through the potential (2.50). Assuming on-shell final particles, those reads:

$$\mathcal{A}(\chi \to \chi\pi) = i\frac{gV^3}{\sqrt{2}m}k, \tag{2.51}$$

$$\mathcal{A}\left(\chi \to \chi\pi^2\right) = -\frac{gV}{2m^2}k_1k_2 \tag{2.52}$$

$$\mathcal{A}\left(\chi \to \chi\pi^3\right) = \mathcal{A}\left(\chi \to \chi\pi^4\right) = 0 \tag{2.53}$$

As we can see, the amplitude of a χ probe radiating two phonons is not trivial and matches the one obtained in the shift-invariant parametrization. At the same time, processes involving more than two final phonons lead to null amplitude once evaluated for on-shell particles. This is consistent with the idea that the potential $|\chi|^2|\Phi|^4$ cannot mediate a process where three or four constituents are kicked out of the condensate by the perturber χ unless self-interactions between constituents are invoked.

2.3.3 Three body scattering rate

We have demonstrated that a probe particle χ that radiates a phonon π is equivalent to the scattering of the same probe particle on a superfluid constituent Φ, once the limit $c_s \to 0$ is considered. We have shown this for the specific two-body interaction $|\chi|^2|\Phi|^2$.

In this section, we exploit this property in a reverse way and use it to compute the three-body scattering rate of

$$\chi(p_i) + \Phi_1(0) + \Phi_2(0) \to \chi(p_f) + \Phi_1(k_1) + \Phi_2(k_2), \tag{2.54}$$

by introducing the potential self-interacting potential

$$-\frac{g}{2}|\chi|^2|\Phi|^4. \tag{2.55}$$

Here, we set the mass of the probe particle $M = m$ to simplify the computation and we work in the zero sound speed limit. Also, in this limit, the interaction rate of this process is expected to

be similar to the three-body scattering rate in $\lambda|\Phi|^6$, although we discuss in details this point in the next section.

In contrast to quartic potentials, where the single-phonon radiation is the only non-zero decay channel, sextic potentials exhibit two main processes that contribute to the three-body scattering rate as discussed in the previous section. By summing them, we may evaluate the interaction rate of the process (2.56) by computing

$$\Gamma\left(\chi+\Phi+\Phi\to\chi+\Phi+\Phi\right)\equiv\Gamma\left(\chi\to\chi+\pi\right)+\Gamma\left(\chi\to\chi+\pi+\pi\right). \tag{2.56}$$

The connection of the second process on the right-hand side with the constituent picture is straightforward: it is the scattering rate of a probe particle χ interacting with two superfluid constituents and kicking them out of the condensed phase. In the mean field description, two phonons are radiated by the probe, one for each constituent that has been put in motion.

The first process is also interesting. In this case, the probe particle χ interacts with two constituents but transfers its momentum only to one of them. As a result, only one final phonon appears in the mean-field description since only one constituent is removed from the condensed phase. The sum of these two contributions determines the total three-body scattering rate.

Let us evaluate the partial interaction rates. The first term of the right-hand side is obtained from (2.37) by setting $M = m$ and by adding a factor of V^4. For the second term, we follow the approach of [71]. Partial rates read

$$\Gamma\left(\chi\to\chi+\pi\right)=\frac{g^2n_{\rm sf}^3}{256\pi m^4}\,v_i,\qquad\Gamma\left(\chi\to\chi+\pi+\pi\right)=\frac{g^2n_{\rm sf}^2}{1024\pi m}\,v_i^4. \tag{2.57}$$

Here, v_i is the velocity of the incoming perturber χ. By summing over the two partial contributions, the total rate of a probe particle χ scattering over two constituents Φ reads

$$\Gamma\left(\chi+\Phi+\Phi\to\chi+\Phi+\Phi\right)=\frac{g^2n_{\rm sf}^2}{1024\pi^4m}\,v_i^4\left\{1+\frac{n_{\rm sf}\lambda_{\rm db}^3}{2}\left(\frac{v}{v_i}\right)^3\right\}. \tag{2.58}$$

The first and second terms in Eq. (2.58) correspond to the contribution from two-phonon and one-phonon radiation, respectively. It's worth noting that in the second term in parentheses, we identified the *de Broglie wavelength* of a constituent particle $\lambda_{\rm db} = 2\pi/(mv)$, where v is the velocity dispersion of the system of bosons Φ. By recognizing this, we can draw the following conclusions:

- If the system is not degenerate, that is $n_{\rm sf}\lambda_{\rm db}^3 \ll 1$, the three-body scattering rate is dominated by the process where χ transfers its momentum to *both* the particles at rest[4]. This is consistent with the classical intuition, which suggests that during the scattering of a probe on two particles at rest, both of them are more likely to be put in motion due to the larger

[4]One could question that this result does not holds the non-degenerate limit since the derivation is performed in a mean-field approximation. Nevertheless, notice that the rate of a probe χ radiating a phonon matches (2.37) the two-body scattering rate of two isolated particles. This seems to indicate that we can extend the result of a mean-field computation to non-degenerate systems.

phase space of this case. Notice that this conclusion also applies to an incoming perturber scattering on a degenerate condensate, when the perturber has a velocity much bigger than the internal velocity dispersion of the system.

- If the de Broglie volume is highly occupied and the velocity of the perturber is similar or smaller than the velocity dispersion of the system, the scattering rate is dominated by the process where χ transfers its momentum *only* to one constituent particle Φ. This behaviour is in accordance with the Bose-Einstein statistics, which suppresses processes in which particles are injected into non-degenerate states, compared to processes where final states are highly occupied. Hence, processes in which only one particle is excited into a high momentum empty state exhibit *Bose enhancement* when compared to processes where both constituent particles are extracted from the condensate. This enhancement of the single-phonon channel compensates for the smaller phase space available for such events in comparison to the two-phonon case.

Finally, the same conclusions will apply if the probe particle χ is replaced with a constituent particle Φ. In this case, the interaction rate matches (2.58), up to an overall order one overall factor that takes into account the different symmetry factors of the process.

2.3.4 Relaxation rate of a degenerate gas of three-body interacting particles

The exercise of the previous section, the derivation of the three-body scattering rate (2.57), has important implications in the context of the dynamics of many-body systems. In particular, it can be exploited to derive the thermalization time of a three-body interacting system. This is an important time scale, as it allows us to characterize the time it takes for a system to get to thermal equilibrium due to its own internal interactions. For a two-body interacting system, it can be approximated as the time it takes for every single particle of the system to interact at least once. In other words, a good estimate is provided by the inverse of the *relaxation rate*, which in turn is approximated by the interaction rate [72–74]. Therefore, we may use the aforementioned identification to estimate the relaxation time for a gas in which constituents interact mainly through three-body interactions. This can be a difficult computation if performed in terms of constituents, but it becomes simpler if performed in the language of the long-wavelength fluctuations

First, we should consider whether the rate given in Equation (2.58) can be applied as an approximation to describe a general three-body scattering, so when the system in question is not a condensate but a typical gas. In these cases, the two constituent particles do not have zero momentum and a different, more complex kinematic should in principle be considered. However, in the same way as a two-body interacting system, for three-body interactions, the rate (2.58) provides a good order one approximation for the relaxation rate *if the gas of particles is non-degenerate*. In other words, we have

$$t_{\text{rel}}^{-1} \sim \Gamma\left(\chi \to \chi + \pi + \pi\right), \tag{2.59}$$

where χ plays the role of a Φ constituent and we identify $v \sim v_i$. Notice that we ignored the single phonon channel, which is negligible if the system is not degenerate. This result provides an

approximate result since the different initial kinematics of a general scattering should contribute with an order one factor.

Unfortunately, in the case of a *degenerate* gas of Φ particles, we cannot directly apply the formula (2.59) to evaluate the relaxation rate. The scattering rate we derived in the previous part has a specific physical meaning: it describes an excited particle scattering over a condensate of zero momentum constituents. In contrast, the phase space of a gas of degenerate particles which is not at equilibrium is expected to be comprised of a lot of high occupied energy levels. This implies that it is extremely likely that constituent particles of the gas would be scattered into highly occupied energy levels, and not empty ones as in the case of the condensate solution. The outcome of this is that scatterings between particles are now enhanced by *Bose-enhancement factors* $\mathcal{N}$, which roughly counts the number of particles per de Broglie volume of the specific energy levels which are involved in the process. We can estimate it as

$$\mathcal{N} = n\lambda_{\rm db}^3, \tag{2.60}$$

with n average number density of the gas[5].

If we compute the relaxation rate starting from the three-body interaction rate, we have to add n factors of $\mathcal{N}$ in front of the partial rates involving phonons, where n is the number of constituent particles whose momentum changed in the scattering process [73, 75], without counting χ [6]. Because each phonon is associated with a constituent particle that changed the energy level, we have to add a factor of $\mathcal{N}$ per every phonon that is radiated.

Therefore, the relaxation rate for a degenerate gas of bosons interacting mainly through three-body interactions read

$$t_{\rm rel}^{-1} \sim \mathcal{N}\Gamma\left(\chi \to \chi + \pi\right) + \mathcal{N}^2\Gamma\left(\chi \to \chi + \pi + \pi\right) \sim \mathcal{N}^2 \frac{3g^2n^2}{2048\pi^4 m}\, v^4, \tag{2.61}$$

where we set the velocity of the perturber (in this case a Φ particle) equal to the velocity dispersion of the gas. Here, we neglected certain symmetry factors that should be reintroduced for simplicity and we redirect the reader to [70] for these details. It is important to note that, in a non-degenerate gas, only the two-phonon channel contributes to the relaxation rate. However, in the degenerate case, both the single and two-phonon channels contribute equally to the relaxation rate.

[5] This also explains why we can directly use the three-body scattering rate derived for a condensate solution to describe the case of a gas of non-degenerate particles. When evaluating the relaxation rate, the Bose-enhancement factor only appears to count the degeneracy of final states [75]. In the case of the scattering of a particle over the condensate or of three particles in the vacuum, the final states are non-degenerate and the only distinction between these scenarios is the kinematics.

[6] Although we are implicitly assuming that the χ particle is identical to a Φ particle, the number of Bose factors that enter in the relaxation rate for a degenerate system is equal to the number of final particles involved in the scattering minus one and therefore we can ignore χ in the counting.

2.4 Superfluidity and Gravity

Up to this point, we have described how the dynamics of the low-energy degrees of freedom of a superfluid can be addressed. While this formalism is sufficient for studying the properties of the superfluid phase in laboratory settings, it lacks a fundamental ingredient for its application to galactic dynamics: gravity. As a result, this section aims to conclude the discussion of the EFT of superfluidity by incorporating the effect of gravity. Specifically, we will focus on the *theory of phonons in the presence of gravity*, while the analysis of self-gravitating classical profiles will be discussed in the next chapter.

Concerning the $P(X)$ approach, gravity can be introduced by incorporating its effects in the chemical potential of the system [76]. Given the Newtonian potential $\varphi(x)$, its effect on the superfluid bulk can be described by introducing a new perturbed chemical potential

$$X' = \mu - m\,\varphi(x) + \dot{\pi} + \frac{(\nabla\pi)^2}{2m}. \tag{2.62}$$

and the most general Lagrangian density is now determined by $P(X')$. Nevertheless, in this discussion, we want to be as general as possible and keep also higher-order derivatives corrections. We briefly review the derivation of this case, by following [77].

We start by considering a quartic superfluid minimally coupled to gravity

$$S = \int d^4x\sqrt{-g}\left\{\frac{R}{16\pi G} + \partial_\mu\Phi^+\partial^\mu\Phi - m^2|\Phi|^2 - \frac{\lambda}{2}|\Phi|^4\right\}, \tag{2.63}$$

where R is the scalar curvature. Again, we can introduce the solution (2.12) and study the dynamics of its perturbations. In this case, we also have to track the gravitational degree of freedom. Since we are interested in non-relativistic superfluids, we consider the weak-field limit of gravity

$$ds^2 = (1-2\varphi)\,dt^2 - \delta_{ij}dx^i dx^j. \tag{2.64}$$

In this case, the Lagrangian for perturbations reads

$$\mathcal{L} = \frac{1}{8\pi G}\varphi\Delta\varphi + h\Delta h + 2m\,(V+h)\left\{\mu - m\varphi + \dot{\pi} - \frac{(\vec{\nabla}\pi)^2}{2m}\right\} - \frac{\lambda}{2}\,(V+h)^4\,. \tag{2.65}$$

We integrate out h and the Newtonian potential $\varphi(x)$, assuming that the latter is sourced by a homogeneous configuration. The resulting quadratic canonically normalized Lagrangian for perturbations is

$$\mathcal{L} = \frac{1}{2}\dot{\pi}^2 + \frac{1}{2}\pi\left(m_g^2 + c_s^2\Delta - \frac{\Delta^2}{4m^2}\right)\pi + ..., \tag{2.66}$$

where $m_g = 4\pi G\rho$ is the Jeans mass. The presence of gravity introduces an additional tachyonic term in the dispersion relation of phonons, which now reads

$$\omega_k^2 = -m_g^2 + c_s^2k^2 + \frac{k^4}{4m^2}. \tag{2.67}$$

This modification leads to the instability of condensates which are large enough, driven by the tachyonic modes they exhibit. In the subsequent section, we demonstrate that this instability is reminiscent of the well-known Jeans instability, and it suggests that self-gravitating superfluid configurations become unstable beyond a certain size, as their self-interactions are inadequate to counteract the gravitational collapse.

Chapter 3

Superfluid Dark Matter

This chapter is devoted to studying the phenomenology of a dark matter superfluid, with a particular emphasis on the consequences that this phase of dark matter can have on the formation and evolution of halos. Most of the content of this chapter is based on an original work of the author of this thesis, that was published in [70] and [78].

The idea of dark matter existing in the form of condensates at characteristic galactic densities can be summarized in two different but complementary proposals, which mainly differ by the impact that dark matter self-interactions have on the dynamics of the condensed phase (see [79] for a general review). To be as general as possible, let us consider a homogeneous configuration of real scalar bosons with repulsive quartic self-interactions, which are minimally coupled to gravity. The resulting Lagrangian reads

$$\mathcal{L} = \frac{1}{8\pi G}\varphi\vec{\nabla}^2\varphi + \frac{i}{2}\left(\psi^*\partial_t\psi - \psi\partial_t\psi^*\right) - \frac{|\vec{\nabla}\psi|^2}{2m} - \frac{\lambda}{16m^2}|\psi|^4 - m^2|\psi|^2\varphi, \tag{3.1}$$

where φ is the Newtonian potential as in the previous chapter. Since dark matter has to behave as a non-relativistic fluid on cosmological scales, here we considered the non-relativist limit of the Lagrangian (2.63) [1]. In line with the previous section, we introduce a highly occupied configuration of zero momentum bosons, the dark matter condensate, with a non-relativistic energy density determined by

$$\rho \simeq m^2|\psi|^2. \tag{3.2}$$

By reading the Lagrangian (3.1), we realize that the internal dynamics of the system at a certain scale k^{-1} depends on the relative magnitude of the third and fourth term at that particular scale. If dark matter self-interactions are negligible at galactic scales (kpc), then we have models of *Fuzzy dark matter* [50, 51]. By introducing scalar bosons with a mass $m \sim 10^{-21}$ eV as constituents of the condensate, the de Broglie wavelength $\lambda_{\rm db} \sim (mv)^{-1}$ of dark matter particles

[1] More precisely, this is the non-relativistic approximation of the real counterpart of the Lagrangian (2.63). The two formulations are equivalent in the non-relativistic approximation since number-changing processes are suppressed in this limit. The non-relativistic limit is obtained by introducing the decomposition $\hat{\phi} = \frac{1}{\sqrt{2}}\left(\psi e^{imt} + \psi^* e^{-imt}\right)$ and averaging over time-scales larger than m^{-1}.

at typical galactic densities becomes $\sim$ kpc sized, making manifest their wave-like nature at these scales.

Because the wavefunction of particles spreads over the size $\lambda_{\rm db}$ due to the Heisenberg uncertainly principle, substructures which are smaller than this scale are efficiently fuzzed out by the positive *quantum pressure*. Since this positive pressure can lead to the formation of quasi-homogeneous regions in dark matter halos, the model was originally proposed to ameliorate the excess of dark matter in inner regions of halos and the excess of substructures predicted by N-body simulations[2]. Over time, these claims have been supported by several numerical investigations [52, 80, 81].

On the other hand, if the fourth term of (3.1) dominates over the third one at typical galactic scales, self-interactions can profoundly change the phenomenology of the condensate, as discussed in Chapter 2. Hence, a second and complementary approach — as proposed by J. Goodman in [54] — is to consider condensates whose dynamics is dominantly driven by microscopic *repulsive* self-interactions, hence superfluids. In this case, a quasi-homogeneous core may form in central regions of halos due to the positive pressure sourced by interactions. The model was originally introduced as an improved alternative to models of self-interacting dark matter, since degenerate condensates can sustain macroscopic configurations also at zero temperature, preventing the gravo-thermal collapse characteristic of SIDM models [46, 82, 83].

Later, the model was claimed to be ruled out in [84]. By assuming a specific finite-temperature equation of state for the superfluid, the global thermal equilibrium of the dark matter halo, the spherical symmetry of the condensate wave function, and the bullet cluster constraint, the authors demonstrated that it is not possible to derive dark matter density profiles which are consistent with observations. While the shortcomings of the equation of state have been addressed in [85, 86], this chapter is devoted to revising the leftover underlying assumptions. In particular, we show that it is possible to relax the assumption of global thermal equilibrium, and also that the spherical symmetry of the wavefunction of the halo is untenable within the context of this model.

Finally, let us mention that Dark Matter Superfluidity has been revitalized in the past years by the complementary approach proposed in [55,56]. In these papers, the dynamics of the superfluid phase is exploited to generate long-range interaction between baryons, which are mediated by phonons. The only additional ingredient is the coupling of the baryonic sector to the dark matter sector of the theory. It was shown that by choosing a particular microscopic dynamics for the dark matter fluid, that is a specific form of the $P(X)$ Lagrangian, it is possible to generate an emergent force between baryons that can emulate the behaviour of the Modified Newtonian Dynamics (MOND) [87–89], as long as baryons are submerged within the dark matter superfluid.

[2]The quantum pressure is a statistical pressure peculiar to non-homogeneous configurations. It is determined by evaluating the leading non-relativistic spacial component of the energy-momentum tensor. We may obtain an estimate of this component of the pressure by evaluating the kinetic term of (3.1) using $i\vec{\nabla}\psi \sim R^{-1}\psi$, with R the scale of the inhomogeneity. By replacing the field value with the density ρ, we arrive at

$$P \sim \left(\frac{\hbar^2}{m^2 R^2}\right)\rho. \tag{3.3}$$

The model is also successful in reproducing the large-scale predictions of ΛCDM and the mass function of clusters. The possibility of having long-range forces also in non-interacting Bose-Einstein condensates was studied in [90], while the implications of dark matter superfluidity in the context of dynamical friction have been discussed in [77]. In this chapter, we will not explore this particular realization, as we are not introducing any coupling between the baryonic and dark sectors.

3.1 Hydrodynamic properties of the Dark Matter Superfluid

To start describing the phenomenology of a dark matter superfluid, it is convenient to study the hydrodynamic properties of the theory (3.1). Let us consider a classical field configuration of finite energy density $\rho_{\rm sf}$. As discussed in the previous chapter, the low-energy spectrum of perturbation in the presence of gravity reads

$$\omega_k^2 = -4\pi G\rho_{\rm sf} + c_s^2 k^2 + \frac{k^4}{4m^2}. \tag{3.4}$$

By analysing the spectrum (3.4) we see that perturbations which are softer than the characteristic scale

$$k_j^2 = 2m^2 c_s^2 \left(-1 + \sqrt{1 + \frac{4\pi G\rho}{m^2 c_s^4}}\right) \tag{3.5}$$

are unstable. The mode k_j is the *Jeans momentum* and it determines the characteristic scale $\ell = 2\pi k_j^{-1}$, commonly known as *Jeans scale*. The latter can be interpreted as the size above which self-gravitating configurations are unstable and would collapse gravitationally [91].

We can examine two limits of (3.5), which depend on which contribution between the quadratic and quartic term of (3.4) dominates at the scale of the collapse $k \sim \sqrt{4\pi G\rho}$. These two regimes are identified by the magnitude of the parameter

$$\xi = \frac{m^2 c_s^4}{4\pi G\rho}. \tag{3.6}$$

If the parameter ξ is small, the Jeans scale reduces to the characteristic Jeans scale of the Fuzzy dark matter model [50, 51]

$$\ell \simeq \left(\frac{\pi^3}{G\rho m^2}\right)^{\frac{1}{4}}, \qquad \xi \ll 1. \tag{3.7}$$

In this case, the gravitational collapse is prevented by the quantum pressure of the field configuration. Hence, in the rest of this thesis we refer to this case as *degeneracy pressure case*.

If $\xi \gg 1$, then the collapse is prevented by the pressure generated by the repulsive self-interactions and the Jeans scale reduces to [92]

$$\ell \simeq \left(\frac{\pi c_s^2}{G\rho}\right)^{\frac{1}{2}}, \qquad \xi \gg 1. \tag{3.8}$$

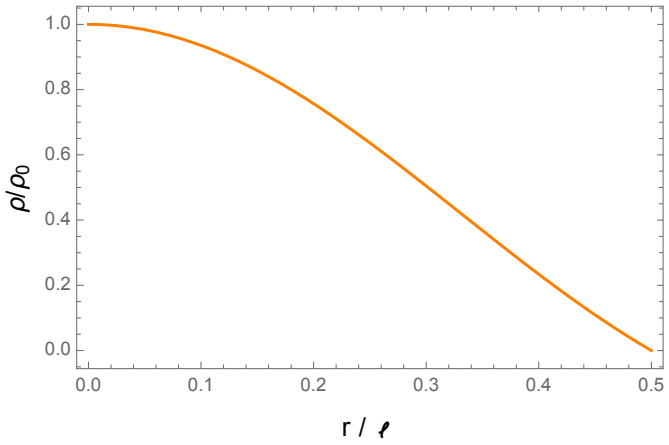

Figure 3.1: Density profile of a self-gravitating superfluid configuration (3.13). Here, two-body interactions source the pressure that stabilizes the configuration. The diameter of the configuration is equal to the Jeans length of the system.

We refer to this case as *interaction pressure case*, since the gravitational collapse is prevented by the pressure provided by the self-interactions.

Since interactions source positive pressure, the theory admits non-topological soliton solutions, derived as the stationary non-relativistic self-gravitating configurations of the theory. To find their density profile, we solve the equation of hydrostatic equilibrium[3], combined with Poisson's equation

$$\frac{1}{\rho}\frac{dP}{d\rho} = -\vec{\nabla}\varphi \tag{3.10}$$

$$\nabla^2\varphi = 4\pi G\rho_{\rm sf}. \tag{3.11}$$

To solve this system, we also have to provide the equation of state of the superfluid. For the theory at hand, we have

$$P = \frac{\lambda\rho^2}{8m^4}. \tag{3.12}$$

Notice that this form of the pressure is legitimate only in the regime $\xi \gg 1$, hence as long as the quantum pressure is negligible compared to the interaction pressure.

By plugging in the pressure (3.12) in the equation of hydrostatic equilibrium, we derive the density profile of the superfluid soliton [54, 94]

$$\rho(r) = \rho_{\rm sf}\frac{\sin(2\pi r/\ell)}{2\pi r/\ell}. \tag{3.13}$$

[3]This equation is derived by considering the equation of motion of ψ, derived from (3.1). Using the Madelung decomposition [93]

$$\psi = \sqrt{\frac{\rho}{m}}e^{i\alpha}, \qquad \vec{v} = \frac{1}{m}\vec{\nabla}\alpha, \tag{3.9}$$

equation (3.10) is obtained as the equation for the velocity field $\vec{v}$ in the stationary limit $\partial_t\vec{v} = \vec{\nabla}\cdot\vec{v} = 0$.

The scale ℓ is the Jeans scale in the interaction pressure case and $\rho_{\rm sf}$ is the superfluid soliton central density. Notice that, for two-body interacting superfluids, this scale is density-independent. In Fig. 3.1, we plot the density profile of the soliton (3.13). The Jeans scale exactly represents the *diameter* of the configuration. Also, we see that the density profile is almost homogeneous in inner regions, due to the positive pressure provided by self-interactions.

3.2 Formation of the superfluid phase

Having depicted the hydrodynamic properties, we derive what are the minimal conditions that would lead to the formation of the superfluid phase in galaxies.

In Chapter 2, we discussed the relation between superfluidity and Bose-Einstein condensation. Based on that discussion, one might have inferred that achieving local thermalization is a prerequisite for condensation. However, this point requires some further elucidation. Condensation may occur as long as the de Broglie volume of the system is highly occupied, and this condition is independent of thermal equilibrium. This takes place in models of Fuzzy Dark Matter for example, in which self-interactions are never efficient enough for establishing equilibrium. Therefore, with the previous section in mind, we define the *coherence scale* $\ell_{\rm c}$ of the system, namely the scale below which superfluid properties may transpire and the gas of dark matter particles can be considered as an effective condensate. This is set by [73]

$$\ell_{\rm c} \simeq \min\left(\frac{2\pi}{k_*}, \lambda_{\rm db}\right) \qquad \text{with} \qquad \lambda_{\rm db} = \frac{2\pi}{mv} \qquad \text{(de Broglie wavelenght).} \tag{3.14}$$

Here, v is the velocity dispersion of the system. In other words, the coherence length is set as the minimum between the scale of gravitational stability and the de Broglie wavelength. Let us investigate what properties dark matter should have to determine a coherence length which is kpc-sized. Without thermalization (so without a mechanism that would push all particles in zero momentum state), the typical velocity dispersion of dark matter particles in galaxies is $v \simeq 10^{-3}$ and extremely light masses ($m \simeq 10^{-21}$ eV) are required to have coherence over the kpc scales. This is because it is the de Broglie wavelength that sets the scale of coherence unless masses lighter than the fuzzy dark matter scales are considered, which is a scenario highly constrained by observations [95–97].

In contrast, if a local thermal equilibrium is established, the coherence length is determined by the Jeans scale. This is because thermalization and relaxation processes efficiently reshuffle the dark matter phase space, by creating a highly occupied zero momentum state [4]. Therefore, in practice, one needs to invoke thermalization for a kpc-sized core to be formed in galaxies, for moderately sub-eV particles.

Following what we said, the formation of a macroscopic superfluid phase of dark matter sets in if the following two conditions are satisfied:

[4] Intuitively, if dark matter reaches equilibrium and all particles are pushed into a zero momentum state, the velocity dispersion of the configuration approaches 0 and $(mv)^{-1} \to \infty$. In this case, the coherence length (3.14) is determined by the Jeans scale.

- The system is in local equilibrium. This is achieved if particles have sufficient time to interact, allowing them to establish a Bose-Einstein statistics. The time it takes to reach the equilibrium can be estimated as the time it takes for each particle to scatter at least once [74]. The longer one waits, compared to this time scale, the more certain one can be for being close to equilibrium. For typical dark matter halos, density distributions are not homogeneous and it is expected that high-density regions thermalize first. Because of this, we may define a new peculiar scale of the halo, the thermal radius R_T, which is the radius within which dark matter is in thermal equilibrium.

- The de Broglie wavelengths of particles overlap. This property is not implied by the previous condition, as systems can be in thermal equilibrium, but not in a degenerate state. The degeneracy of a thermal system is achieved if the system itself is colder than the critical temperature $T_c \sim n^{2/3}/m$; with n denoting the particle number density at galactic scales. As for local thermal equilibrium, we may also identify a peculiar scale of the dark matter halo which is connected to the property of degeneracy. We call it the degeneracy radius $R_{\rm deg}$.

To sum up, the phenomenology of dark matter halos in the theory (3.1) depends on different emergent length scales. The first is the *thermal radius* R_T. It sets the radius within which dark matter interactions are efficient enough to have dark matter particles in thermal equilibrium. The second scale is the *degeneracy radius* $R_{\rm deg}$, which sets the region of the halo in which the de Broglie wavelengths of dark matter particles overlap. Finally, we have the Jeans scale ℓ, which sets the size of a gravitational stable superfluid configuration.

Understanding the hierarchy between these scales is fundamental in order to depict the final density profile of the halo. Therefore, in the next sections, we provide a comparison of R_T, $R_{\rm deg}$ and ℓ for different values of the mass m and of the coupling λ.

3.2.1 Comparing R_T and $R_{\rm deg}$: degenerate and non-degenerate thermalization

In this section, we compare the thermal radius R_T and degeneracy radius $R_{\rm deg}$. In particular, we focus on the different physical effects that would emerge when one of these scales is larger than the other.

To do so, it is crucial to define the density distribution of dark matter in galaxies. Following the discussion of Chapter 1, the formation of a dark matter halo is a highly non-linear process and the outcome of the collapse in the absence of baryons is usually approximated with the NFW density profile (1.3), which we report here again for convenience

$$\rho(r) = \frac{\rho_0}{\frac{r}{r_s}\left(1+\frac{r}{r_s}\right)^2}\,. \tag{3.15}$$

Following what takes place in models of self-interacting dark matter, the initial stages of the formation of halos are expected to be analogous to non-self-interacting dark matter [74]. Therefore, the density profile (3.15) should provide a reasonable ansatz for the distribution of

dark matter in the halo *before* self-interactions become efficient enough to reshuffle the density distribution. We consider it as the initial input of the computations that will follow. For the numerical estimates that will follow, we use $M_{\rm DM} = 10^{12} M_\odot$, the concentration parameter $c = R_{\rm V}/r_s = 6$ and the Virial radius $R_V = 200$ kpc, corresponding to the parameters of Milky-Way-like halos.

Both the condition of degeneracy and the formation of a thermal profile are expected to be more easily satisfied in central regions of halos, in which densities are higher than in the outskirts. We start by analysing what are the minimum requirements to have degenerate dark matter in galaxies. In the first approximation, given a density distribution $\rho(r)$, a gas of particles is degenerate if there is more than one particle per de Broglie volume. Therefore, the dark matter halo is degenerate in regions that satisfy the condition

$$r < R_{\rm deg}, \qquad\qquad R_{\rm deg}: \quad n\lambda_{\rm db}^3 \sim \frac{\rho(R_{\rm deg})}{m}\left(\frac{2\pi}{mv}\right)^3 = 1, \tag{3.16}$$

where we defined the degeneracy radius $R_{\rm deg}$ as the distance from the galactic density at which we have exactly one particle per de Broglie volume. As we see, this is uniquely determined by the mass of the dark matter particle. For typical Milky Way-like galaxies, we find

$$R_{\rm deg} \gg 10{\rm kpc} \quad \Longrightarrow \quad m \ll 50\ {\rm eV} \tag{3.17}$$

Let us stress that halos are completely degenerate, so $R_{\rm deg} \gg R_V$, if dark matter particles lighter than 1 eV are considered.

Concerning the region of the halo which is in equilibrium, this is identified by the region within which particle interactions had the chance to interact at least once during the lifetime of the halo. We define the thermal radius R_T, as the radius of this region. The interaction rate plays a central role in determining R_T and its explicit form depends on whether dark matter was already degenerate at R_T or not. This is because, for degenerate particles, the interaction rate is enhanced by the Bose-enhancement factor $\mathcal{N}$, which counts the number of particles in a de Broglie volume. Therefore, the relaxation rate is approximately determined by [72, 75]

$$\Gamma = (1+\mathcal{N})\,\frac{\sigma}{m}\rho v\,, \qquad \mathcal{N} = \frac{\rho}{m}\left(\frac{2\pi}{mv}\right)^3\,, \tag{3.18}$$

where $v(r) = \sqrt{\frac{GM(r)}{r}}$ is the orbital velocity of dark matter particles, $M(r)$ is the mass of the halo enclosed in an orbit of radius r, and σ/m is the two-body scattering cross section determined by

$$\frac{\sigma}{m} = \frac{\lambda^2}{128\pi m^3}. \tag{3.19}$$

Notice that we use interchangeably v to indicate the velocity and the velocity dispersion, which we assume are of the same order. As we see, if particles are not degenerate, the relaxation rate reduces to the standard 2-body scattering rate in vacuum. However, if the condition of degeneracy is satisfied, the relaxation rate is boosted by a factor of $\mathcal{N}$.

According to what we said, the thermal radius is defined as the radius within which particles had the chance to scatter at least once in the lifetime of the halo [74]. Assuming $t_g \sim 13\,\mathrm{Gyrs}$, we have

$$R_T : \qquad \Gamma|_{r=R_T} t_g = 1, \tag{3.20}$$

where t_g is the age of the halo. One could question if using t_g as the time scale for thermalization is a good working assumption. What we are implicitly assuming is that it is possible to ignore the phase-space reshuffling of Φ due to dynamical effects within the galaxy. If this is not justified, the dynamical time $t_{\rm dyn} = r/v$ is more appropriate to determine the thermal radius. However, it was shown in [78] that the qualitative picture of the discussion would stay the same if we repeat the analysis using the dynamical time.

Now, superfluidity takes place within the smaller radius among R_T and $R_{\rm deg}$. We identify the two cases of *degenerate* and *non-degenerate thermalization*, depending on the relation of these two scales.

(i) If $R_T > R_{\rm deg}$, then the relaxation rate of the system at R_T is approximated by the standard 2-body interaction rate in the vacuum. The evolution of the phase space would track the one of non-degenerate self-interacting dark matter models. The final structure of the halo would contain three phases: an outskirt $r > R_T > R_{\rm deg}$ of non-degenerate particles with a non-equilibrium phase space distribution, a non-degenerate intermediate region $R_T > r > R_{\rm deg}$ in which particles would have the chance to experience interactions, and a central region within $r < R_{\rm deg} < R_T$ where the superfluid phase transition would take place.

(ii) If $R_{\rm deg} > R_T$, the relaxation rate is boosted by the degeneracy factor. The structure of the halo is simpler in this case and it is comprised of an outskirt of degenerate particles which did not have the chance to interact and a central superfluid region.

We study these two scenarios separately in the following subsections.

Case (i) Non-degenerate Thermalization

In the first case, the dark matter gas reaches equilibrium *outside* the region in which particles are degenerate, that is $R_{\rm deg} < R_T$. In this case, the thermal radius R_T is determined by solving the equation

$$\Gamma t_{\rm g} = \frac{\sigma}{m}\rho(R_T)v(R_T)t_{\rm g} = 1\,. \tag{3.21}$$

In the case of non-degenerate thermalization, the thermal radius is only a function of σ/m. Concerning the dependence of (3.21) of the NFW profile, this is a non-linear function of R_T, ρ_0 and r_s. However, it simplifies if we focus on the two relevant regimes $R_T \ll r_s$ and $R_T \gg r_s$

$$R_T \simeq r_s\Big(\rho_0 r_s\sqrt{2\pi G\rho_0}\frac{\sigma}{m}t_{\rm g}\Big)^{\gamma}, \quad \text{with} \quad \gamma = \begin{cases} 2, & \text{for } R_T \ll r_s \\ 2/7, & \text{for } R_T \gg r_s \end{cases} \tag{3.22}$$

Notice that if $R_T \ll r_s$, the ratio R_T/r_s is a sensitive function of the density profile. Therefore, different initial density distributions could significantly change this ratio.

As expected, for larger σ/m, the dark matter gas reaches equilibrium at lower densities. By using the typical NFW parameters of a Milky-Way-like galaxy and the average density $\rho \simeq 10^{-25}\text{g/cm}^3$, we find the following compact expression for the thermal radius:

$$R_T^{\rm MW} \simeq r_s \left(\frac{\sigma/m}{\text{cm}^2/\text{g}}\right)^{\gamma} \tag{3.23}$$

Although it would seem that only σ/m determines the thermal radius R_T, the relation holds as long as $\mathcal{N}$ is small at R_T, so it holds for dark matter masses significantly heavier than the eV scale.

This is the important message: given masses above the eV-scales, we can already understand what kind of superfluid solitons we may expect in the superfluid region, assuming the maximum interaction cross-section $\sigma/m \sim 1\ \text{cm}^2/\text{g}$. This is the value that saturates the bullet cluster bound and we derive again in the second part of this chapter. By plugging in these values in (3.8), we get that a stable superfluid soliton cannot be bigger than

$$\ell \lesssim 5 \cdot 10^{-2}\ \text{pc}\,. \tag{3.24}$$

which is roughly the size of the solar system. In other words, if we want to consider coherence lengths which have an astrophysical size, we cannot rely on non-degenerate thermalization.

Case (ii): Degenerate Thermalization

The second scenario we want to explore involves the possibility that $R_{\rm deg} > R_T$. This implies that we have to consider particles which are lighter than the eV-scale. The derivation of the thermal radius tracks the previous case, with the only difference that we have to use the interaction rate for degenerate particles

$$\Gamma t_{\rm g} = \frac{\sigma}{m}\rho(R_T)v(R_T)\mathcal{N}t_{\rm g} = 1\,, \quad \text{with} \quad \mathcal{N} = \frac{\rho}{m}\left(\frac{2\pi}{mv}\right)^3 \gg 1\,. \tag{3.25}$$

We may consider the two limiting cases

$$R_T \simeq r_s \left(\frac{4\pi^2\rho_0}{Gm^4 r_s^2}\frac{\sigma}{m}t_{\rm g}\right)^{\delta}\,, \quad \text{with} \quad \delta = \begin{cases} 1/3, & \text{for } R_T \ll r_s \\ 1/5, & \text{for } R_T \gg, r_s \end{cases} \tag{3.26}$$

which, for a Milky Way-like halo, reduces to

$$R_T^{\rm MW} \simeq \begin{cases} 60 \cdot r_s \left[\frac{\sigma/m}{\text{cm}^2/\text{g}}\left(\frac{m}{\text{eV}}\right)^{-4}\right]^{1/3}, & \text{for } R_T \ll r_s \\ 10 \cdot r_s \left[\frac{\sigma/m}{\text{cm}^2/\text{g}}\left(\frac{m}{\text{eV}}\right)^{-4}\right]^{1/5}, & \text{for } R_T \gg r_s \end{cases} \tag{3.27}$$

Notice that for degenerate dark matter, the combination of parameters that regulates the size of the thermal core is $(\sigma/m)\, m^{-4}$, as it was previously shown in [56]. Also, in the case of non-degenerate thermalization, the ratio R_T/r_s is mildly dependent on the NFW parameters r_s and ρ_0. Therefore, this result is not expected to be sensitive to a fine-tuning of the NFW parameters.

As we are going to show in the next section, for sub-eV masses it is possible to consider slices of the parameter space in which ℓ is kpc-sized.

3.2.2 Comparing the R_T and ℓ: gravitational stability of the superfluid phase

The parameter space which is favourable for generating macroscopic superfluid solitons is the one in which thermalization takes place in a degenerate environment. We focus on this case and, to keep the analysis compact, we consider the scenario in which the whole halo is degenerate ($R_{\rm deg} > R_V$), implying that dark matter particles are sub-eV.

The second (and most important) comparison we have to make concerns the thermal radius R_T and the Jeans scale ℓ. Depending on the hierarchy of the two scales, we have the two following scenarios

- If $\ell > R_T$, so if thermal equilibrium is established in scales smaller than the scale of gravitational stability, a stable superfluid core of size R_T would form in inner regions of the dark matter halo. However, as we will demonstrate, this scenario cannot take place if the main contributor to the pressure responsible for stabilizing the core is the interaction pressure.

- If $\ell < R_T$, the region of the halo which is in equilibrium is wider than the size of a stable superfluid soliton. Therefore, the thermal core is gravitationally unstable and prone to fragmenting in a collection of superfluid solitons due to Jean's instability.

In the interaction pressure regime ($\xi \gg 1$) the Jeans scale and the thermal radius depend on different combinations of λ and m. Nevertheless, the case $\ell > R_T$ is precluded and only the case in which the thermal core is unstable is physical. We can see this from Fig 3.2. There, the Jeans scale ℓ (black lines) and the thermal radius R_T (coloured lines) are plotted for different values of m and λ. The flat part of the Jeans scales corresponds to the quantum pressure case ($\xi \ll 1$), while the tilted part is the interaction pressure case ($\xi \gg 1$). It can be observed that the scenario where $\ell > R_T$ takes place only for Jeans scales which are quantum pressure dominated. Also, this outcome is not dependent on the specific definition of the thermal radius we have employed: shaded coloured regions illustrate how the thermal radius would be affected if we change the minimum number of scatterings needed to define R_T, in the range 1-10. As we can see, the result is qualitatively similar.

To conclude, a thermalized region of size R_T within the model and the parameter space at hand is unstable and prone to fragmenting in a collection of superfluid droplets due to gravitational instability.

3.2.3 Tidal effects

According to the analysis of the previous section, the thermal core is prone to fragmenting in a collection of superfluid droplets of size $\sim \ell$. Nevertheless, this analysis assumes that the spectrum of perturbations of the superfluid solution is determined, with good approximation, by (3.4).

An underlying assumption that was made in [77] to derive the phonon spectrum in the presence of gravity is that the superfluid bulk is self-gravitating and is not affected by any external

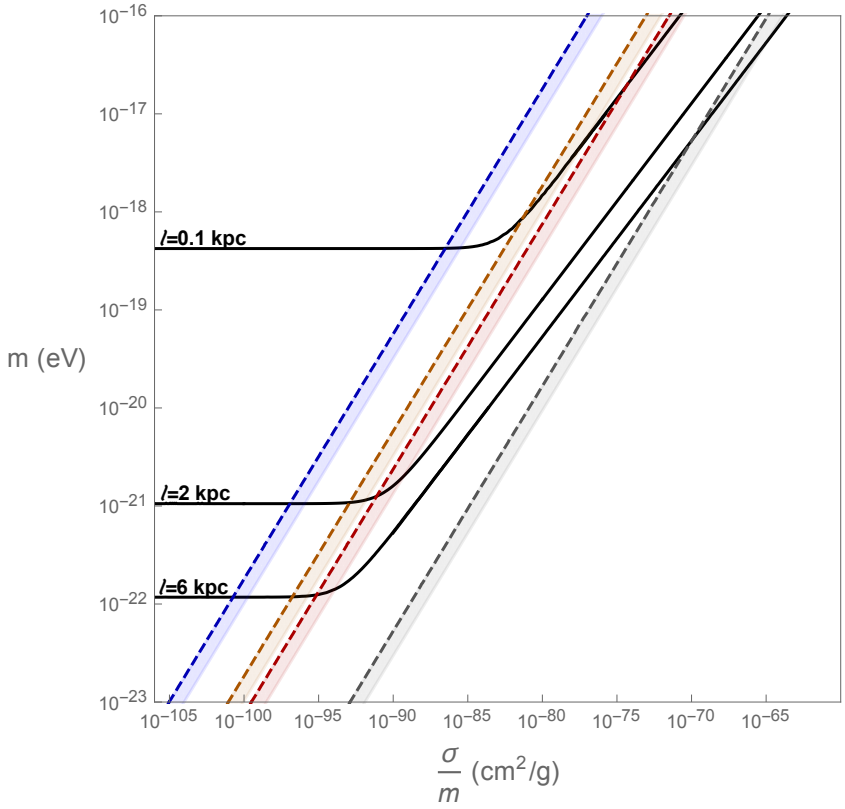

Figure 3.2: In this figure, the thermal radius and the Jeans scale are compared for different values of the mass m and the scattering cross section σ/m. Black lines represent the parameter space that gives a Jeans scale of 0.1 kpc/ 2 kpc/ 6 kpc in degenerate regions of the Milky Way dark matter halo, assuming a particle species governed by the Lagrangian (3.1). These lines are obtained by a numerical evaluation of the Jeans scale (3.5). The tilted part of the curve represents the interaction pressure regime of the theory ($\xi \gg 1$), while the flat part ($\xi \ll 1$) is the degeneracy pressure regime. Blue/Orange/Red dashed curves correspond to the parameter space in which the thermal radius is 0.1 kpc/2 kpc/6 kpc respectively. The portion of a specific ℓ line that resides to the left of the corresponding R_T line gives the parameter space of gravitationally stable thermal cores. As we can see, only flat segments fall within this regime, implying that the existence of stable thermal regions is feasible only if $\xi \ll 1$. Coloured shaded regions show how R_T changes if we vary the number of scatterings that each particle has to undergo to achieve equilibrium, in the range 1-10. On the right of the grey line, the Milky Way dark matter halo is in global thermal equilibrium.

potential. While this assumption is reasonable for superfluid solitons residing in the galactic centre, solitons which are far enough in the outskirts of the halo feel the gravitational potential of the ones within their orbit. Consequently, these solitons experience tidal forces that, as we will demonstrate, significantly impact their dynamics, ultimately resulting in efficient tidal disruption.

To quantify these effects, it is useful to revisit what tidal forces are. In a two-body system, tidal forces are gravitational effects that stretch the bodies along the line connecting their centres of mass. Tidal effects are particularly effective when one of the two bodies is more massive than the other. In the extreme case, if tidal forces are sufficiently strong, the less massive body can undergo tidal disruption, since its own gravitational field is not strong enough to prevent its parts from being torn away by the more massive companion body.

To quantify the strength of these effects, it is convenient to introduce the tidal radius $r_{\rm tid}$, which quantifies the strength of the tidal field of a body of mass M on a lighter body of mass m. This reads [98]

$$r_{\rm tid} = r \left(\frac{m}{M}\right)^{1/3} \tag{3.28}$$

and it determines the size of a body which is stable under tidal deformations. In particular, tidal disruption takes place if the size of the lighter body is bigger than the tidal radius itself [5]. If we apply the definition of tidal radius (3.28) to the setup we are studying, tidal forces are strong enough to shatter a soliton if $r_{\rm tidal} > 0.5\,\ell$. The result of this process is the disruption of the soliton into a collection of superfluid debris.

To estimate the tidal radius, let us consider a soliton orbiting at a radial distance r from the galactic centre. This soliton is affected by the tidal interactions with all the other solitons and debris which are enclosed within its orbit and we quantify these effects by introducing the effective mass $M = M(r)$. This effective mass is a key parameter in determining the efficacy of tidal effects in erasing solitons.

Concerning the mass of the soliton, this is simply obtained by integrating the density distribution (3.13) up to ℓ. The result reads

$$m_{\rm soliton} = \frac{\rho_{\rm soliton}\ell^3}{2\pi}. \tag{3.29}$$

But what mass distribution should we consider for evaluating $M(r)$? We assume it resembles a course-grained version of the NFW profile we started with. This assumption can be justified as follows: while we have described the formation of superfluid solitons as a simplified sequence of three events—thermalization, phase transition, and fragmentation of the thermal core—in reality, these processes are expected to occur concurrently. Small high-density regions of the halo are anticipated to thermalize, become superfluid, and merge, eventually forming solitons of size ℓ. Thermalization continues to affect regions of lower density, giving rise to additional solitons.

[5] While tidal disruption may not occur immediately when $r_{\rm size} \lesssim r_{\rm tidal}$, it is important to note that tidal deformations can still take place. In cases of significant deformation, after several cycles, the orbiting probe can become stretched to the extent that its size along the stretched direction approaches that of the tidal radius. This can ultimately result in the shattering of the body. This effect has been studied in FDM solitons orbiting in a Navarro-Frank-White profile [99].

Therefore, we expect that the average density of each soliton is connected to the local density of the halo in which it formed. Since we initially used the NFW profile as our input, it is reasonable to assume that the course-grained density distribution of the superfluid droplets within a radius r would also follow an NFW-like profile.

With this assumption, the ratio of the tidal radius over the Jeans scale approximately reads

$$\frac{r_{\rm tidal}}{\ell} \simeq \left(\frac{\rho_{\rm soliton}}{40\rho(r)}\right)^{1/3}. \tag{3.30}$$

In other words, solitons which are stable are the ones that have a central density which is at least 40 times the mean density of the environment in which they form. However, this assumes that none of them would move around and eventually cross the galactic centre. Assuming random motion, a better estimate is that stable solitons should satisfy the condition

$$\rho_{\rm soliton} > 40\rho_0 \tag{3.31}$$

to not being tidally disrupted, where ρ_0 is the NFW characteristic density.

3.2.3.1 Survival rate of solitons

The final step is to apply this analysis to the collection of solitons residing in the Milky Way halo. In particular, one could ask how many of these solitons are expect to survive.

In general, it is possible to associate any unstable mode of momentum $k < k_J$ — as given by the dispersion relation (3.4) — with a length scale R. The mass encompassed within this scale is precisely what would end up in forming a specific soliton of size ℓ. Therefore, the longer is R, the heavier the soliton formed from the collapse of the fluctuation will be. However, fluctuations $R > \ell$ are exponentially suppressed if compared to fluctuations of size ℓ, so that heavy solitons are extremely unlikely to form [91].

If we make the assumption that the formation of a soliton occurred through the collapse of a self-gravitating sphere and that tidal effects come into play at a later stage, we can deduce the peculiar length R_* which would result in a tidally stable soliton. To do that, we equate the mass contained in a fluctuation of size R_*, to the one of a stable soliton. We find

$$M_{\rm fluct} \simeq \rho_{\rm NFW}(r)R_*^3 = \frac{40\rho_0\ell^3}{2\pi} = m_{\rm soliton} \Longrightarrow R_* \geq 2\ell, \tag{3.32}$$

where we implemented the relation (3.31) after the second equality. Therefore, we see that fluctuations which are slightly larger than the Jeans scale would result in stable solitons. Of course, this assumes that $\rho_{\rm nfw}(r)$ is of order ρ_0, which only takes place in inner regions of the halo. As solitons start forming in the outskirts, the starting density would be an order (or two) of magnitude smaller than ρ_0, so that, the minimum stable fluctuation becomes $R_* \sim 4$ and only extremely large (and statistically unlikely) fluctuations would form stable solitons.

Finally, let us say that the process of forming solitons is a highly non-linear problem and its analysis has to be approached numerically. In particular, the working assumption that tidal effects are not affecting the collapse is unrealistic for most of the solitons, since both the collapse

and tidal disruption take place on the same time scale $\ell \simeq 1/\sqrt{G\rho}$, making the previous analysis not applicable for this scenario. However, in this case, we expect that tidal effects should be even more important and could also prevent the soliton forms in the first place, as the dynamics of the collapse could be highly distorted once compared to the self-gravitating ideal case. Also, the collapse of a homogeneous configuration could not be completely appropriate to describe the formation of self-gravitating solitons of kpc-size, since the original NFW profile may not be considered as a homogeneous configuration over these scales. We leave a more detailed analysis of these shortcomings to future works, where the dynamics of these solitons is numerically implemented.

Therefore, the final picture is that only one (or a few) central solitons are expected to survive, while the ones that would be formed in the outskirts are expected to be efficiently tidal disrupted into a collection of superfluid debris.

3.3 Bounds

Before summing up the final picture, we explore the constraints that can be imposed on the parameter space of the model. Self-interactions are extremely important in characterizing the superfluid phase of the halo, but several astrophysical and cosmological bounds can be put on their strength. In this section, we study how these would translate into bounds on the properties of the superfluid solitons.

3.3.1 Bounds from the Bullet Cluster

The most famous astrophysical constraint on the strength of dark matter self-interactions is derived from the analysis of the Bullet Cluster [100–102]. This is a system of two merging clusters, in which the main one, the *target*, collided with a smaller one, the *bullet*. The result of the collision is an offset of the gas component with respect of the dark matter component of each cluster. The main interpretation that allows us to reproduce the setup is that the dark matter component did not interact during the collision, differently from the gaseous component.

In terms of the microscopical properties of dark matter, this is possible if the mean number of scatterings that a dark matter particle from the bullet cluster underwent while crossing the target cluster was smaller than one

$$\langle n_{\rm sc} \rangle < 1, \tag{3.33}$$

where the mean number of scatterings is averaged over all the bullet cluster dark matter particles. The mean number of scatterings is estimated in terms of the scattering rate Γ as

$$\langle n_{\rm sc} \rangle = \Gamma \frac{2R_{\rm V}}{v_{\text{in-fall}}}, \tag{3.34}$$

where $v_{\text{in-fall}} \simeq 10^{-2}$ is the in-fall velocity and $R_{\rm V} \simeq 2\,$Mpc is the target cluster virial radius. For the incoming estimates, we assume a characteristic mean density of $\rho_{\rm NFW} = 10^{-25}\text{g/cm}^3$, which is the average density of the target cluster within 500 kpc from its centre [103].

Now, a crucial point is the interaction rate that enters in (3.34). If dark matter that comprises the bullet and target cluster halo is not degenerate, then the interaction rate is determined by the standard 2-body scattering rate in the vacuum. By plugging this relation in (3.34) and by evaluating it for typical cluster parameters, we find the well-known bound

$$\frac{\sigma}{m} \lesssim 1 \frac{\text{cm}^2}{\text{g}}, \qquad \text{if} \quad \Gamma = \frac{\sigma}{m} \rho \, v_{\text{in-fall}}. \tag{3.35}$$

However, if the dark matter mass is lighter than a few eV, dark matter particles are expected to be degenerate in the cluster halos. This implies that the interaction rate which regulates the evolution of the bullet cluster event is enhanced by the Bose enhancement. This property affects the bullet cluster bound by introducing an additional factor of $\mathcal{N}$ in the interaction rate. The bullet cluster bound for degenerate particles reads

$$\frac{\sigma}{m} \lesssim \frac{1}{\mathcal{N}} \frac{\text{cm}^2}{\text{g}} \simeq 10^{-2} \left(\frac{m}{\text{eV}}\right)^4 \frac{\text{cm}^2}{\text{g}}, \qquad \text{if} \quad \Gamma = \mathcal{N} \frac{\sigma}{m} \rho \, v_{\text{in-fall}}. \tag{3.36}$$

It is important to question to what extent this enhanced version of the bullet cluster bound is applicable. Although the degeneracy of dark matter can enhance self-interactions, this is true as long as the degenerate outskirt comprises the majority of the dark matter of the halo. However, if most of the dark matter is in the superfluid phase, this condition does not occur. We have already seen this scenario back in Section 2.3.3 - 2.3.4, where the rate of a particle scattering over a superfluid background (2.37) *was not Bose enhanced*. Therefore, we expect that the enhanced bullet cluster bound relaxes to the ordinary non-degenerate version if self-interactions are efficient enough that the majority of particles in the halo had the chance to interact several times. As a rough estimate, we may expect that this takes place if $R_T > R_V^{\text{cluster}}$, which is achieved if the cross-section is stronger than $\frac{\sigma}{m} > 3 \left(\frac{m}{\text{eV}}\right)^4 \frac{\text{cm}^2}{\text{g}}$.

We sum the bullet cluster bound for sub-eV particles in the following way

- Cross sections smaller than

$$\frac{\sigma}{m} \lesssim 10^{-2} \left(\frac{m}{\text{eV}}\right)^4 \frac{\text{cm}^2}{\text{g}} \tag{3.37}$$

  are allowed. In this case, only the central part of the halo is in thermal equilibrium, while the outskirt of the halo is still degenerate, but not thermal.

- Cross sections in the regime

$$10^{-2} \left(\frac{m}{\text{eV}}\right)^4 \frac{\text{cm}^2}{g} \lesssim \frac{\sigma}{m} \lesssim 3 \left(\frac{m}{\text{eV}}\right)^4 \frac{\text{cm}^2}{g} \tag{3.38}$$

  are NOT allowed. In this case, halos of clusters have a non-negligible degenerate dark matter component, which during cluster collisions would not behave as a collisionless fluid.

- Cross section in the regime

$$3\left(\frac{m}{\mathrm{eV}}\right)^4 \frac{\mathrm{cm}^2}{g} \lesssim \frac{\sigma}{m} \lesssim 1\,\frac{\mathrm{cm}^2}{\mathrm{g}} \tag{3.39}$$

  are also allowed. In this case, the halo is completely in the superfluid phase, with a central region comprised of a superfluid core and an outskirt of superfluid debris. The interaction rate is not enhanced by $\mathcal{N}$ due to the specific dark matter phase space distribution of this scenario.

3.3.2 Bounds from Matter Radiation Equality

A complementary bound on the strength of self-interactions is derived from the analysis of the pressure sustained by the cosmological dark matter condensate during recombination.

Large scale structure formation and the analysis of the cosmic microwave background support the idea that dark matter had to behave as dust at matter radiation equality. For the model at hand, if particles were produced by vacuum misalignment [104–106], then we have to ask that the cosmological condensate had to be non-relativistic at that time. This is equivalent to asking that

$$\frac{P}{\rho}\Big|_{\text{equality}} = \frac{\lambda\rho_{\text{equality}}}{8m^4} \ll 1, \qquad \Rightarrow \qquad \frac{\sigma}{m} \ll \left(\frac{m}{2\times 10^{-5}}\right)^5 \frac{\mathrm{cm}^2}{\mathrm{g}}. \tag{3.40}$$

Notice that this represents a bound on the maximum Jeans scale *today*. We can see this because the constraint (3.40) is also a constraint on the sound speed of the condensate at recombination. However, the bound on the Jeans scale is extremely mild and gives $\ell \lesssim \mathcal{O}(100)$ kpc.

A complementary, yet stronger, bound, comes from the analysis of large scale structure formation. In particular, to reproduce the correct matter power spectrum, the beginning of structure formation requires the presence of the pressureless dark matter as early as when baryons had a temperature $T \sim$ keV. Of course, this provides a bound which is stronger than (3.40). In particular, the maximum Jean's scale allowed would shrink down to

$$\ell \lesssim 10\ \text{kpc}. \tag{3.41}$$

This is motivated by the numerical analysis [107], which concluded that the Jeans scales bigger than $\ell > 1$ kpc are disfavored at the 2.4σ level. Nevertheless, differently from the bullet cluster bound, both the constraints from matter radiation equality and structure formation assume a specific evolution history of the condensate. In particular, it is fundamental that dark matter behaved as a cosmological scalar field starting from its production up to today. Also, these bounds rely on the production mechanism. In other words, it is possible to overcome these bounds, if the evolution history of the dark matter candidate is found to be different between today and the temperature $T \sim$ keV.

3.3.3 Evaporation of the dark matter condensate

The last bound we want to consider concerns the evaporation of the scalar condensate due to quantum effects. As we will elaborate in the following chapter, the analysis we performed here

assumes that the classical solution that approximates the superfluid background provides a good description of the system for any given duration. However, this assumption cannot be extended arbitrarily, due to the intrinsic quantum properties of the setup we are studying.

A superfluid can be considered as a condensate of zero momentum bosons. If we consider *real* bosons, then processes in which four zero-momentum bosons annihilate into two relativistic particles are allowed. This class of number-changing processes can drain the number of constituent particles of the condensate phase, by transforming them into radiation. The time scale for which these effects become dominant is the *quantum break-time*, which for the system at hand is given by [108–110]

$$t_{\rm q.b.}^{-1} = \lambda \left(\frac{\lambda n}{m^3}\right)^3 m. \tag{3.42}$$

This sets the time scale after which quantum effects drained an order one fraction of the classical solution, and the approximation we used to study the setup cannot be trusted anymore.

In principle, one should evaluate the effect of the evaporation of the condensate along the full evolution history of the condensate, from the matter equality up to today. However, to provide a conservative and more simple bound, we impose that the quantum break time satisfies the bound

$$t_{\rm q.b} < t_{\rm equality} \quad \Rightarrow \quad \left(\frac{\sigma/m}{\rm cm^2/g}\right) \ll \left(\frac{m}{4\cdot 10^{-6}\ {\rm eV}}\right)^{5/2}, \tag{3.43}$$

where we considered typical galactic densities to derive the bound on the right. Notice that this bound is not applicable if the dark matter superfluid is made up of complex scalar bosons.

3.4 Final Picture

Finally, we are ready to sum up the expected density distribution of superfluid dark matter in halos, as depicted in the previous sections.

- The region $r \lesssim \ell$ of the halo hosts the central superfluid soliton. By assuming a central density of $\rho_0 \sim 10^{-25}{\rm g/cm}^3$, the mass of the central soliton is expected to be

$$M \simeq 2\times 10^5 \left(\frac{\ell}{\rm kpc}\right)^3 M_\odot. \tag{3.44}$$

- The region $\ell \lesssim r < R_T$ of the halo is comprised of streams of superfluid debris originating from the tidal disruption of outer solitons. These debris behave as non-interacting objects since the interaction between condensates should not be Bose-enhanced, unless a consistent degenerate and out-of-equilibrium fraction of dark matter is generated by the disruption of solitons. Because of the non-interacting nature of these fragments, the course-grained density distribution of this region should resemble an NFW profile. This region also hosts solitons that are dense enough to not be tidally disrupted.

- In the region $R_T \lesssim r \lesssim R_V$, dark matter particles did not have the chance to interact once during the lifetime of the halo. Their velocity distribution is similar to the one of standard Cold Dark Matter, although with a highly degenerate phase space (due to the sub-eV mass range). This is the region responsible for the enhanced bullet cluster bound since the interaction of these regions in cluster collisions would be enhanced by the out-of-equilibrium phase space. If clusters are in equilibrium ($R_T > R_V$), this region is absent and the bullet cluster bound relaxes to its non-degenerate counterpart.

Finally, let us discuss the parameter space of the theory. Figure 3.3 displays different values of the Jeans scales for various values of the mass and the cross-section. Specifically, the solid, dashed, and dotted lines correspond to parameter spaces for which the Jeans scale is equal to $\ell = 30$ kpc, $\ell = 2$ kpc, and $\ell = 0.1$ kpc, respectively. Furthermore, the green region delineates the parameter space wherein the main component to the ground state pressure is the *quantum pressure*. In this regime, dark matter halos are similar to the ones described by models of Fuzzy dark matter and therefore are not considered in this work.

Concerning regions excluded by the bounds highlighted in the previous sections, the light and dark purple regions are excluded by the bound (3.40) and (3.43) respectively. The first corresponds to condensates that are relativistic at matter radiation equality. If we demand that condensates had to be non-relativistic already at $T =$ keV, then the excluded region is extended up to in between the dashed and solid black lines. The dark purple region corresponds to condensates that would have evaporated into dark radiation and only applies to condensates comprised of real scalar bosons.

Finally, the red stripe corresponds to the bullet cluster bound. Here, we can identify two allowed sub-regions. The white region on the left of the stripe corresponds to halos in which only central regions present a superfluid phase. In this case, we have that $R_T < R_V$ and only cores up to $\ell \sim 6$ kpc are allowed. Bigger values are not allowed by the bullet cluster bound unless the halo is completely in equilibrium. The white region of the right side corresponds to dark matter halos which are completely in equilibrium ($R_T > R_V$). In this case, Jeans scales up to $\mathcal{O}(100$ kpc), as long as the bullet cluster bound can be relaxed for halos in global thermal equilibrium. If the bound from structure formation is invoked, then the maximum ℓ is 10 kpc.

3.5 Addressing small-scale problems with dark matter superfluidity

Finally, we show that the properties of the superfluid phase and the density profile depicted in the previous section can address and ameliorate the core-cusp problem and the excess of substructure predicted by CDM.

3.5.1 Core-cusp problem and Rotation curves

One of the main implications of dark matter superfluidity is its potential to ameliorate the core-cusp problem by introducing an effective positive pressure, sourced by the condensed phase of

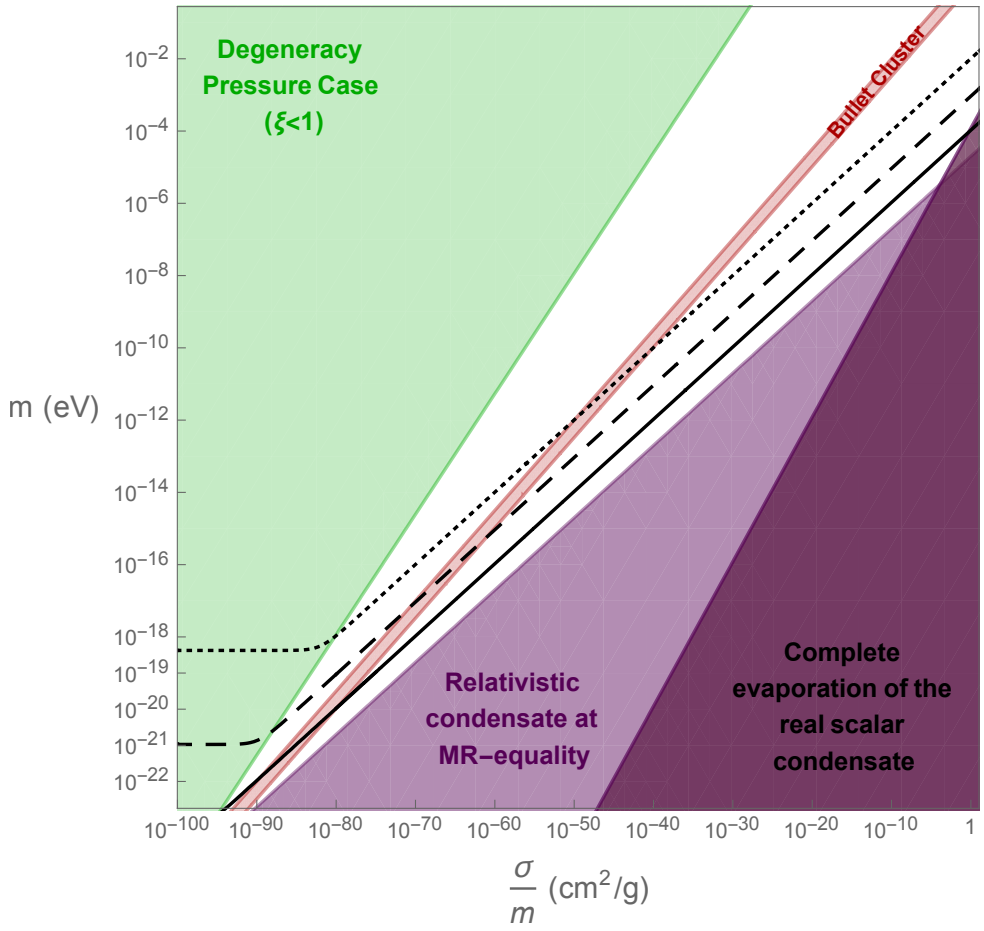

Figure 3.3: Parameter space of the model (3.1). Solid/Dashed/Dotted line represents the parameter space for which ℓ is 30 kpc/2 kpc/0.1 kpc, respectively. The green region gives condensate in which the Jeans scale is determined in the degeneracy pressure regime. The red stripe is excluded by the bullet cluster bound. The light purple region is excluded by the condition that the dark matter condensate was non-relativistic at matter radiation equality. The dark purple region is excluded by the condition that the condensate was not evaporated completely at matter radiation equality.

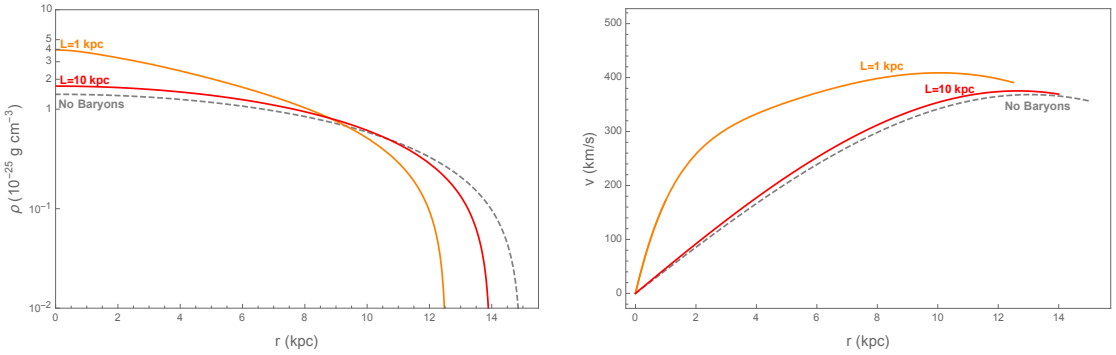

Figure 3.4: Left Panel: Dark Matter density profile of the central soliton. In this figure, we analyse three distinctive cases. The first is the soliton in the absence of without (dashed grey), which matches the density profile (3.13). Then we introduce baryons, which we describe using the spherical-exponential profile (3.45). Here, we consider the cases $L = 1$ kpc (orange) and $L = 10$ kpc (red), corresponding respectively to a cusped and quasi-homogeneous baryonic distribution. Right panel: Rotation curves derived from the dark matter density distribution in the left panel.

dark matter and by self-interactions. In particular, the presence of one or a few central superfluid solitons within galactic halos is expected to transform cusped density profiles, typical of Cold Dark Matter halos, into flatter and cored profiles, in a similar way to models of Fuzzy Dark Matter. An interesting implication of the quartic model considered in the chapter is that the size of the central soliton is independent of its central density. This can be exploited to explain the contrasting phenomenology observed in the rotation curves of Milky Way-like galaxies and dwarf galaxies [111], as depicted in Chapter 1.

To provide an explicit example, we consider a set of parameters that gives a Jeans scale $\ell \sim 30$ kpc, corresponding to superfluid solitons of radius $r \sim 15$ kpc. Notice that in order to consider solitons of this size, clusters should be in global thermal equilibrium in order to avoid the enhanced bullet cluster bound. Now, concerning Milky-Way-like galaxies, this would imply that rotation curves would display a mild rise in the first $\sim \mathcal{O}(10)$ kpc (corresponding to the central core) and then become flat once entering the outskirt of degenerate superfluid debris. However, the case of dwarf galaxies would be completely different, as the central core of small halos would comprise the majority of the dark matter of the halo and rotation curves would only have the linearly growing part. This would represent the the Low Surface Brightness (LSB) galaxy IC2574 depicted in Fig 1.1, in which the baryonic component is faint and diffuse.

However, this would not explain the different shapes of rotation curves displayed by dwarf galaxies in Fig 1.1. In the context of Dark Matter superfluidity in small halos, it is important to characterize the distribution of baryons. To illustrate this point, we introduce the toy baryonic distribution [56]

$$\rho_{\text{baryon}}(r) = \frac{\gamma}{4\pi L^3} e^{-r/L}. \tag{3.45}$$

This is a two-parameter exponential profile, with L representing the 'scale radius' of the distribution and γ the total mass of the system. We focus on the two specific cases $L = 1$ kpc

and $L = 10$ kpc, corresponding to a cusped and a quasi-homogeneous baryonic distribution, respectively. Also, we fix the central density of the dark matter soliton and of the baryonic distribution, in such a way that the enclosed mass in the soliton satisfies $M_{\rm baryon} = 2 \times 10^9 M_\odot$ and $M_{\rm dark\ matter} = 10^{10} M_\odot$, which are the fitted baryon and dark matter mass of the LSB galaxy IC2574 [112].

Having introduced all the ingredients (dark matter and baryons), we study how the density profile of the central soliton changes if we introduce the baryon distribution (3.45). Although we cannot track the dynamics of the gas of superfluid debris analytically that resides outside the central soliton, being this a highly non-linear problem, the density distribution of the central superfluid core in the presence of baryon can be studied by solving the equation for hydrostatic equilibrium and the Poisson equation

$$\Delta\Phi = 4\pi G \left(\rho_{\rm dm} + \rho_{\rm baryon}\right) \tag{3.46}$$

$$\frac{1}{\rho_{\rm dm}} \frac{dP}{dr} = -\vec{\nabla}\Phi \tag{3.47}$$

The numerical solutions are given in the figures 3.4 and 3.5. In the left panel of Figure 3.4, different density profiles are given for different baryonic distributions. The grey line corresponds to a central soliton without baryons, while the orange and red lines are, respectively, in the presence of a cusped quasi-homogeneous baryon distribution. As expected, the more concentrated the baryons are, the more the soliton shrinks and the central density increases. The effect on rotation curves is given in the right panel of the analogous figure. As we can see, for quasi-homogeneous baryon distribution, rotation curves rise slowly, in a similar way to dark matter only solitons. However, once a central baryon distribution is introduced, we see a sharp rise followed by a quasi-flat part. In Fig.3.5, partial contributions to the orbital velocity are given. As we can see, in the case of spiked distributions, the sharp rise is mostly driven by baryons, while in the outer part, the dark matter catches on. In the case of quasi-homogeneous baryonic distribution, the effect of baryons is always subleading. Therefore, the way of accounting for the variety of rotation curves is similar to the case of SIDM [26], where the presence of baryons in central regions erases the quasi-homogeneous region generated by dark matter interactions.

3.5.2 Efficient erasure of substructures from hierarchical structure formation

To address the problem of the missing satellites, we notice that the positive pressure sourced by self-interactions, combined with tidal effects, is extremely efficient in erasing substructure from hierarchical structure formation.

According to the discussion of the previous sections, structure formation is expected to proceed in a similar way to standard dark matter, since the effect of self-interactions is negligible at cosmological scales. Numerical simulations for CDM and SIDM [26, 113] predict that the mass function of resolved subhalos within a host galaxy spans over the range 4.5 km/s $< V_{\rm max} <$ 40 km/s, where $V_{\rm max}$ is the maximum subhalo circular velocity. We can read these data from Fig

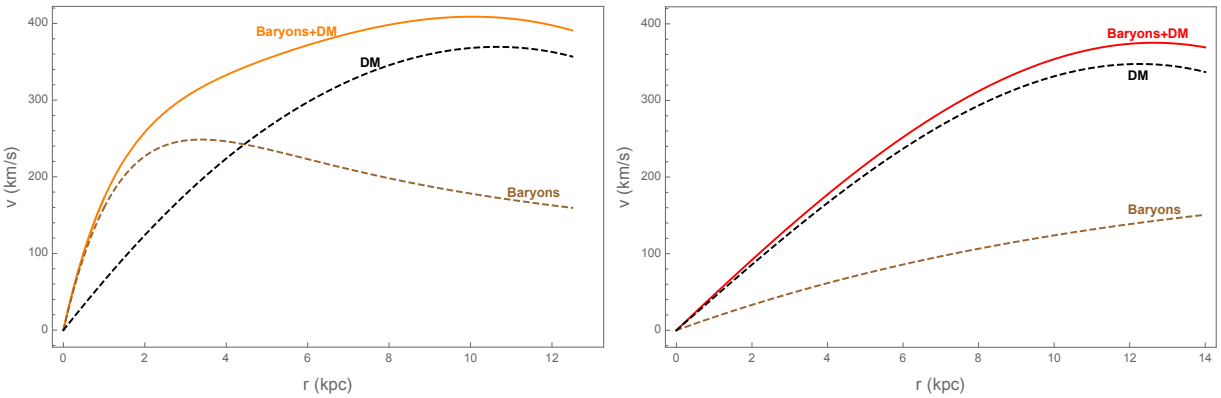

Figure 3.5: Dark matter and baryon partial contributions to the rotation curves, for $L = 1$ kpc (Left) and $L = 10$ kpc (Right).

1.1. By converting this in terms of the subhalo mass, we get that the expected mass range of these substructures is

$$5 \times 10^6 M_\odot \lesssim M_{\text{sub-halos}} \lesssim 5 \times 10^7 M_\odot \tag{3.48}$$

These structures form way before the superfluid phase transition takes place and, as time proceeds, their dark matter content reaches equilibrium. Eventually, the phase transition takes place and the density profile of the subhalos relaxes to (3.13). Being small, the dark matter content of these subhalos is expected to be located in a single core.

However, based on the constraint (3.31), only solitons which are massive enough can survive tidal disruption in the host halo, with the mass threshold determined by

$$M > \frac{40\rho_0}{2\pi}\ell^3 \quad \Longrightarrow \quad M > 10^7 \left(\frac{\ell}{\text{kpc}}\right)^3 M_\odot. \tag{3.49}$$

This implies that, if the Jeans scale is bigger than a few kpc, almost all substructures from hierarchical structure formation would be efficiently tidally disrupted once captured by the host galaxy.

Chapter 4

Coherent States and the Quantum Dynamics of Highly Occupied Systems

In the previous chapters, we described the macroscopic properties of the superfluid phase by introducing the quantum fluctuations of a particular classical scalar field configuration. Nevertheless, this is a mere approximation since the dynamics of a quantum system is governed by the Hamiltonian evolution of its associated quantum state. The specific approximation we studied, in which the classical solution is the order parameter of the expansion defines the *semiclassical approximation* [114, 115].

Although the semiclassical approximation can be highly accurate in describing specific physical scenarios, such as the dynamics of highly occupied systems, an open question remains regarding the potential importance of subleading cumulative quantum effects in fully characterizing the behaviour of certain setups. For example, a series of papers [108, 109, 116–120] has shown that these quantum effects play a significant role in altering the late-time dynamics of various cosmological relevant systems, such as de Sitter spacetimes[1], Black Holes and Cosmological condensates. See [123, 124] for implications on the onset of Cosmic Inflation.

In these papers, the analysis of cumulative quantum effects is performed by invoking the corpuscular resolution of highly occupied systems. By parametrizing the initial state of the system in terms of a *coherent state* of constituent particles, semiclassical and sub-leading quantum properties are then studied by computing the transition amplitudes of processes involving constituents, such as scatterings or decays. The dynamics is organized in terms of a N^{-1} expansion, where N sets the number of asymptotic constituents involved in the process at hand, with the property that only classical contributions survive in the limit $N \to \infty$.

The time scale after which cumulative quantum effects (so the N^{-1} corrections to the dynamics) may invalidate the semiclassical expansion sets the *quantum break time* $t_{\text{q.b.}}$ of the system.

[1] See also [121, 122] for a different approach to de Sitter instabilities at the quantum level.

Different behaviours have been found by studying the emergence of this time scale in different setups. In systems exhibiting a classical (or Lyapunov) instability, the quantum break time reads

$$t_{\text{q.b.}} \sim \gamma^{-1} \log N, \tag{4.1}$$

where γ is the Lyapunov exponent of the semiclassical instability. The concept of the quantum break-time was initially introduced in the context of this category of systems in the paper [125], in which authors focused on the case of non-relativistic and overcritical ($\alpha N \gg 1$, with α quantum coupling) superfluids. The generalization to the relativistic case was performed in [126, 127].

On the other hand, if the system does not exhibit any Lyapunov instability, the maximum quantum break time is set to

$$t_{\text{q.b.}} \sim \alpha^{-1} t_{\text{cl}}, \tag{4.2}$$

where t_{cl} is the time scale after which the classical equation of motion becomes non-perturbative in *classical* non-linearities. This is the case which is relevant for de Sitter spacetimes and Black Holes, derived for the first time in [119]. Notice that there can be drastic differences between systems exhibiting Lyapunov instabilities and ones that do not. As shown in [128], the quantum break time for subcritical superfluids scales as $\sqrt{N}$, in contrast with the logarithmic scaling (4.1) of the overcritical analogues[2].

An interesting implication of this is that quantum effects could transform a *stationary* classical solution into an unstable quantum configuration. As we stressed, there are no classical solutions in quantum field theories. This is an approximate concept since solutions of the Euler-Lagrange equation are not (in general) solutions of the equivalent Heisenberg equation for the one-point function of the field operator, in an interacting quantum field theory. This mismatch defines the *quantum back-reaction of modes on the classical background*. Neglecting the back-reaction is not always a good approximation and its validity should be checked on a case-by-case basis.

For example, if the theory at hand allows for number-changing processes, such as the theory of a real scalar field with self-interactions, then a highly occupied configuration of zero momentum constituents could be depleted by the annihilation of constituent bosons. These processes may generate a mismatch between the classical solution and the one-point function of the field operator, leading to a departure of the quantum order parameter[3] from its classical counterpart and eventually invalidating the semiclassical description. It is important to highlight that the assessment of the backreaction within the semi-classical framework can be approached using various methods. For a comprehensive overview, we refer the reader to [132, 133]. However, in this chapter, we discuss the advantages of studying the time evolution of the state itself.

[2]It is claimed that the *memory burden* [129] is another phenomenon that could strongly influence the quantum breaking in systems with enhanced memory capacity. These are systems exhibiting an abundance of microstates which are energetically cheap to populate. Certain critical systems belong to this category. If they start to decay, the information stored backreacts on the system itself, leading to quantum breaking. This effect is important for black holes, for example, as it would change their evolution at latest after the half-evaporation time [130].

[3]In this thesis, we investigate systems in which the one-point function of the field operator serves as the expansion parameter of the dynamics. However, in general, any higher-order correlation function can serve this purpose. For instance, in the case of the BCS theory [131], the correlation function $\langle \psi^\dagger \psi \rangle$ provides the expansion parameter, while for the quark condensate this role is played by the charge operator $\langle \bar{\psi} \psi \rangle$.

Although the corpuscular picture is a strong tool for understanding the dynamics of the aforementioned systems, it provides approximate results, since certain properties of the dynamics cannot be easily computed. Therefore, in this chapter, we investigate the quantum dynamics of highly occupied systems by studying the evolution of correlation functions in the interaction picture formalism. By using the standard Schwinger-Keldish approach, we connect the results obtained in the S-matrix formalism with the more standard correlation function analysis. One of the main advantages of this formulation is that it allows to compute the evolution of a quantum state starting from finite time. This analysis has two purposes: we are confirming the corpuscular analysis by using different techniques and we investigate the consistency of coherent states, once they are embedded in the full quantum field theory framework.

The model we study is the theory of a real scalar field with quartic interactions, with the Hamiltonian density determined by

$$\hat{H} = \frac{1}{2}\hat{\pi}^2(x) + \frac{1}{2}\partial_i\hat{\phi}(x)\partial^i\hat{\phi}(x) + \frac{1}{2}m^2\hat{\phi}^2(x) + \frac{\lambda}{4!}\hat{\phi}^4. \tag{4.3}$$

Finally, let us stress that the content of this chapter is drawn from the series of papers [110, 134] in which the author of this thesis played a significant role as one of the primary contributors.

4.1 Introduction to Coherent states

Coherent states were originally introduced by Erwin Schrödinger in 1926 [135]. They are derived as the Gaussian wave packets of the harmonic oscillator, obtained by solving the Schrödinger equation for this particular system. By centering the Gaussian distribution around two external parameters, it becomes possible to construct a wave packet that minimizes the uncertainty principle while maintaining non-zero expectation values for the position and momentum operators in the classical limit. Although it was known that coherent states could describe systems of minimum uncertainty, it was only forty years later that Roy J. Glauber could show their importance in understanding the wave-particle duality of photons in quantum optics. He demonstrated that coherent states provide the theoretical framework to comprehend the disappearance of this duality as the classical limit of a coherent electromagnetic wave is approached [136].

In this section, we provide the theoretical groundwork of Coherent states in interacting quantum field theories [137, 138][4]. The simplest coherent states that can be constructed starting from a real scalar field operator $\hat{\phi}(x)$ and its conjugate momentum $\hat{\pi}(x)$ are known as *non squeezed coherent states*. These are states of minimum uncertainty, in which the latter is equally distributed in the canonical variable and its conjugate momentum. They are also typically characterized by a set of c-number functions $\phi_{\rm cl}(x)$, $\pi_{\rm cl}(x)$ that determine the initial conditions of the system. Their general form can be expressed as follows

$$|C\rangle = e^{-\frac{i}{\hbar}\int \mathrm{d}^3x\left(\phi_{\rm cl}(x)\hat{\pi}(x) - \pi_{\rm cl}(x)\hat{\phi}(x)\right)}|\Omega\rangle, \tag{4.4}$$

[4]See also [110, 139] for a general overview on the dynamics on quantum field theories and [140] for their evolution in quantum mechanics.

where $|\Omega\rangle$ is the vacuum of the interacting theory, with the field operator and its conjugate momentum satisfying canonical commutation relations. It is straightforward to show that the initial conditions for the expectation value of the field operator and of the conjugate momentum over the state $|C\rangle$ are uniquely determined by the c-number functions as

$$\langle C|\hat{\phi}|C\rangle(t=0) = \phi_{\rm cl}(x)\,, \tag{4.5}$$
$$\langle C|\hat{\pi}|C\rangle(t=0) = \pi_{\rm cl}(x)\,. \tag{4.6}$$

If $\phi_{\rm cl}(x)$ and $\pi_{\rm cl}(x)$ stay finite as $\hbar$ approaches zero, the properties of the state in this limit can be completely captured by the classical evolution of the c-number functions. Consequently, in the classical limit, the state defined by equation (4.4) exhibits the same dynamics as the classical configuration characterized by the same set of $\phi_{\rm cl}(x)$ and $\pi_{\rm cl}(x)$.

The behaviour of correlation functions evaluated over $|C\rangle$ is one of the main properties of non-squeezed coherent states. In particular, any product of operators that is bracketed over this state is shifted by the c-number functions as follows

$$\langle C|\mathcal{O}(\hat{\phi},\hat{\pi})|C\rangle = \langle\Omega|\mathcal{O}(\phi_{cl}(x)+\hat{\phi},\pi_{cl}(x)+\hat{\pi})|\Omega\rangle. \tag{4.7}$$

This relation follows from the application of the Baker–Campbell–Hausdorff formula, canonical commutation relations and the linear nature in $\hat{\phi}$ and $\hat{\pi}$ of the exponent that enters in (4.4). See Appendix A for more details. The overall exponential factor of (4.4) is usually known as the *shift operator* since it induces a shift of the field operator it acts on according to (4.7).

This property of the shift operator entails the initial conditions that the state itself imprints on any correlation function. For example, we can check how non-squeezed coherent states determine the initial conditions for the two-point correlation function. At initial time, the expectation value of the quadratic field correlator on the state $|C\rangle$ reads

$$\langle C|\hat{\phi}(x,0)\hat{\phi}(y,0)|C\rangle = \phi_{\rm cl}(x)\phi_{\rm cl}(y) + \langle\Omega|\hat{\phi}(x,0)\hat{\phi}(y,0)|\Omega\rangle\,, \tag{4.8}$$
$$\langle C|\hat{\pi}(x,0)\hat{\pi}(y,0)|C\rangle = \pi_{\rm cl}(x)\pi_{\rm cl}(y) + \langle\Omega|\hat{\pi}(x,0)\hat{\pi}(y,0)|\Omega\rangle\,. \tag{4.9}$$

It is important to note that we have not invoked any specific properties of the theory, except for canonical commutation relations. Nevertheless, the expressions for initial conditions (4.5) and (4.9) are exact and merely rely on the fact that the one-point expectation value vanishes on the vacuum.

4.2 Depletion of the scalar condensate: S-matrix analysis

The theory of a real scalar field with quartic interactions is a good example of a theory where quantum effects can drastically change the late-time dynamics of a highly occupied system. In the classical theory, stationary solutions with finite amplitudes can be found by solving the classical equations of motion. However, when quantum effects are taken into account, this property is spoiled. The underlying reason is that the self-interacting potential of the theory (4.3) mediates number-changing processes, which depletes the condensate of zero-momentum particles. Notice

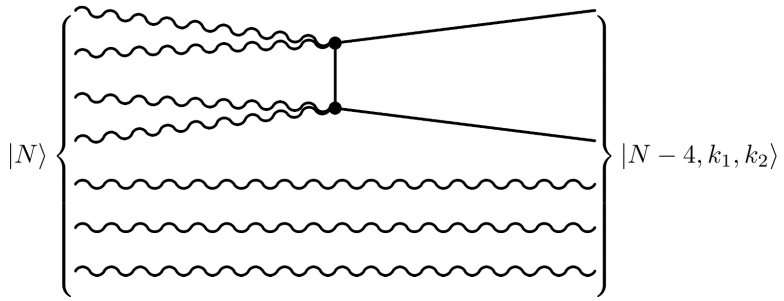

Figure 4.1: Depletion channel in which four zero momentum constituents of a condensate of real scalar bosons annihilate into two relativistic bosons. This is the leading channel and the net result is a depletion of the condensed phase and the production of radiation.

that this class of processes would not take place for complex scalar bosons, since the underlying $U(1)$ global symmetry of the theory would forbid number-changing processes.

A quantitative estimate of these effects can be obtained from S-matrix considerations. This analysis was performed in the context of the axion condensate in [108] (also see [141]). We sum up here the main results of the aforementioned papers. Let us introduce a state of N zero-momentum bosons

$$|N\rangle = \left(a_0^\dagger\right)^N |\Omega\rangle, \tag{4.10}$$

which describes a system in which all particles are in a zero momentum configuration. Here, we are ignoring the off-shell nature of these particles due to interactions. This is a good approximation only for time scales shorter than $t_{\rm cl}$, which correspond to the time scale after which classical non-linearities become significant. Within the theory (4.3), several processes may drain the condensate. Due to phase space considerations and multiplicity counting, the main process that contributes to the depletion of the condensate is the annihilation of four quantum constituents into two excited bosons

$$|N\rangle \to |N-4\rangle \otimes |k_1 k_2\rangle, \tag{4.11}$$

with the final bosons having a relativistic momentum $\vec{k}_{1,2} = \pm m$. This is expected to be the leading process as long as the combination of parameters $\lambda\hbar N$ is smaller than one. In the next section, we show that this corresponds to a system in which it is possible to perform a loop expansion. The effect of the multiplicity counting can be understood in terms of Bose-Einstein statistics. Due to the symmetry of the wavefunction, at zero temperature, a significant number of bosons are inclined to condense into the same energy level. Conversely, processes that remove particles from the condensed phase become increasingly less likely as more particles are removed and pushed into excited states. This explains qualitatively why, among the class of processes $|N\rangle \to |N-2m\rangle \otimes |k_i...k_m\rangle$, the channel with $m = 2$ is the dominant one.

Having said that, the interaction rate describing the conversion of four quantum constituents

into two relativistic particles may be estimated as

$$\frac{\Gamma_{4\to 2}}{V} \sim \left(\frac{\lambda n}{m^3}\right)^4 m^4 \tag{4.12}$$

Within the parenthesis, we identify the collective coupling, which can be interpreted as the coupling times the number of particles in a volume of size m^{-3}. The rate (4.12) sets the time scale in which quantum effects start changing the late-time dynamics of the system when compared to the classical approximation. The time scale in which an order one fraction of the condensed phase is depleted reads

$$\frac{\Gamma\, t_{\rm q.b.}}{N} = 1 \quad \longrightarrow \quad t^{-1}_{\rm q.b.} = \lambda \left(\frac{\lambda n}{m^3}\right)^3 m \tag{4.13}$$

Here, $t_{\rm q.b}$ is the quantum break-time. In terms of the parameters of the coherent state, the quantum break time (4.13) can be recast into

$$t^{-1}_{\rm q.b} \sim \frac{\lambda^4 \phi^6_{\rm cl}}{m^5}, \tag{4.14}$$

with the number of particles per unit volume equal to $n \simeq 2m\phi^2_{\rm cl}$.

In other words, considerations about the nature of the constituents of the condensate predict that the number of quantum constituents should decrease with time. In the next section, we demonstrate that this estimate of the time scale of the depletion is consistent with a rigorous analysis of the dynamics of the coherent state corresponding to a homogeneous condensate.

4.3 Depletion of the scalar condensate: Coherent state analysis

In this section, we derive the depletion of the condensed phase of a collection of zero-momentum real scalar bosons by analysing the evolution of the coherent state corresponding to a homogeneous field configuration

$$|C_h\rangle = \exp\left\{-i \int {\rm d}^3x\, \phi_0 \hat{\pi}(x)\right\} |\Omega\rangle. \tag{4.15}$$

Here, ϕ_0 is a constant number, connected to the one-point function of the field operator at the initial time, according to (4.5). The initial time expectation value of the conjugate momentum is set to zero.

The first step is to choose the observable built from the coherent state $|C_h\rangle$ which encodes the depletion of the condensate due to number changing processes. The most natural candidate is the one-point function of the field operator. This can be inferred by noting that the number of particles in the system can be estimated by considering the expectation value of the Hamiltonian per unit of mass. Since the expectation value of the field operator at the initial time is the only parameter we introduced, it is not surprising to find that

$$\langle C_h|\hat{N}|C_h\rangle(t=0) \sim m\,\phi_0^2 + m\langle\Omega|\hat{\phi}^2(x,t)|\Omega\rangle \tag{4.16}$$

In the same spirit as a superfluid, the expectation value of the field operator is associated with the number of particles stored in the condensed phase. Any depletion of the condensed phase is expected to result in a depletion of the amplitude of the one-point function $\langle C_h|\hat{\phi}|C_h\rangle(t)$. At the same time, the resulting creation of relativistic bosons is going to populate excited states, leading to a deviation of the expectation value $\langle C_h|\hat{\phi}^2|C_h\rangle - \langle C_h|\hat{\phi}|C_h\rangle^2$ from its vacuum counterpart. In other words, $4 \to 2$ processes are expected to induce the decoherence of the state and, at the same time, diminish the amplitude of the correlation function $\langle C_h|\hat{\phi}|C_h\rangle$.

4.3.1 Interaction picture formalism

The one-point function of the field operator can be computed in several ways. The first approach is to directly evaluate the correlation function $\langle C_h|\hat{\phi}|C_h\rangle$ in the interaction picture formalism. This can be done following the standard textbook derivation [142] and the evaluation of this correlation function with this method is reported in Appendix A of the paper [110].

We sum up the procedure in this subsection. The starting point is to split the full Hamiltonian into its quadratic part and the interacting Hamiltonian. In the case of $\lambda\hat{\phi}^4(x)$, it implies the decomposition

$$\hat{H} = \hat{H}_0 + \hat{H}_{\rm int}, \qquad \text{with} \qquad \hat{H}_{\rm int} = \int d^3x \frac{\lambda}{4!}\hat{\phi}^4. \tag{4.17}$$

We define the *Interaction Picture field*, as the field that evolves according to the quadratic Hamiltonian H_0

$$\hat{\phi}_I(x,t) = e^{iH_0(t-t_0)}\hat{\phi}(t_0,x)e^{-iH_0(t-t_0)}. \tag{4.18}$$

In terms of a ladder expansion, we decompose the interaction picture field in terms of free waves as

$$\hat{\phi}_I(x,t) = \int \frac{d^3p}{(2\pi)^3}\frac{1}{\sqrt{2\omega_p}}\left(a_{\vec{p}}\, e^{-i\omega_p(t-t_0)+ip\cdot x} + a^\dagger_{\vec{p}}\, e^{i\omega_p(t-t_0)-i\vec{p}\cdot x}\right), \tag{4.19}$$

where t_0 (which in our case is going to be set to zero) is the fiducial time at which the ladder expansion is defined and $\omega_p = \sqrt{p^2+m^2}$.

If λ is small, the time evolution is in first approximation captured by H_0 and correlation functions can be expanded in terms of the interaction picture field operator. Correlation functions are evaluated in series of the interaction Hamiltonian by expanding

$$\langle C|\mathcal{O}(\hat{\phi},\hat{\pi})|C\rangle(t) = \langle 0|e^{i\phi_0\int \mathrm{d}^3x'\hat{\pi}_I(0,x')}U_I(0,t)\mathcal{O}(\hat{\phi},\hat{\pi})U_I(t,0)e^{-i\phi_0\int \mathrm{d}^3x''\hat{\pi}_I(0,x'')}|0\rangle, \tag{4.20}$$

with $\mathcal{O}$ an arbitrary combination of field operators and conjugate momenta[5]. We also define the free vacuum $|0\rangle$ as the vacuum annihilated by the interaction picture ladder operator $a_{\vec{p}}$. The operator

$$U_I(t,t_0) = \int_{t_0}^{t} \mathrm{d}t' H_I(x,t') \tag{4.21}$$

[5]Here, we considered only evolution operators $U(t_0,t)$ that we need to study the problem at hand up to one-loop corrections. The full correlation function written in terms of interaction picture operators and free vacuum includes an overall normalization factor $\langle U(-T,T)\rangle^{-1}$ and two additional evolution operators $U_I(T,0)$ and $U_I(-T,0)$, which have to be inserted respectively between the left (right) free vacuum and the left (right) shift operator, with $T \to \infty_-$.

is the evolution operator in the interaction picture, which controls the order of the expansion. Because the effect we expect is order λ^4, the relation (4.20) has to be evaluated up to the fourth order in the interaction Hamiltonian.

The main advantage of this method is that it allows for a straightforward evaluation of a correlation function once the state of the system is specified. However, there are also significant drawbacks. One major downside is that, by applying the interaction picture formalism, the full self-interacting potential is treated as a perturbation. This implies that any correlation function built from $|C_h\rangle$ is plagued by spurious secular classical instabilities, that have to be resummed. We see this by noting that the classical equation of motion of the theory (4.3) admits a non-trivial solution in terms of Hypergeometric functions. However, the shift operator in the interaction picture would affect the perturbative expansion (4.20) by shifting field operators only by the *free solution* of the equation of motion. This is straightforward if we note that

$$e^{i\phi_0 \int \mathrm{d}^3x' \hat{\pi}_I(0,x')} \phi_I(x,t) e^{-i\phi_0 \int \mathrm{d}^3x'' \hat{\pi}_I(0,x'')} = \phi_0 \cos mt + \hat{\phi}_I(x,t). \tag{4.22}$$

Consequently, at every order in H_{int}, certain contributions appear, aimed at restoring non-linearities in the shift (4.22). As shown in [110], the effect of these corrections is to replace the free solution to the equation of motion which is introduced by the shift operator into the one-point function of the field operator itself. In other words, their resummation is achieved if we *impose by hand* that the coherent state $|C_h\rangle$ shifts any field operator $\hat{\phi}_I$ by $\langle C_h|\hat{\phi}|C_h\rangle$, and then we drop the spurious contributions[6].

4.3.2 Background field method formalism

There is an equivalent derivation of the one-point function of the field operator that is more convenient to overcome these downsides. This is the *background field method* revisited for coherent states (see e.g. [115]). The equivalence of the two methods is shown in [110]. To build the formalism, we start by considering the Heisenberg field equation for the field operator $\hat{\phi}(x,t)$

$$\Box\hat{\phi} + m^2\hat{\phi} + \frac{\lambda}{3!}\hat{\phi}^3 = 0, \tag{4.23}$$

As we said, the effect of the non-squeezed coherent state is to shift any power of the field operator by the one-point function of the field operator itself. Because of this, we can implement this shift by hand if we perform the following field redefinition

$$\hat{\phi}(x,t) = \Phi(t) + \hat{\psi}(x,t) \qquad \text{with} \qquad \langle C_h|\hat{\psi}(x,t)|C_h\rangle = 0. \tag{4.24}$$

Here, $\Phi(t) = \langle C_h|\hat{\phi}|C_h\rangle$ is the one-point function of the field operator by definition and it implies that $\hat{\psi}(x,t)$ has no expectation value when evaluated over $|C_h\rangle$. We also want to stress that the decomposition of the field operator (4.24) is an exact statement.

[6] This may appear tautological, since the one-point function of the field operator over $|C_h\rangle$ seems to evolve according to a Hamiltonian that depends on the one-point function itself. However, the n-loop contribution to the 1-point function is determined by a Hamiltonian that depends only on the previous $n-1$ contributions. This property allows for a perturbative time evolution, making the expansion consistent as long as a loop-expansion is allowed.

By plugging this decomposition in the equation of motion for the field operator, it is possible to derive a set of two differential equations, one for the one-point function of the field operator $\Phi(t)$ and one for the fluctuation field $\hat{\psi}(x,t)$. The first equation is obtained by considering the expectation value of the full equation over $|C_h\rangle$ and using the property that the expectation value of the fluctuation field vanishes over the coherent state. We get

$$\ddot{\Phi}(t) + m^2\Phi(t) + \frac{\lambda}{2}\langle C_h|\hat{\psi}^2(x,t)|C_h\rangle\Phi_{cl}(t) + \mathcal{O}(\hbar^2) = 0 \tag{4.25}$$

where we dropped terms that would contribute starting from higher $\hbar$ orders. The second equation, which determines the dynamics of $\hat{\psi}(x,t)$, is obtained by subtracting the equation (4.25) to the full shifted equation. By multiplying the new equation on the left by an additional factor of $\hat{\psi}(y,t)$ and by considering the expectation value of $|C_h\rangle$, we obtain the following equation of motion for the two-point correlation function of the fluctuation field

$$\langle C_h|\hat{\psi}\,(y,t)\left(\Box - m^2 - \frac{\lambda}{2}\Phi^2(t)\right)\hat{\psi}\,(x,t)\,|C_h\rangle + ... = 0 \tag{4.26}$$

where we dropped contributions which would contribute at higher orders in the loop expansion. The system of equations (4.25)-(4.26) provides the full one-loop dynamics of the system. It is important to note that, since we are only concerned with the tree-level corrections to $U_P(t)$, the $\Phi(t)$ term appearing in (4.26) can be approximated by the classical solution of the equation of motion.

One may ask what is the role of the state $|C_h\rangle$ in this decomposition. At this stage, we only assumed that the loop expansion could be performed, and any state would have produced the same outcome. However, the non-squeezed coherent state $|C_h\rangle$ fixes the initial conditions that we have to impose to solve the system of equations (4.25)-(4.26). In this case, it implies that the initial time one-point function has to be determined by ϕ_0, while the two-point function of the field operator $\hat{\psi}$ by its vacuum value, as indicated by (4.8). It is also important to note that this is different from what would happen if we were to use the crude interaction picture formalism to evaluate the evolution of these correlation functions since the master formula (4.20) automatically accounts for these properties.

It is possible to evaluate the aforementioned system of equations at one-loop. This is done by solving the equation for the quadratic correlation function by writing the formal solution

$$\langle C_h|\psi(x,t)\psi(y,t)|C_h\rangle = \int \frac{d^3p}{(2\pi)^3 2\omega_p}|U_p(t)|^2 e^{i\vec{p}\cdot(\vec{x}-\vec{y})}. \tag{4.27}$$

Here, the dispersion relation that enters the ladder expansion is the same one of free fields in the vacuum. This property is fixed by $|\Omega\rangle$ on which the coherent state is built. We are going to show in the next section that this property has strong implications on the perturbativity of non-squeezed coherent states.

If we plug this ansatz back in the equation of motion (4.26), we derive the following differential equation for $U_p(t)$

$$\left(\partial_t^2 + \omega_p^2 + \frac{\lambda}{2}\Phi_{\rm cl}(t)^2\right)U_p(t) = 0. \tag{4.28}$$

The equation (4.27) has no exact analytic solution, but it can be solved perturbatively in λ or it can be evaluated numerically. Finally, we plug in the solution to the equation of motion for the quadratic correlation function back in (4.25) and we solve for the one-point function. This approach was implemented in the paper [115] to study the 1-loop dynamics of a condensate of real scalar bosons, although different initial conditions — and therefore a different initial state — were considered.

Still, the procedure depicted above does not suit completely what we want to achieve. To establish a connection between the S-matrix approach and the evolution of the Coherent state, we have to be perturbative in terms of *quantum non-linearities*. By solving the system of equations in the aforementioned way, we are considering the depletion of the 1-point function due to the sum of all the $|N\rangle \to |N-2m\rangle \otimes |k_i...k_m\rangle$ decay channels. This class of processes contributes to the depletion with the same power of $\hbar$ and therefore the full resummed 1-loop dynamics would account for their combined effect. However, what we want to do is isolate the $m = 2$ channel and show that it dominates the dynamics, according to the S-matrix analysis.

To remain perturbative in λ, while summing over classical non-linearities, we use a hybrid approach in between the background field method and the crude interaction picture formalism. By focusing on the equation (4.25), we rewrite the correlation function quadratic in the fluctuation field in terms of the original ϕ field as

$$\langle C_h|\hat{\psi}^2(x,t)|C_h\rangle = \langle C_h|\hat{\phi}^2(x,t)|C_h\rangle - \langle C_h|\hat{\phi}(x,t)|C_h\rangle^2. \tag{4.29}$$

Then, we evaluate all the correlation functions entering in the right-hand side up to order λ^3 using the interaction picture formalism (4.20). In this way, the equation (4.25) can be brought to the following form

$$\begin{aligned}\left(\partial_t^2 + m^2\right)\Phi(t) + \frac{\lambda}{3!}\Phi^3(t) = &-\frac{\lambda}{2}\Phi(t)\langle\hat{\phi}^2\rangle + \frac{\lambda^2}{2}\Phi(t)\int_0^t \mathrm{d}t_1\,\Phi^2(t_1)S_1(t,t_1)\\ &-\frac{\lambda^3}{2}\Phi(t)\int_0^t \mathrm{d}t_1\int_0^{t_1}\mathrm{d}t_2\,\Phi^2(t_1)\Phi^2(t_2)S_2(t,t_1,t_2)\\ &+\frac{\lambda^4}{8}\Phi(t)\int_0^t \mathrm{d}t_1\int_0^{t_1}\mathrm{d}t_2\int_0^{t_2}\mathrm{d}t_3\,\Phi^2(t_1)\Phi^2(t_2)\Phi^2(t_3)S_3(t,t_1,t_2,t_3) + ...\end{aligned} \tag{4.30}$$

Here, $\langle\hat{\phi}^2\rangle$ is the expectation value taken over the free vacuum of the theory $|0\rangle$, while S_i functions read

$$S_1(t,t_1) = \int \frac{\mathrm{d}^3p}{(2\pi)^3(2\omega_\mathrm{p})^2}\sin\left(2\omega_\mathrm{p}(t-t_1)\right) \tag{4.31}$$

$$S_2(t,t_1,t_2) = \int \frac{\mathrm{d}^3p}{(2\pi)^3(2\omega_\mathrm{p})^3}\Big(\cos\left(2\omega_\mathrm{p}(t_1-t_2)\right) - \cos\left(2\omega_\mathrm{p}(t-t_1)\right)\Big) \tag{4.32}$$

$$\begin{aligned}S_3(t,t_1,t_2,t_3) = \int \frac{\mathrm{d}^3p}{(2\pi)^3(2\omega_\mathrm{p})^4}\Big(&\sin\left(2\omega_\mathrm{p}(t-t_3)\right) - \sin\left(2\omega_\mathrm{p}(t_1-t_3)\right)\\ &+ \left(\sin\left(2\omega_\mathrm{p}(t-t_1)\right)\cos\left(2\omega_\mathrm{p}(t_2-t_3)\right)\right)\Big).\end{aligned} \tag{4.33}$$

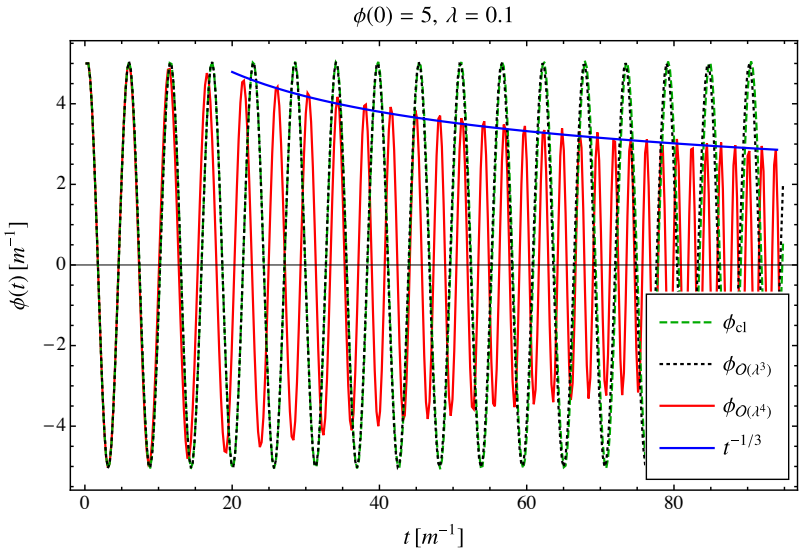

Figure 4.2: The numerical solution of Eq. (4.30), with different $\mathcal{O}(\lambda)$ terms. The green line corresponds to the classical solution of the equation of motion while the black line to the one-point correlation function up to λ^3 and $\hbar$ corrections. No qualitative deviations are seen between those two lines. The situation is drastically different if λ^4 terms are included (red line). At this order, the $4 \to 2$ annihilation channel of constituent particles is included, leading to a depletion of the amplitude of the one-point function of the field operator. The blue line represents the scaling $t^{-1/3}$ which is obtained by performing a full one loop-analysis. As we may see, it matches the scaling of depletion obtained from the λ^4 term, confirming that $4 \to 2$ is the main depletion channel.

Also, free solutions are replaced by the 1-point function itself and reducible diagrams are dropped, according to the resummation scheme we depicted in the first part of this section. The functions S_i can be interpreted as the quantum corrections to the equation of motion for the one-point function of the field operator, sourced by specific powers of λ.

The evaluation of these correlation functions is accompanied by the appearance of divergent contributions, which can be removed by regulating and renormalizing the theory. We postpone this analysis to the next section, but we see that we may remove divergences if we rewrite the equation (4.30) in terms of the physical mass and coupling, according to the prescriptions

$$m_{\rm ph}^2 = m^2 + \frac{\lambda}{2}\langle\phi^2\rangle, \qquad \lambda_{\rm ph} = \lambda - 3\lambda^2 \int \frac{d^3{\rm p}}{(2\pi)^3}. \tag{4.34}$$

Coupling renormalization is obtained by isolating the divergent term in the S_1 contribution and redefining the coupling of the cubic term $\lambda\Phi^3$. Notice that these are the same prescriptions that we would introduce to renormalize scattering computations.

Once divergences have been removed from Eq. (4.30), it is possible to solve numerically the integro-differential equation to find the one-point function $\Phi(t)$ as a function of time. Details of the numerical evaluation are given in [110]. The final result is reported in Fig (4.2). If

only λ^2 and λ^3 corrections are included, the evolution of $\Phi(t)$ is qualitatively similar to the behaviour of the classical solution to the equation of motion. These are represented in Fig. (4.2) by the dashed green (classical solution) and dotted black line (one-point up to λ^3). We see that quantum corrections induce a small dephasing of the classical solution, while the amplitude remains unaffected.

The situation is different at order λ^4, which is precisely the order at which $4 \to 2$ processes are expected to contribute to the depletion of the condensate, as shown by the estimate of the quantum break time (4.14) obtained in the S-matrix analysis. This identification is also confirmed by noting that the λ^4 term contributes to the variation of the amplitude of the one-point function as

$$t_{\rm depl}^{-1} \sim \frac{\dot{\Phi}}{\Phi} \sim \frac{\lambda^4 \phi_0^6}{m^5}, \tag{4.35}$$

which matches parametrically the quantum break time derived (4.14).

The last step is to show that the λ^4 term of (4.30) determines the leading behaviour of Φ(t). To see this, it is sufficient to note from Fig. 4.2 that the amplitude of the one-point function of the field operator depletes according to the scaling $t^{-1/3}$. This is the well-known scaling that has been found in the full 1-loop analysis [114], which resums the effects of all the $\hbar$-order depletion channels, confirming that $4 \to 2$ scatterings are the leading depletion processes.

4.4 Initial time singularity and Squeezed coherent states

In this section, we address the issue of the *initial time singularity* [115, 143, 144] associated with Coherent states. To introduce the problem, it is convenient to highlight what are the pathologies that appear in the evolution of the one-point function of the field operator, evaluated over the non-squeezed coherent state (4.15). To do this, let us go back to the equation of motion for the field operators (4.30) and let us focus on λ^2 terms. We rewrite the aforementioned equation as

$$\left(\partial_t^2 + m_{\rm ph}^2\right)\Phi(t) + \frac{\lambda_{\rm ph}}{3!}\Phi^3(t) = -\frac{\lambda^2\phi_0^2}{2}\Phi(t)\int_0^t {\rm d}t_1 \Phi^2(t_1)\int \frac{{\rm d}^3p}{(2\pi)^3(2E_{\rm p})^3}\cos\left(2E_{\rm p}(t-t_1)\right) + ... \tag{4.36}$$

The term on the right-hand side is obtained by regulating the S_1 integral. In particular, to extract the divergent contribution, we integrate by part the overall time integral of S_1. The boundary term evaluated over $t_1 = t$ can be combined with the cubic term of the left-hand side of equation (4.30) into $\lambda_{\rm ph}$. The leftover time integral is manifestly finite and can be ignored in this discussion. What we have to focus on is the right-hand side of equation (4.36), which corresponds to the boundary term evaluated on $t_1 = 0$. We see that this term is manifestly finite as long as $t \neq 0$, but it becomes divergent at the initial time. In other words, it appears that the equation of motion for the one-point function could present certain divergent terms at the initial time that could spoil the dynamics of the correlation function itself. Nevertheless, if we solve the equation of motion for $\Phi(t)$ and we focus on the term generated by this specific contribution, we obtain

$$\Phi(t) = ... + \frac{\lambda^2\phi_0^3}{64\pi^2}t^2\log(mt). \tag{4.37}$$

The one-point function of the field operator remains a finite quantity at the initial time, but its second-time derivative acquires a logarithmic divergence.

Why does this divergence appear? We notice that if we consider the non-renormalized equation of motion (4.30), all quantum non-linearities vanish at the initial time, including the S_1 source term. Therefore, performing the renormalization of the theory at the initial time would imply that there are no divergences that can be combined with the bare coupling to obtain the physical coupling. However, standard counterterms still have to be introduced to remove divergences that are radiatively generated at late time and, in doing that, these are moved in the initial time field acceleration.

One could question if having a field acceleration which is divergent at the initial time may represent a problem at all. However, there is a second and more severe problem which appears if initial time singularities are not addressed, namely the divergence of the energy which the field configuration is sourcing. Let us consider the expectation value of the full Hamiltonian over non-squeezed coherent states for the theory (4.3) (see [139])

$$\langle C|\hat{H}|C\rangle = \frac{1}{2}\int d^3x \left\{ \pi_{\rm cl}^2 + (\nabla\phi_{cl})^2 + \left(m^2 + \frac{\lambda}{2}\langle\Omega|\hat{\phi}^2(x)|\Omega\rangle \right)\phi_{\rm cl}^2 + \frac{\lambda}{12}\phi_{\rm cl}^4 \right\}. \tag{4.38}$$

Here, we considered the non-homogeneous coherent state (4.4) and we have adjusted the bare vacuum energy in a way that the expectation value (4.38) vanishes if we set $\phi_{\rm cl}$ and $\pi_{\rm cl}$ to zero.

The bare mass term m comes in pair with the divergent contribution $\langle\Omega|\hat{\phi}^2|\Omega\rangle$. At the leading order in $\hbar$, this corresponds to the same *bubble divergence* that we absorbed in the redefinition of the mass in (4.34). However, the analogous contribution to the coupling constant is absent in (4.38) implying that, in the same way as the initial field acceleration, the energy stored in the coherent state is sourced by the bare coupling constant, and not by its physical counterpart. However, the missing divergence is not localized at the initial time in the case of the energy, being the expectation value of the total Hamiltonian conserved.

The discrepancy between the divergences at the initial time provided by a state and the standard vacuum divergences is commonly referred to as an *Initial Time Singularity* [115, 145–148]. The name arises from the observation that, when we examine the evolution of the expectation value of the field operator, we discover that the missing S-matrix singularities are perturbatively generated at $t > 0$. However, these singularities are not initially present and, through the process of renormalization, they are effectively shifted at the initial time. In an equivalent way, but which emphasizes the severity of the problem, the initial time singularity can be understood from (4.30) and (4.38) as the inability to make both the total energy of the system and the one-point function of the field operator finite by introducing time-independent counterterms.

Here, we conclude our discussion about non-squeezed coherent states. Non-squeezed coherent states such as (4.4) can be considered physical members of the Hilbert space of the theory (4.3) only if we determine a procedure to remove the discrepancy between initial time and late divergences. Since we know that the bare coupling constant is infinite at any given order in perturbation theory, the only possibility for the coherent state in question would be if the bare coupling comes out finite after resuming all infinite contributions. A similar argument should apply to some of the divergent contributions to the mass which, as we are going to see in the last

part of this chapter, may generate initial time singularities starting from the 2-loop dynamics. Of course, this solution would go beyond the domain of perturbation theory and therefore we conclude that Coherent states as (4.4) cannot provide a finite perturbative description of a physical system.

4.4.1 Squeezed coherent states as the regulator of the one-loop dynamics

The natural follow-up question concerns finding the minimal modification to the coherent state (4.4) that would restore a perturbative behaviour and that can remove any eventual initial time singularity. The starting point is to remind the reader that mode functions at the initial time are defined in terms of the vacuum dispersion relation. This is due to the fact that the connected part of the initial time two-point function is equivalent to the vacuum one and entails that the function $U_p(t)$ defined (4.27) is equal to one at $t = 0$.

It was noticed in [115] in the context of a semiclassical computation that initial time-singularities vanish at one-loop if the mode functions of the fluctuation field $\hat{\psi}(x)$ at initial time are defined in terms of the *shifted mass* $m_{\rm exc}$[7], instead of vacuum mass m, with

$$m^2_{\rm exc} = m^2 + \frac{\lambda}{2}\phi_0^2. \tag{4.39}$$

This result seems to indicate that the root of the problem comes from the two-point correlation function (4.8) and the fact that its fluctuation part is independent of ϕ_0. In standard semiclassical computations, the shifted mass (4.39) precisely yields the background-dependent contribution to correlation functions that one would need at the initial time to restore the perturbativity. However, the non-squeezed coherent state (4.15) initializes the connected part of correlation functions as if they are in the interacting vacuum, as we see from (4.8) and (4.9). Therefore, no notion of background appears.

To overcome this issue, we have to fix the state of the system to provide the following initial conditions of the quadratic correlation functions

$$\langle C_S|\hat{\phi}(x,0)\hat{\phi}(y,0)|C_S\rangle = \phi_0^2 + \int \frac{d^3p}{(2\pi)^3}\frac{e^{i\vec{p}\cdot(\vec{x}-\vec{y})}}{2\sqrt{p^2+m^2+\frac{\lambda}{2}\phi_0^2}}\,, \tag{4.40}$$

$$\langle C_S|\hat{\pi}(x,0)\hat{\pi}(y,0)|C_S\rangle = \int \frac{d^3p}{(2\pi)^3}\,\frac{1}{2}e^{i\vec{p}\cdot(\vec{x}-\vec{y})}\sqrt{p^2+m^2+\frac{\lambda}{2}\phi_0^2}\,. \tag{4.41}$$

which, as we demonstrate, provides the correct initial time divergences.

This raises the question of what this implies in terms of the state of the system. It was noted in [115] that, to provide a notion of shifted mass at the initial time, we have to implement a Bogoliubov transformation on the fluctuation field $\psi(x,t)$. Because a Bogoliubov transformation can be equivalently parameterized by replacing the vacuum state of the theory with a squeezed

[7] We have to keep in mind that, differently from a U(1) invariant theory, there is no notion of shifted mass at all times, being $\Phi^2(t)$ a manifestly time-dependent quantity, and that (4.39) should be considered as an initial time statement.

vacuum [149], a good guess for restoring the perturbative aspects of the dynamics is to consider the following realization of a unitary *squeezed* coherent state

$$|C_S\rangle = \exp\left\{-\frac{i}{\hbar}\int \mathrm{d}^3x\,\phi_0\,\hat{\pi}(x)\right\}|S\rangle\,, \qquad \text{with} \quad |S\rangle = e^{-i\hat{S}}|\Omega\rangle \tag{4.42}$$

where $|S\rangle$ is the squeezed vacuum, with the one-point function of the field operator vanishing on this state. Squeezed coherent states can be understood as states which still saturate the uncertainty principle but with an unequal distribution of uncertainties. In other words, one of the uncertainties (either field or momentum) is reduced, while the other is increased, compared to the non-squeezed case.

We still focus our discussion on a homogeneous scalar field configuration. In terms of the field operator and conjugate momentum, a unitary squeezing can be represented by an exponential operator *quadratic in the field content* acting on the true vacuum of the theory. For the system at hand, we consider the following unitary realization

$$\hat{S} = \frac{1}{2}\int \mathrm{d}^3x\mathrm{d}^3y\,D(x-y)\left\{\hat{\phi}(x)\hat{\pi}(x)+\hat{\pi}(x)\hat{\phi}(y)\right\} \qquad D(x-y) = -\frac{1}{4}\int\frac{d^3p}{(2\pi)^3}\log\frac{E_p}{\omega_p}e^{ip\cdot(x-y)}, \tag{4.43}$$

where $D(x-y)$ is a c-number function connected to the initial conditions we want to imprint in correlation functions. Here, we fixed the squeezing operator to reproduce the initial time quadratic correlation functions (4.40)-(4.41), hence removing the initial time singularity at 1-loop order. We also defined $E_p = \sqrt{\omega_p^2 + \frac{\lambda}{2}\phi_0^2}$ as the dispersion relation written in terms of the shifted mass. As we are going to see later, there are different choices of the squeezing operator for which the initial time-singularity is removed. However, all $D(x-y)$ should have a specific high-k limit, in accordance with the one of (4.44).

In the case of squeezed coherent states, it is convenient to expand $\hat{S}$ in terms of creation and annihilation operators, obtaining the compact expression

$$\hat{S} = \frac{i}{4}\int\frac{\mathrm{d}^3p}{(2\pi)^3}\ln\frac{E_p}{\omega_p}\left(a_p a_{-p} - a_p^\dagger a_{-p}^\dagger\right). \tag{4.44}$$

When evaluating correlation functions over the squeezed state, the presence of the squeezed vacuum corresponds to implementing a Bogoliubov transformation on the creation and annihilation operators (see Appendix A). This transformation allows us to compute any correlation function over the state $|C_S\rangle$ by replacing the field content with a new one given by:

$$\hat{\phi}_s = e^{iS}\hat{\phi}e^{-iS} \qquad = \int\frac{d^3p}{(2\pi)^3\sqrt{2E_p}}\left(a_p e^{ip\cdot x} + a_p^\dagger e^{-ip\cdot x}\right), \tag{4.45}$$

$$\hat{\pi}_s = e^{iS}\hat{\pi}e^{-iS} = (-i)\int\frac{d^3p}{(2\pi)^3}\sqrt{\frac{E_p}{2}}\left(a_p e^{ip\cdot x} - a_p^\dagger e^{-ip\cdot x}\right), \tag{4.46}$$

These new operators are then evaluated on the true vacuum $|\Omega\rangle$. It is important to note that due to the presence of squeezing, the mode expansion involves the energy E_p instead of the usual frequency ω_p, which instead appears in the case of a non-squeezed coherent state.

In terms of the modified coherent state (4.42), the expressions of the field acceleration and of the total energy of the system acquire the following form

$$\partial_t^2 \langle C_S|\hat{\phi}|C_S\rangle(t=0) = -\phi_0 \left(m^2 + \frac{\lambda}{2}\langle S|\hat{\phi}^2|S\rangle\right) - \frac{\lambda}{3!}\phi_0^3\,, \tag{4.47}$$

$$\begin{aligned}\langle C_S|\hat{H}|C_S\rangle = \int \mathrm{d}^3x \Bigg[&\frac{1}{2}\left(m^2 + \frac{\lambda}{2}\langle S|\hat{\phi}^2|S\rangle\right)\phi_0^2 + \frac{\lambda}{4!}\phi_0^4 \\ &+ \frac{1}{2}\langle S|\left\{\hat{\pi}^2 + \left(\vec{\nabla}\hat{\phi}\right)^2 + m^2\hat{\phi}^2 + \frac{\lambda}{4!}\hat{\phi}^4\right\}|S\rangle \\ &-\frac{1}{2}\langle \Omega|\left\{\hat{\pi}^2 + \left(\vec{\nabla}\hat{\phi}\right)^2 + m^2\hat{\phi}^2 + \frac{\lambda}{4!}\hat{\phi}^4\right\}|\Omega\rangle\Bigg]\,;\end{aligned} \tag{4.48}$$

Again, the last two lines of (4.48) originate from the fact that the bare vacuum energy parameter has been adjusted so that $\langle\Omega|\hat{H}|\Omega\rangle = 0$ and they are the analogs of (4.25) and (4.38).

We can show now that both these observables are free from initial time singularities. To do this, we have to show that 1-loop prescriptions (4.34) can make both the energy and the field acceleration finite at the initial time. Let us begin by checking the latter. If we plug in the modified quadratic correlation function (4.40) in the 1-loop equation of motion, we find

$$\partial_t^2 \langle C_S|\hat{\phi}|C_S\rangle(t=0) = -\phi_0 \left(m^2 + \frac{\lambda}{2}\int \frac{d^3p}{(2\pi)^3}\frac{1}{2\sqrt{p^2 + m^2 + \frac{\lambda}{2}\phi_0^2}}\right) - \frac{\lambda}{3!}\phi_0^3\,, \tag{4.49}$$

where on the right-hand side we recognize the Coleman-Weinberg potential [150]. To see explicitly that the standard (S-matrix) 1-loop renormalization prescription for the quartic theory at hand renders (4.49) finite, let us expand the integrand in the Taylor series in the coupling constant. Up to finite contributions it reduces to

$$\frac{\lambda}{2}\int \frac{d^3p}{(2\pi)^3}\frac{1}{2\sqrt{p^2 + m^2 + \frac{\lambda}{2}\phi_0^2}} = \frac{\lambda}{2}\langle\hat{\phi}^2\rangle - \frac{\lambda^2}{2}\phi_0^2\int \frac{d^3p}{(2\pi)^3(2\omega_p)^3} + (\text{finite})\,. \tag{4.50}$$

The first term is the standard bubble diagram that contributes to mass renormalization, which we also encountered in the analysis of non-squeezed coherent states. However, in the case of the squeezing, we also have an additional logarithmic divergence, represented by the second term. It is straightforward to see that this combines with the cubic term of (4.49) into $\lambda_{\rm ph}$ according to (4.34) and we can repackage the equation of motion into

$$\partial_t^2 \langle C_S|\hat{\phi}|C_S\rangle(t=0) = -m_{\rm ph}^2\phi_0 - \frac{\lambda_{\rm ph}}{3!}\phi_0^3 + (\text{finite})\,. \tag{4.51}$$

Here (finite) stands for the finite corrections that originate from the effective potential a la Coleman-Weinberg.

The procedure outlined above also addresses the one-loop singularities of the Hamiltonian, when applied to equation (4.48). Naively, it may not appear to be so, since the same correlation function that generates the divergence in the equation of motion cannot produce the necessary divergence to renormalize the coupling of the $\lambda\phi_0^4$ term in the Hamiltonian. However, in

this scenario, we must also take into account the contributions from the second and third lines. Specifically, in the case of the squeezed vacuum, these lines generate an additional non-trivial correction. By considering all of these factors together, we find that the renormalization of the potential is achieved in the Hamiltonian by the same squeezing that removes divergences in the equation of motion for the one-point function.

After this discussion, it is evident that we are not bound to choose the squeezed vacuum $|S\rangle$ in a way that (4.40) and (4.41) are generated at the initial time. The only part required by consistency is the *divergent part* of the aforementioned correlation functions at space-coincidence. In other words, we have the freedom to incorporate any finite contribution, representing specific physical excitations of particles. Concretely, we could have chosen a dispersion relation E_p in a way that two-point correlation functions at the initial time would have read

$$\langle S|\hat{\phi}(x,0)\hat{\phi}(y,0)|S\rangle = \int \frac{d^3p}{(2\pi)^3}\frac{e^{i\vec{p}\cdot(\vec{x}-\vec{y})}}{2\sqrt{p^2+m^2}}\left(1-\frac{\lambda\phi_0^2}{4}\frac{1}{p^2+m^2}\right) + \int \frac{d^3p}{(2\pi)^3}e^{i\vec{p}\cdot(\vec{x}-\vec{y})}f(p)\,, \tag{4.52}$$

$$\langle S|\hat{\pi}(x,0)\hat{\pi}(y,0)|S\rangle = \int \frac{d^3p}{(2\pi)^3}\,\frac{1}{2}e^{i\vec{p}\cdot(\vec{x}-\vec{y})}\sqrt{p^2+m^2}\left(1+\frac{\lambda\phi_0^2}{4}\frac{1}{p^2+m^2}\right) + \int \frac{d^3p}{(2\pi)^3}e^{i\vec{p}\cdot(\vec{x}-\vec{y})}g(p)\,, \tag{4.53}$$

with $f(p)$ and $g(p)$ being arbitrary functions regular in $p \to 0$ limit and decaying faster than p^{-3} for large momenta. In their absence, the (*finite*)-terms are also absent from the above equations.

This is the current state of affairs regarding the expectation values of the field and the Hamiltonian in a scalar field theory with quartic interaction, at one loop. The bottom line of the discussion is that, to restore the perturbative aspects of the dynamics, a certain class of squeezing operators has to be considered, to restore certain divergences at the initial time.

4.5 Initial time singularity at two-loops and non-Gaussian states

In this section, we extend the analysis of initial time singularities to the two-loops order. To highlight the shortcomings of the previous section when considering higher loop corrections, it is convenient to study the time evolution of the one-point function of the field operator at order λ^2 and $\hbar^2$.

Let us consider, the equation of motion of the one-point function of the field operator, evaluated over the non-squeezed coherent state (4.15). This reads

$$Z\partial_t^2\langle C_h|\hat{\phi}|C_h\rangle = -Z\phi_0\left(m^2+\frac{\lambda}{2}\langle\Omega|\hat{\phi}^2|\Omega\rangle\right) - \frac{\lambda Z^2}{3!}\phi_0^3 - \frac{\lambda Z^2}{3!}\langle\Omega|\hat{\phi}^3|\Omega\rangle. \tag{4.54}$$

Since we study the dynamics at two loops, the field redefinition $\phi \to \sqrt{Z}\phi$ has been performed in order to provide the field renormalization. Also, we keep the overall Z-coefficients on the

left and right-hand sides, as it turns out to be convenient for renormalizing. By evaluating the correlation functions in interaction picture up to $\hbar^2\lambda^2$ corrections, the aforementioned equation reduces to [110]

$$Z\left(\partial_t^2+m^2\right)\Phi(t)+\frac{Z^2\lambda}{3!}\Phi^3(t)+\frac{\lambda}{2}\langle\phi^2\rangle\Phi(t)-\frac{\lambda^2}{2}\Phi(t)\int\frac{\mathrm{d}^3p}{(2\pi)^3(2\omega_p)^2}\int_0^t\mathrm{d}t_1\Phi^2(t_1)\sin 2\omega_p(t_1-t)+$$
$$-\frac{\lambda^2}{3}\int\frac{\mathrm{d}^3p\mathrm{d}^3q}{(2\pi)^6(8\omega_p\omega_q\omega_{p+q})}\int_0^t dt_1\Phi(t_1)\sin[\textstyle\sum\omega_i)(t-t_1)]+$$
$$-\frac{\lambda^2}{2}\langle\phi^2\rangle\Phi(t)\int\frac{\mathrm{d}^3p}{(2\pi)^3(2\omega_p)^3}...=0, \tag{4.55}$$

with $\sum\omega=\omega_p+\omega_q+\omega_{p+q}$. The second and third line are the additional $\hbar^2\lambda^2$ corrections to the equation of motion. We show now that their divergent part is removed if we impose the standard two-loop vacuum renormalization prescription for the mass and the field operator.

The interesting term is the nested momentum integral of the second line, which corresponds to the so-called *setting sun diagram* appearing in the vacuum analysis. To identify its divergent contributions, we integrate it by part three times. With that, we can extract two divergent contributions and the associated initial time singularities

$$\frac{\lambda^2}{3}\int\frac{\mathrm{d}^3p\mathrm{d}^3q}{(2\pi)^6(8\omega_p\omega_q\omega_{p+q})}\int_0^t dt_1\Phi(t_1)\sin[(\textstyle\sum\omega_i)(t-t_1)]\simeq$$
$$\frac{\lambda^2}{3}\int\frac{\mathrm{d}^3p\mathrm{d}^3q}{(2\pi)^6(8\omega_p\omega_q\omega_{p+q})}\frac{1}{\sum\omega_i}\left\{\Phi(t)-\Phi(0)\cos\left(\sum\omega_i t\right)-\frac{\ddot{\Phi}(t)}{(\sum\omega_i)^2}+\frac{\ddot{\Phi}(0)}{(\sum\omega_i)^2}\cos\left(\sum\omega_i t\right)\right\}, \tag{4.56}$$

where we neglected finite terms. It is straightforward to check that the first and third terms of (4.56) correspond to the standard mass and field divergences sourced by the setting sun diagram. This is confirmed by regulating the integrals in dimensional regularization and comparing the result of the integration to its vacuum analogous [151]. By using the following prescriptions

$$Z=1-\frac{\lambda^2}{3}\int\frac{\mathrm{d}^3p\mathrm{d}^3q}{(2\pi)^6(8\omega_p\omega_q\omega_{p+q})}\frac{1}{(\sum\omega_i)^3}, \tag{4.57}$$

$$m_{\mathrm{ph}}^2=Zm^2+\left(\frac{\lambda}{2}-\frac{\lambda}{2}\int\frac{d^3p}{(2\pi)^3(2\omega_p)^3}\right)\langle\hat{\phi^2}\rangle-\frac{\lambda^2}{3}\int\frac{d^3pd^3q}{(2\pi)^6(8\omega_p\omega_q\omega_{p+q})}\frac{1}{\sum\omega_i}, \tag{4.58}$$

the equation of motion can be made finite at a late time. Nevertheless, once the prescriptions are imposed, initial time singularities appear, corresponding to the second and fourth terms of (4.56). As we can see, these integrals are finite if $t>0$, but are divergent at initial time.

4.5.1 The failure of the squeezing operator at two-loops

A follow-up question regards the possibility of using the squeezing operator to fix the problem of initial time singularities also at the two-loops order.

We begin by examining the additional divergences that the squeezed coherent state (4.44) — the same squeezed state we introduced at one-loop — might introduce at the two-loops order. If we compute $\hbar^2$-corrections to the bubble diagram evaluated on this state, only the first two-loop divergence of (4.58) is generated. This is accomplished by including corrections that arise from projecting the interacting vacuum of the theory onto the non-interacting one, giving

$$\langle S|\hat{\phi}^2(x,0)|S\rangle = \int \frac{d^3p}{(2\pi)^3 2E_p}\left\{1-\frac{\lambda\langle\phi^2\rangle}{(2\omega_p)^2}\right\}. \tag{4.59}$$

However, notice that this term would have been generated also for non-squeezed coherent states, just with E_k replaced by ω_k. This is expected since the bubble diagram is the only divergence that is present also for non-squeezed coherent states. Notice that the cubic correlation function $\langle S|\hat{\phi}^3|S\rangle$ is still zero also at $\hbar^2$ order. However, the setting sun divergence is missing.

The second possibility could involve constructing a new squeezing operator designed to produce the missing divergence, represented by the setting sun contribution. Let us write explicitly the form of the quadratic correlation function that would make the mass in the equation of motion finite, by introducing the setting sun divergence. We would have

$$\langle S'|\hat{\phi}^2|S'\rangle = \int \frac{d^3p}{(2\pi)^3 2E_p}\left(1-\frac{\lambda^2}{3}\int \frac{d^3q}{(2\pi)^3 2E_q E_{q+p}}\frac{1}{\sum E_i}\right), \tag{4.60}$$

with $\sum E = E_p + E_q + E_{p+q}$. There are two main issues in the correlation function (4.60). First, we see that the new correction is independent of ϕ_0 and therefore would not vanish in the absence of the condensate. Second, the squeezing operator we have to consider would alter quadratic correlation functions in a way that would make the two-point function at point splitting divergent. We conclude that the quadratic correlation function and the squeezing operator cannot, by themselves, address the two-loop divergences generated by the setting sun contribution.

4.5.2 Non-gaussian states and the $\hat{T}$ operator

To solve the issue of the initial time singularity at two loops, it seems necessary to explore different states. In particular, because the quadratic correlation function cannot address the issue of the initial time singularity, it seems necessary to explore states for which the initial time cubic correlation function is not trivial.

Following this, we introduce the following class of non-gaussian states

$$|C_T\rangle = \exp\left\{-\frac{i}{\hbar}\int \mathrm{d}^3x\,\phi_0\,\hat{\pi}(x)\right\}|T\rangle \qquad \text{with} \quad |T\rangle = e^{-i\hat{S}}e^{-i\hat{T}}|\Omega\rangle, \tag{4.61}$$

where we introduced the $\hat{T}$ operator, cubic in the field operator and in the conjugate momentum[8]. In terms of creation and annihilation operators, we demand that $\hat{T}$ satisfies the following

[8]This class of operators in the field space can be written as $\hat{T} = \int d^3x\, d^3y\, d^3z\, M^{\alpha\beta\gamma}(x,y,z)\Phi_\alpha(x)\Phi_\beta(y)\Phi_\gamma(z)$, with $\Phi_1 = \hat{\phi}$ and $\Phi_2 = \hat{\pi}$.

decomposition

$$\hat{T} = i\frac{\lambda}{6}\int \frac{d^3p d^3q}{(2\pi)^6\sqrt{8E_pE_qE_{p+q}}}\frac{a_pa_qa_{-p-q} - a_p^\dagger a_q^\dagger a_{-p-q}^\dagger}{\sum E_i}\left(\phi_0 - \frac{(\ddot{\phi})_0}{(\sum E_i)^2}\right), \tag{4.62}$$

where coefficients have been fixed to generate the correct initial time divergences, as we are going to show. Notice that, at this order of perturbation theory (λ^2 and $\hbar^2$), we can use interchangeably E_k and ω_k to define $\hat{T}$. This stops being true if we extend our analysis to λ^3 divergences.

The order of appearance of the $\hat{T}$ and $\hat{S}$ in (4.62) is not arbitrary. In particular, when arranged in this way, correlation functions can be evaluated by first applying shifts and rotations as one would do with squeezed coherent states and *then* acting with the $\hat{T}$ operator. In other words, we can write

$$\langle C_T|\mathcal{O}[\hat{\phi},\hat{\pi}]|C_T\rangle = \langle\Omega|\phi_0 + e^{-i\hat{T}}\hat{\phi}_s e^{i\hat{T}},\ e^{-i\hat{T}}\hat{\pi}_s e^{i\hat{T}}|\Omega\rangle. \tag{4.63}$$

In contrast to the squeezing operator $\hat{S}$, where its effect can be resummed into ϕ_s, it is not possible to resum up the rotation induced by $\hat{T}$ into a closed form. Nevertheless, since we are interested in computing only two-loop corrections to the one-point function, we can expand the exponential operators in a series of commutators and consider only the first and second corrections (see Appendix A.1). With these, we can compute the first correction to the quadratic and cubic correlation function, finding

$$\langle T|\hat{\phi}^2|T\rangle_0 = \int\frac{d^3p}{(2\pi)^3 2E_p}\left\{1 - \frac{\lambda\langle\phi^2\rangle}{(2\omega_p)^2} + \lambda^2\int\frac{d^3q}{(2\pi)^3 8E_pE_qE_{p+q}}\left(\frac{\phi_0}{\sum E_i} - \frac{(\ddot{\phi})_0}{(\sum E_i)^3}\right)^2\right\}, \tag{4.64}$$

$$\langle T|\hat{\phi}^3|T\rangle_0 = -\lambda\int\frac{d^3p d^3q}{(2\pi)^6 4E_pE_qE_{p+q}}\frac{1}{\sum E_i}\left(\phi_0 - \frac{(\ddot{\phi})_0}{(\sum E_i)^3}\right). \tag{4.65}$$

Here, correlation functions are given at point coincidence and it can be shown that they are finite if evaluated at different points.

In the next part, we show that these initial time correlation functions have the appropriate behaviour to make the expectation value of the Hamiltonian and the 1-point function of the field operator finite. Before doing that, let us derive the action of the $\hat{T}$ operator on the creation operator a_p

$$(a_T)_p = a_p - \int\frac{d^3k_1}{(2\pi)^3}\,\gamma_{p,k_1}\,a_{k_1}^\dagger a_{-k_1-p}^\dagger + \\ + \int\frac{d^3k_1 d^3k_2}{(2\pi)^6}\,\gamma_{p,k_1}\gamma_{k_1,k_2}\left(a_{k_2}a_{k_1}a_{k_1+k_2-p}^\dagger + a_{k_1+k_2-p}^\dagger a_{k_1}a_{k_2}\right) + \ldots \tag{4.66}$$

Here, γ_{k_i,k_j} is a general momentum-dependent coefficient that parametrizes $\hat{T}$ (see again Appendix A.1). By analysing (4.66), it is evident that it is not possible to resume (4.66) in any particular form unless a specific form of γ_{k_i,k_j} is chosen. This is different to what takes place for the squeezing operator.

4.5.3 Solving the initial time singularity with $\hat{T}$

Finally, we show that the $\hat{T}$ operator provides the correct behaviour of the quadratic and cubic correlation functions to fix the initial time singularity sourced by the setting sun diagram, at two loops.

We show this in two steps, first by analysing the equation of motion of the field operator and then by checking the expectation value of the Hamiltonian. Concerning the first, we have

$$Z\partial_t^2\langle C_T|\hat{\phi}|C_T\rangle(t=0) = -\phi_0\left(Zm^2+\frac{\lambda}{2}\langle T|\hat{\phi}^2(x)|T\rangle_0\right)-\frac{\lambda Z^2}{3!}\phi_0^3-\frac{\lambda}{3!}\langle T|\hat{\phi}^3(x)|T\rangle_0\,. \tag{4.67}$$

Here, we can ignore the new correction to the quadratic correlation function, since its contribution is cubic in the coupling constant. By plugging in the cubic correlation function and focussing on divergent terms, we find

$$\begin{aligned} Z\partial_t^2\langle C_T|\hat{\phi}|C_T\rangle(t=0) = &-(\ddot{\phi})_0\left\{\frac{\lambda^2}{3!}\int\frac{d^3pd^3q}{(2\pi)^6 4E_pE_qE_{p+q}}\frac{1}{\left(E_p+E_q+E_{p+q}\right)^3}\right\}_{\phi_0=0}\\ -\phi_0\Bigg\{Zm^2+&\left(\frac{\lambda}{2}-\frac{\lambda^2}{2}\int\frac{d^3p}{(2\pi)^3(8E_p\omega_p^2)}\right)\langle\phi^2\rangle-\frac{\lambda^2}{3}\int\frac{d^3pd^3q}{(2\pi)^6 8E_pE_qE_{p+q}}\frac{1}{E_p+E_q+E_{p+q}}\Bigg\}_{\phi_0=0} \end{aligned} \tag{4.68}$$

We see that the second term of the first line corresponds to the wave function divergence and is removed by imposing the Z prescription (4.57). The same applies to the second line if we impose the physical mass prescription (4.58).

Similar to the squeezing operator, this result is not surprising since we fixed the $\hat{T}$ to provide all the initial time divergences that would make the equation of motion finite. The real deal is to check that the same state makes also the expectation value of the Hamiltonian finite. For that, let us start by considering

$$\begin{aligned} \langle C_T|\hat{H}|C_T\rangle = \int \mathrm{d}^3x\Bigg[&\frac{Z}{2}\left(m^2+\frac{\lambda}{2}\langle T|\hat{\phi}^2|T\rangle\right)\phi_0^2+\frac{\lambda Z^2}{4!}\phi_0^4+\frac{\lambda}{3!}\langle T|\hat{\phi}^3|T\rangle\phi_0+\\ &+\frac{1}{2}\langle T|\left\{\hat{\pi}^2+\left(\vec{\nabla}\hat{\phi}\right)^2+m^2\hat{\phi}^2+\frac{\lambda}{4!}\hat{\phi}^4\right\}|T\rangle\\ &-\frac{1}{2}\langle\Omega|\left\{\hat{\pi}^2+\left(\vec{\nabla}\hat{\phi}\right)^2+m^2\hat{\phi}^2+\frac{\lambda}{4!}\hat{\phi}^4\right\}|\Omega\rangle\Bigg]\,. \end{aligned} \tag{4.69}$$

At first glance, the cubic correlation function does not combine with the mass term as it does in the equation of motion, due to the different overall coefficient. Also, in the case of the Hamiltonian, we do not have any classical kinetic energy and the term proportional to $\ddot{\phi}_0$ remains unaddressed. However, in the case of (4.69), the second line provides a non-negligible contribu-

tion. By a direct evaluation, we have

$$\frac{1}{2}\langle T|\hat{\pi}^2 + \left(\vec{\nabla}\hat{\phi}\right)^2 + m^2\hat{\phi}^2|T\rangle = \frac{1}{2}\langle S|\hat{\pi}^2 + \left(\vec{\nabla}\hat{\phi}\right)^2 + m^2\hat{\phi}^2|S\rangle + \frac{\lambda^2\phi_0}{3!2}\int \frac{d^3p d^3q}{(2\pi)^6 8E_pE_qE_{p+q}}\frac{1}{\sum E_i}\left(\phi_0 - \frac{2(\ddot{\phi})_0}{(\sum E_i)^2}\right) + \text{(finite)} + \mathcal{O}(\lambda^3). \tag{4.70}$$

Once we plug the relation (4.70) in the expectation value of the Hamiltonian, we see that the mass divergence is generated with the correct coefficient, while terms proportional to $\ddot{\phi}$ drops out.

Chapter 5

Conclusions and Outlook

5.1 Dark Matter and Superfluidity

The first part of this thesis was devoted to understanding how collective effects, such as Bose-Einstein condensation and Superfluidity, could affect the dynamics of dark matter in halos. The guiding motivation is the mismatch between the dynamics of dark matter inferred by local observations and the one predicted by N-body simulations. An important tool we exploited is the Effective Field Theory of Superfluidity, in which the macroscopic properties of a superfluid are understood in terms of the Bose-Einstein condensation of its microscopic self-interacting constituents. After reviewing the theory, we investigated the relation between the quantum constituents of the condensate and phonons, the long-wavelength fluctuations of the superfluid background. In particular, we studied the matching between hard phonons and propagating constituent particles and exploited this property to evaluate the thermalization time of a gas of three-body interacting particles.

Then, following the papers [70, 78], we depicted the simplest theory of dark matter superfluidity, where a sub-eV scalar field endowed by repulsive self-interactions, is introduced as a potential dark matter candidate. In particular, we have shown that inner regions of galactic halos, where dark matter thermalization is efficient enough to trigger a superfluid phase transition, are unstable and prone to fragmenting in a collection of superfluid solitons due to Jeans instability. If parameters of the theory are chosen accordingly, these solitons can have a size which is slightly bigger than the kpc-scale. Also, if tidal effects are taken into account, most of the solitons which are not residing in the galactic centre would not survive tidal disruption and would be reshuffled in a fluid-like state that is not expected to rethermalize due to the peculiar structure of its phase space. The final density distribution of the halo is expected to be characterized by a quasi-homogeneous central region, surrounded by a coarse-grained NFW envelope and could explain both the core-cusp problem and the excess of substructures predicted by models of Cold Dark Matter.

There are several aspects of this first part of the thesis that require further investigation. An open question concerns the possibility of having a coupling between the superfluid component

and the baryonic sector along the line of [55, 90], able to generate a phonon-mediated force in the superfluid medium which is gravity-competing. Although it seems that these emergent forces can be effective in decelerating macroscopic probes [152], it could be interesting to make a theoretical analysis of what kind of coupling would be consistent with observations and what would not.

Finally, it would also be interesting to look for possible observational signatures associated with a superfluid phase of dark matter. An example is the suppression of dynamical friction experienced by orbiting probes moving in the superfluid background [77]. In the upcoming paper [153], we assess the role of dynamical friction in determining the dynamics of binary systems moving in a superfluid environment enhanced by a density spike. We show that the suppression of dynamical friction in these systems may help to discriminate between models of Cold Dark Matter and Superfluid Dark Matter.

5.2 Coherent states and Highly occupied systems

In the second part of the thesis, we studied coherent states in interacting quantum field theories. After reviewing the basic notions associated with this class of states, we studied the time evolution of the one-point function of the field operator in the theory of a real scalar field with quartic interactions.

In particular, we began by focusing on a non-squeezed coherent state describing a homogeneous configuration, corresponding to a condensate of zero momentum real bosons. We demonstrated that the amplitude of the one-point function of the field operator is damped if $\hbar\lambda^4$ quantum corrections are included, in contrast to the oscillatory behaviour of the solution to the classical equation of motion. We have shown this with two equivalent methods: by evaluating the one-point function of the field operator in the interaction picture and by applying the background field method. The root of this effect is the annihilation of four constituents of the condensate into two relativistic particles, which confirms the results of [108]. This is a pure quantum effect which strongly backreacts on the classical background after the time

$$t_{\rm depl} \sim \left(\frac{\lambda^4\phi_0^6}{m^5}\right)^{-1}, \tag{5.1}$$

which is identified with the *quantum break-time* of the system.

Finally, we investigated the problem of the initial time singularities. These are divergences that appear in the expectation value of the Hamiltonian and in the initial time field acceleration, and that cannot be removed by renormalizing the theory. To overcome this issue, specific properties have to be given to the state itself. We demonstrated that both non-squeezed and squeezed coherent states are affected by this class of divergences and that non-gaussian generalizations have to be considered.

The results obtained in this section can serve as the starting point for numerous additional investigations. For example, it would be interesting to study the implications of initial time

singularities in gauge theories, along the lines of [154]. In the context of a homogeneous background of $U(1)$-charged complex bosons, one might anticipate that the gauge field at the initial time should exhibit a shifted-mass prescription of the form

$$m_{\rm A}^2 \sim e^2\phi_0^2, \tag{5.2}$$

sourced by the scalar field background. Here, e is the gauge coupling of the theory.

It may also be interesting to see if the dynamical effects, such as the depletion of condensates due to quantum effects, are also present in gravity. For example, a follow-up work in this direction is the application of the background field method to study the dynamics of the de Sitter background, driven by a spectator scalar field ϕ. The aim is to understand if any time-dependent quantum correction to the one-point function of the metric appears at a certain order in quantum perturbation theory, indicating that the de Sitter solution is depleted by quantum effects in agreement with the predictions of [119, 122].

Appendix A

Appendix

A.1 Correlation functions over squeezed and non-Gaussian states

In this appendix, we explain the procedure to evaluate correlation functions, built using the states $|C\rangle$, $|S\rangle$ and $|T\rangle$.

We start by recalling a notable identity involving unitary operators. Let us consider the state $|U\rangle = e^{-i\hat{U}}|\Omega\rangle$, with $\hat{U}$ hermitian, and the general function of the field operator and conjugate momentum $\mathcal{O}(\hat{\phi}, \hat{\pi})$. Then, correlation functions satisfy the relation

$$\langle U|\mathcal{O}(\hat{\phi}, \hat{\pi})|U\rangle = \langle\Omega|e^{i\hat{U}}\mathcal{O}(\hat{\phi}, \hat{\pi})e^{-i\hat{U}}|\Omega\rangle = \langle\Omega|\mathcal{O}(e^{i\hat{U}}\hat{\phi}\, e^{-i\hat{U}}, e^{i\hat{U}}\hat{\pi}e^{-i\hat{U}})|\Omega\rangle. \tag{A.1}$$

In the last step, we expanded the general operator $\mathcal{O}(\hat{\phi}, \hat{\pi})$ in a series of the field and momentum, and inserted the combination $e^{i\hat{U}} \times e^{-i\hat{U}}$ in between every power of $\hat{\pi}$ and $\hat{\phi}$. Then, we resummed the series.

We see that the state $|U\rangle$ implements a rotation of the field operator and conjugate momentum, according to

$$\hat{\phi} \to e^{iU}\hat{\phi}\, e^{-iU}, \tag{A.2}$$

$$\hat{\pi} \to e^{iU}\hat{\pi}\, e^{-iU}. \tag{A.3}$$

These relations can be evaluated by applying the Baker–Campbell–Hausdorff formula as

$$e^{i\hat{U}}\,\hat{\phi}\, e^{-i\hat{U}} = \phi + [i\hat{U}, \hat{\phi}] + \frac{1}{2}[i\hat{U}, [i\hat{U}, \hat{\phi}]] + \frac{1}{3!}[i\hat{U}, [i\hat{U}, [i\hat{U}, \hat{\phi}]]] + ..., \tag{A.4}$$

and the same applies to the conjugate momentum.

Non-squeezed coherent state

By making explicit choices of $\hat{U}$, we can evaluate the series of commutators. For example, if we consider a $\hat{U}$ which is linear in the field operator, only the first commutator of the series (A.4) is non-null. This is the case of non-squeezed coherent states. We can see this explicitly by considering the specific operator

$$\hat{f} = \int d^3x\, \phi_0 \hat{\pi}, \tag{A.5}$$

and plugging it in the place of $\hat{U}$. The result reads

$$e^{i\hat{f}}\, \hat{\phi} e^{-i\hat{f}} = \phi_0 + \hat{\phi}, \tag{A.6}$$

reproducing the relation (4.7).

$\hat{S}$-state

If we choose an operator which is quadratic in the field and conjugate momentum, we have the case of the $|S\rangle$ state. Let us analyse this case explicitly by considering the following general realization of $\hat{S}$

$$\hat{S} = \frac{1}{2} \int \frac{d^3k}{(2\pi)^3} \left(\alpha_k\, a_k\, a_{-k} + \alpha_k^*\, a_k^\dagger\, a_{-k}^\dagger \right). \tag{A.7}$$

Here, we decided to work in momentum space for convenience. In this case, the series of commutators can be resummed into

$$\hat{\phi}_s = \int \frac{d^3k}{(2\pi)^3 \sqrt{2\omega_k}} \left\{ \left(\cosh|\alpha_k| + i \sinh|\alpha_k| e^{i\theta_k} \right) a_k + \left(\cosh|\alpha_k| - i \sinh|\alpha_k| e^{-i\theta_k} \right) a_{-k}^\dagger \right\} e^{ik\cdot x}, \tag{A.8}$$

$$\hat{\pi}_s = (-i) \int \frac{d^3k}{(2\pi)^3} \sqrt{\frac{\omega_k}{2}} \left\{ \left(\cosh|\alpha_k| - i \sinh|\alpha_k| e^{i\theta_k} \right) a_k - \left(\cosh|\alpha_k| + i \sinh|\alpha_k| e^{-i\theta_k} \right) a_{-k}^\dagger \right\} e^{ik\cdot x}, \tag{A.9}$$

with $\hat{\phi}_s = e^{i\hat{S}} \hat{\phi} e^{-i\hat{S}}$ and $\hat{\pi}_s = e^{i\hat{S}} \hat{\pi} e^{-i\hat{S}}$. Also, we decomposed $\alpha_k = |\alpha_k| e^{i\theta_k}$. Notice that if we choose

$$\alpha_k = \frac{i}{2} \log \frac{E_k}{\omega_k}, \tag{A.10}$$

the rotations (4.45) and (4.46) are reproduced.

$\hat{T}$-state

Finally, let us conclude the discussion by choosing an operator which is cubic in the number of fields

$$\hat{T} = \frac{1}{3} \int \frac{d^3k d^3k'}{(2\pi)^6} \left\{ \gamma_{k,k'}^* a_k^\dagger a_{k'}^\dagger a_{-k-k'}^\dagger + \gamma_{k,k'} a_k a_{k'} a_{-k-k'} \right\}. \tag{A.11}$$

Again, for convenience, we work in momentum space. In this case, the series of commutators cannot be resummed. Nevertheless, we may compute the first-order corrections to the quadratic and cubic correlation functions by evaluating the first two commutators of the series

$$\begin{aligned}\hat{\phi}_T =&\hat{\phi} + i\int \frac{d^3k d^3k'}{(2\pi)^6\sqrt{2\omega_k}}\left(\gamma_{k,k'}a_{k'}a_{-k-k'}e^{-ik\cdot x} - \gamma^*_{k,k'}e^{ik\cdot x}a^\dagger_{k'}a^\dagger_{-k-k'}\right)\\ &+\frac{1}{3}\int \frac{d^3k d^3k' d^3k''}{(2\pi)^6\sqrt{2\omega_k}}\gamma_{k,k'}\gamma^*_{k,k''}e^{ik\cdot x}\left(a^\dagger_{k''}a_{k'}a_{-K} + a_{k'}a^\dagger_{k''}a_{-K} + a_{k'}a_{-K}a^\dagger_{k''}\right) + \text{h.c} + \dots,\end{aligned} \tag{A.12}$$

with $\hat{\phi}_T = e^{i\hat{T}}\hat{\phi}e^{-i\hat{T}}$. This is the order of approximation we need for the two-loop analysis of Section 4.5.3.

Acknowledgements

First and foremost, I would like to express my profound gratitude to my supervisor, Lasha. I could have not overcome all the challenges in this journey without his guidance and advice. I am extremely grateful for all the insights he shared, both about physics and life in general. His office door was always open for me, always accompanied by his unique perspectives and advice on any problem I encountered[1]. I am also grateful to Gia Dvali for welcoming me into his group and giving me in this way the opportunity to pursue my research.

Next, I would like to thank all the people I had the chance to collaborate with, in particular Michael Zantedeschi[2], Valerio De Luca and Justin Khoury. I am honoured to have had the opportunity to learn so much from you.

Regarding all the wonderful people I had the privilege to meet in Munich, I am extremely thankful to Stefano de Nicola and Nazarena Tortorelli. Thank you for hosting me in your home when needed and sharing the food and wine[3] of your *'pacco da giù'* with me. If I endured the COVID-19 lockdown, it is also thanks to the wonderful diners we used to have. Thank you also for all the recipes that you patiently taught me and for welcoming me and guiding me in Naples.

A special thanks goes also to Angelo Caravano. Besides being a great colleague, I am grateful that I have found such an amazing friend. So thank you for all the fun, for all the scientific discussions and for your fried pizza[4]. And of course, I can only conclude this paragraph by quoting the famous phrase *'Viniii e Viniliii'*.

I also want to thank all the people I met at the MPP. A special thanks go to Anja Stuhlfauth, Giacomo Contri, Emmanouil Koutsangelas, Maximilian Bachmaier, Juan Sebastian Valbuena Bermudes, Ana Alexandre, Silvia Zanoli, Alessandro Ratti[5], Christian Biello, Luc Schnell, Gabriël Koole, Joachim Weiss, Amando Hala, Anna Bertolini, Francesca Pucci and Johanness Diehl. Thank you for adopting me for lunch and for our countless coffee breaks together. Also,

[1] It is a matter of fact that every time I would plan to stop by, I would find Lasha in the process of eating his Quark. The astonishing correlation between these events requires further investigations.

[2] Thank youuuuu Michael!

[3] A special thanks goes to Dino, for his amazing *mirto* and wine.

[4] However, I don't want to thank you for sleeping on my couch for three months and breaking it just before moving out.

[5] Let me also thank Alessandro's shoulders, which have recently reached the critical mass for being recognised as a self-determined being.

a special thanks goes to my office mate Manuel Ettengruber who endured the pain of hearing my outbursts of frustration while evaluating correlation functions. Thank you for your patience and for all the chess games.

Last but certainly not least, I want to express my gratitude to all my friends scattered across Italy. Your support and your consistent presence when I return, bridging the gap of the months I have spent abroad, mean the world to me. And, of course, a special thanks is reserved for my family. To my sister, Francesca, whose determination to pursue her dreams continues to inspire me. To my parents, Dana and Fabrizio, whose support throughout these years made all of this possible.

Bibliography

[1] N. Aghanim et al. Planck 2018 results. VI. Cosmological parameters. *Astron. Astrophys.*, 641:A6, 2020. [Erratum: Astron.Astrophys. 652, C4 (2021)].

[2] N. Aghanim et al. Planck 2018 results. I. Overview and the cosmological legacy of Planck. *Astron. Astrophys.*, 641:A1, 2020.

[3] James S. Bullock and Michael Boylan-Kolchin. Small-Scale Challenges to the ΛCDM Paradigm. *Ann. Rev. Astron. Astrophys.*, 55:343–387, 2017.

[4] G. L. Bryan and M. L. Norman. Statistical properties of x-ray clusters: Analytic and numerical comparisons. *Astrophys. J.*, 495:80, 1998.

[5] Julio F. Navarro, Aaron Ludlow, Volker Springel, Jie Wang, Mark Vogelsberger, Simon D. M. White, Adrian Jenkins, Carlos S. Frenk, and Amina Helmi. The Diversity and Similarity of Cold Dark Matter Halos. *Mon. Not. Roy. Astron. Soc.*, 402:21, 2010.

[6] Julio F. Navarro, Carlos S. Frenk, and Simon D. M. White. The Structure of cold dark matter halos. *Astrophys. J.*, 462:563–575, 1996.

[7] Aaron A. Dutton and Andrea V. Macciò. Cold dark matter haloes in the Planck era: evolution of structural parameters for Einasto and NFW profiles. *Mon. Not. Roy. Astron. Soc.*, 441(4):3359–3374, 2014.

[8] B. Moore, T. Quinn, F. Governato, J. Stadel, and G. Lake. Cold collapse and the core catastrophe. *Monthly Notices of the Royal Astronomical Society*, 310(4):1147–1152, 12 1999.

[9] Jaan Einasto. On the construction of a composite model for the galaxy and on the determination of the system of galactic parameters. *Trudy Astrofizicheskogo Instituta Alma-Ata, Vol. 5, p. 87-100, 1965*, 5:87–100, 1965.

[10] Aggeliki Kassiola and Israel Kovner. Elliptic mass distributions versus elliptic potentials in gravitational lenses. *Astrophysical Journal v. 417, p. 450*, 417:450, 1993.

[11] Walter Jaffe. A simple model for the distribution of light in spherical galaxies. *Monthly Notices of the Royal Astronomical Society*, 202(4):995–999, 1983.

[12] Kyle A. Oman et al. The unexpected diversity of dwarf galaxy rotation curves. *Mon. Not. Roy. Astron. Soc.*, 452(4):3650–3665, 2015.

[13] Romain Teyssier, Andrew Pontzen, Yohan Dubois, and Justin I. Read. Cusp-core transformations in dwarf galaxies: observational predictions. *Monthly Notices of the Royal Astronomical Society*, 429(4):3068–3078, 01 2013.

[14] Piero Madau, Sijing Shen, and Fabio Governato. Dark Matter Heating and Early Core Formation in Dwarf Galaxies. *Astrophys. J. Lett.*, 789:L17, 2014.

[15] Jose Oñ orbe, Michael Boylan-Kolchin, James S. Bullock, Philip F. Hopkins, Dušan Kerěs, Claude-André Faucher-Giguère, Eliot Quataert, and Norman Murray. Forged in FIRE: cusps, cores, and baryons in low-mass dwarf galaxies. *Mon. Not. Roy. Astron. Soc.*, 454(2):2092–2106, 2015.

[16] J. I. Read, O. Agertz, and M. L. M. Collins. Dark matter cores all the way down. *Monthly Notices of the Royal Astronomical Society*, 459(3):2573–2590, 03 2016.

[17] Sergey Mashchenko, H. M. P. Couchman, and James Wadsley. The removal of cusps from galaxy centres by stellar feedback in the early Universe. *Nature*, 442(7102):539–542, August 2006.

[18] F. Governato, C. Brook, L. Mayer, A. Brooks, G. Rhee, J. Wadsley, P. Jonsson, B. Willman, G. Stinson, T. Quinn, and P. Madau. Bulgeless dwarf galaxies and dark matter cores from supernova-driven outflows. *Nature*, 463(7278):203–206, January 2010.

[19] F. Governato, A. Zolotov, A. Pontzen, C. Christensen, S. H. Oh, A. M. Brooks, T. Quinn, S. Shen, and J. Wadsley. Cuspy no more: how outflows affect the central dark matter and baryon distribution in Λ cold dark matter galaxies. *Monthly Notices of the Royal Astronomical Society*, 422(2):1231–1240, 04 2012.

[20] C. B. Brook, G. Stinson, B. K. Gibson, J. Wadsley, and T. Quinn. MaGICC discs: matching observed galaxy relationships over a wide stellar mass range. *Monthly Notices of the Royal Astronomical Society*, 424(2):1275–1283, 08 2012.

[21] Arianna Di Cintio, Chris B. Brook, Andrea V. Macciò, Greg S. Stinson, Alexander Knebe, Aaron A. Dutton, and James Wadsley. The dependence of dark matter profiles on the stellar-to-halo mass ratio: a prediction for cusps versus cores. *Monthly Notices of the Royal Astronomical Society*, 437(1):415–423, 11 2013.

[22] A. Burkert. The Structure of dark matter halos in dwarf galaxies. *Astrophys. J. Lett.*, 447:L25, 1995.

[23] V. Springel, J. Wang, M. Vogelsberger, A. Ludlow, A. Jenkins, A. Helmi, J. F. Navarro, C. S. Frenk, and S. D. M. White. The Aquarius Project: the subhaloes of galactic haloes. *Monthly Notices of the Royal Astronomical Society*, 391(4):1685–1711, 12 2008.

[24] Michael Kuhlen, Piero Madau, and Joseph Silk. Exploring dark matter with milky way substructure. *Science*, 325(5943):970–973, aug 2009.

[25] Brendan F. Griffen, Alexander P. Ji, Gregory A. Dooley, Facundo A. Gó mez, Mark Vogelsberger, Brian W. O'Shea, and Anna Frebel. The Caterpillar Project: A Large Suite Of Milky Way Sized Halos. *The Astrophysical Journal*, 818(1):10, feb 2016.

[26] Victor H. Robles, Tyler Kelley, James S. Bullock, and Manoj Kaplinghat. The Milky Way's halo and subhaloes in self-interacting dark matter. *Mon. Not. Roy. Astron. Soc.*, 490(2):2117–2123, 2019.

[27] A. Drlica-Wagner et al. Eight Ultra-faint Galaxy Candidates Discovered in Year Two of the Dark Energy Survey. *Astrophys. J.*, 813(2):109, 2015.

[28] A. J. Benson, C. S. Frenk, Cedric G. Lacey, C. M. Baugh, and S. Cole. The effects of photoionization on galaxy formation. 2. Satellites in the local group. *Mon. Not. Roy. Astron. Soc.*, 333:177, 2002.

[29] Sergey Koposov, Jaiyul Yoo, Hans-Walter Rix, David Weinberg, Andrea Macciò, and Jordi Miralda-Escudé. A quantitative explanation of the observed population of milky way satellite galaxies. *The Astrophysical Journal*, 696:2179, 04 2009.

[30] Joseph A. Muñoz, Piero Madau, Abraham Loeb, and Jürg Diemand. Probing the epoch of reionization with Milky Way satellites. *Monthly Notices of the Royal Astronomical Society*, 400(3):1593–1602, December 2009.

[31] Yang-Shyang Li, Gabriella De Lucia, and Amina Helmi. On the nature of the Milky Way satellites. *Monthly Notices of the Royal Astronomical Society*, 401(3):2036–2052, 01 2010.

[32] Andrea V. Macciò, Xi Kang, Fabio Fontanot, Rachel S. Somerville, Sergey Koposov, and Pierluigi Monaco. Luminosity function and radial distribution of Milky Way satellites in a ΛCDM Universe. *Monthly Notices of the Royal Astronomical Society*, 402(3):1995–2008, 02 2010.

[33] Qi Guo, Simon White, Michael Boylan-Kolchin, Gabriella De Lucia, Guinevere Kauffmann, Gerard Lemson, Cheng Li, Volker Springel, and Simone Weinmann. From dwarf spheroidals to cD galaxies: simulating the galaxy population in a ΛCDM cosmology. *Monthly Notices of the Royal Astronomical Society*, 413(1):101–131, 04 2011.

[34] Richard B Larson. Effects of supernovae on the early evolution of galaxies. *Monthly Notices of the Royal Astronomical Society*, 169(2):229–245, 1974.

[35] A. Dekel and J. Silk. The Origin of Dwarf Galaxies, Cold Dark Matter, and Biased Galaxy Formation. *The Astrophysical Journal*, 303:39, April 1986.

[36] G. Efstathiou. Suppressing the formation of dwarf galaxies via photoionization. *Monthly Notices of the Royal Astronomical Society*, 256(2):43P–47P, May 1992.

[37] Anne A. Thoul and David H. Weinberg. Hydrodynamic Simulations of Galaxy Formation. II. Photoionization and the Formation of Low-Mass Galaxies. *The Astrophysical Journal*, 465:608, July 1996.

[38] Rennan Barkana and Abraham Loeb. The photoevaporation of dwarf galaxies during reionization. *Astrophys. J.*, 523:54, 1999.

[39] Nickolay Y. Gnedin. Effect of reionization on the structure formation in the universe. *Astrophys. J.*, 542:535–541, 2000.

[40] Matthias Hoeft, Gustavo Yepes, Stefan Gottlober, and Volker Springel. Dwarf galaxies in voids: Suppressing star formation with photo-heating. *Mon. Not. Roy. Astron. Soc.*, 371:401–414, 2006.

[41] Takashi Okamoto, Liang Gao, and Tom Theuns. Mass loss of galaxies due to an ultraviolet background. *Monthly Notices of the Royal Astronomical Society*, 390(3):920–928, 10 2008.

[42] Michael Boylan-Kolchin, James S. Bullock, and Manoj Kaplinghat. The Milky Way's bright satellites as an apparent failure of ΛCDM. *Monthly Notices of the Royal Astronomical Society*, 422(2):1203–1218, 04 2012.

[43] Emmanouil Papastergis and Francesco Shankar. An assessment of the "too big to fail" problem for field dwarf galaxies in view of baryonic feedback effects. *Astronomy & Astrophysics*, 591:A58, 2016.

[44] Stacy S. McGaugh. The Baryonic Tully-Fisher Relation of Gas Rich Galaxies as a Test of ΛCDM and MOND. *The Astronomical Journal*, 143(2):40, jan 2012.

[45] B. Keller and J. Wadsley. ΛCDM is Consistent with SPARC Radial Acceleration Relation. *The Astrophysical Journal*, 835:L17, 01 2017.

[46] David N. Spergel and Paul J. Steinhardt. Observational evidence for selfinteracting cold dark matter. *Phys. Rev. Lett.*, 84:3760–3763, 2000.

[47] Ayuki Kamada, Manoj Kaplinghat, Andrew B. Pace, and Hai-Bo Yu. How the Self-Interacting Dark Matter Model Explains the Diverse Galactic Rotation Curves. *Phys. Rev. Lett.*, 119(11):111102, 2017.

[48] Peter Creasey, Omid Sameie, Laura V. Sales, Hai-Bo Yu, Mark Vogelsberger, and Jesú s Zavala. Spreading out and staying sharp – creating diverse rotation curves via baryonic and self-interaction effects. *Monthly Notices of the Royal Astronomical Society*, 468(2):2283–2295, mar 2017.

[49] Tao Ren, Anna Kwa, Manoj Kaplinghat, and Hai-Bo Yu. Reconciling the Diversity and Uniformity of Galactic Rotation Curves with Self-Interacting Dark Matter. *Phys. Rev. X*, 9(3):031020, 2019.

[50] Wayne Hu, Rennan Barkana, and Andrei Gruzinov. Cold and fuzzy dark matter. *Phys. Rev. Lett.*, 85:1158–1161, 2000.

[51] Lam Hui, Jeremiah P. Ostriker, Scott Tremaine, and Edward Witten. Ultralight scalars as cosmological dark matter. *Phys. Rev. D*, 95(4):043541, 2017.

[52] Simon May and Volker Springel. Structure formation in large-volume cosmological simulations of fuzzy dark matter: impact of the non-linear dynamics. *Mon. Not. Roy. Astron. Soc.*, 506(2):2603–2618, 2021.

[53] Simon May and Volker Springel. The halo mass function and filaments in full cosmological simulations with fuzzy dark matter. *Mon. Not. Roy. Astron. Soc.*, 524(3):4256–4274, 2023.

[54] Jeremy Goodman. Repulsive dark matter. *New Astron.*, 5:103, 2000.

[55] Lasha Berezhiani and Justin Khoury. Theory of dark matter superfluidity. *Phys. Rev. D*, 92:103510, 2015.

[56] Lasha Berezhiani, Benoit Famaey, and Justin Khoury. Phenomenological consequences of superfluid dark matter with baryon-phonon coupling. *JCAP*, 09:021, 2018.

[57] P. Kapitza. Viscosity of Liquid Helium below the λ-Point. *Nature*, 141(3558):74–74, 1938.

[58] J. F. ALLEN and A. D. MISENER. Flow Phenomena in Liquid Helium II. *Nature*, 142(3597):643–644, 1938.

[59] F. LONDON. The λ-Phenomenon of Liquid Helium and the Bose-Einstein Degeneracy. *Nature*, 141(3571):643–644, 1938.

[60] Sébastien Balibar. Laszlo Tisza and the two-fluid model of superfluidity. *Comptes Rendus Physique*, 18(9):586–591, 2017. Science in the making: The Comptes rendus de l'Académie des sciences throughout history.

[61] L. TISZA. Transport Phenomena in Helium II. *Nature*, 141(3577):913–913, 1938.

[62] L. Landau. Theory of the Superfluidity of Helium II. *Phys. Rev.*, 60:356–358, Aug 1941.

[63] N. N. Bogolyubov. On the theory of superfluidity. *J. Phys. (USSR)*, 11:23–32, 1947.

[64] Andreas Schmitt. *Introduction to superfluidity: Field-theoretical approach and applications*, volume 888. Springer, 2015.

[65] Justin Khoury. Dark Matter Superfluidity. *SciPost Phys. Lect. Notes*, 42:1, 2022.

[66] Jeremy Bernstein and Scott Dodelson. Relativistic bose gas. *Phys. Rev. Lett.*, 66:683–686, Feb 1991.

[67] D. T. Son. Low-energy quantum effective action for relativistic superfluids. *arXiv preprint hep-ph/0204199*, 2002.

[68] Alberto Nicolis. Low-energy effective field theory for finite-temperature relativistic superfluids. *arXiv preprint arXiv:1108.2513*, 2011.

[69] Lasha Berezhiani. On effective theory of superfluid phonons. *Phys. Lett. B*, 805:135451, 2020.

[70] Lasha Berezhiani, Giordano Cintia, and Justin Khoury. Thermalization, fragmentation, and tidal disruption: The complex galactic dynamics of dark matter superfluidity. *Physical Review D*, 107(12):123010, 2023.

[71] Francesca Acanfora, Angelo Esposito, and Antonio D. Polosa. Sub-GeV Dark Matter in Superfluid He-4: an Effective Theory Approach. *Eur. Phys. J. C*, 79(7):549, 2019.

[72] P. Sikivie and Q. Yang. Bose-Einstein Condensation of Dark Matter Axions. *Phys. Rev. Lett.*, 103:111301, 2009.

[73] Alan H. Guth, Mark P. Hertzberg, and C. Prescod-Weinstein. Do Dark Matter Axions Form a Condensate with Long-Range Correlation? *Phys. Rev. D*, 92(10):103513, 2015.

[74] Manoj Kaplinghat, Sean Tulin, and Hai-Bo Yu. Dark Matter Halos as Particle Colliders: Unified Solution to Small-Scale Structure Puzzles from Dwarfs to Clusters. *Phys. Rev. Lett.*, 116(4):041302, 2016.

[75] O. Erken, P. Sikivie, H. Tam, and Q. Yang. Cosmic axion thermalization. *Phys. Rev. D*, 85:063520, 2012.

[76] D. T. Son and M. Wingate. General coordinate invariance and conformal invariance in nonrelativistic physics: Unitary Fermi gas. *Annals Phys.*, 321:197–224, 2006.

[77] Lasha Berezhiani, Benjamin Elder, and Justin Khoury. Dynamical Friction in Superfluids. *JCAP*, 10:074, 2019.

[78] Lasha Berezhiani, Giordano Cintia, and Max Warkentin. Core fragmentation in simplest superfluid dark matter scenario. *Phys. Lett. B*, 819:136422, 2021.

[79] Elisa G. M. Ferreira. Ultra-light dark matter. *Astron. Astrophys. Rev.*, 29(1):7, 2021.

[80] Tomer D. Yavetz, Xinyu Li, and Lam Hui. Construction of wave dark matter halos: Numerical algorithm and analytical constraints. *Phys. Rev. D*, 105(2):023512, 2022.

[81] I-Kang Liu, Nick P. Proukakis, and Gerasimos Rigopoulos. Coherent and incoherent structures in fuzzy dark matter haloes. *Mon. Not. Roy. Astron. Soc.*, 521(3):3625–3647, 2023.

[82] D. Lynden-Bell, Roger Wood, and Astronomer Royal. The Gravo-Thermal Catastrophe in Isothermal Spheres and the Onset of Red-Giant Structure for Stellar Systems. *Monthly Notices of the Royal Astronomical Society*, 138(4):495–525, 02 1968.

[83] Jun Koda and Paul R. Shapiro. Gravothermal collapse of isolated self-interacting dark matter haloes: N-body simulation versus the fluid model. *Monthly Notices of the Royal Astronomical Society*, 415(2):1125–1137, jun 2011.

[84] Zachary Slepian and Jeremy Goodman. Ruling Out Bosonic Repulsive Dark Matter in Thermal Equilibrium. *Mon. Not. Roy. Astron. Soc.*, 427:839, 2012.

[85] Anushrut Sharma, Justin Khoury, and Tom Lubensky. The Equation of State of Dark Matter Superfluids. *JCAP*, 05:054, 2019.

[86] Anushrut Sharma, Guram Kartvelishvili, and Justin Khoury. Finite temperature description of an interacting Bose gas. *Phys. Rev. D*, 106(4):045025, 2022.

[87] M. Milgrom. A modification of the Newtonian dynamics as a possible alternative to the hidden mass hypothesis. *The Astrophysical Journal*, 270:365–370, July 1983.

[88] M. Milgrom. A modification of the Newtonian dynamics - Implications for galaxies. *The Astrophysical Journal*, 270:371–383, July 1983.

[89] M. Milgrom. A modification of the newtonian dynamics : implications for galaxy systems. *The Astrophysical Journal*, 270:384–389, July 1983.

[90] Lasha Berezhiani and Justin Khoury. Emergent long-range interactions in Bose-Einstein Condensates. *Phys. Rev. D*, 99(7):076003, 2019.

[91] James Binney and Scott Tremaine. *Galactic Dynamics, Second Edition*. Princeton University Press, Princeton, 2008.

[92] Pierre-Henri Chavanis. Mass-radius relation of newtonian self-gravitating bose-einstein condensates with short-range interactions. i. analytical results. *Physical Review D*, 84(4), aug 2011.

[93] E. Madelung. Quantentheorie in hydrodynamischer Form. *Zeitschrift fur Physik*, 40(3-4):322–326, March 1927.

[94] S. Chandrasekhar and S. Chandrasekhar. *An Introduction to the Study of Stellar Structure*. Astrophysical monographs. Dover Publications, 1957.

[95] Vid Iršič, Matteo Viel, Martin G. Haehnelt, James S. Bolton, and George D. Becker. First constraints on fuzzy dark matter from Lyman-α forest data and hydrodynamical simulations. *Phys. Rev. Lett.*, 119(3):031302, 2017.

[96] Keir K. Rogers and Hiranya V. Peiris. Strong Bound on Canonical Ultralight Axion Dark Matter from the Lyman-Alpha Forest. *Phys. Rev. Lett.*, 126(7):071302, 2021.

[97] Eric Armengaud, Nathalie Palanque-Delabrouille, Christophe Yèche, David J. E. Marsh, and Julien Baur. Constraining the mass of light bosonic dark matter using SDSS Lyman-α forest. *Mon. Not. Roy. Astron. Soc.*, 471(4):4606–4614, 2017.

[98] Michael Kesden and Marc Kamionkowski. Tidal Tails Test the Equivalence Principle in the Dark Sector. *Phys. Rev. D*, 74:083007, 2006.

[99] Noah Glennon, Ethan O. Nadler, Nathan Musoke, Arka Banerjee, Chanda Prescod-Weinstein, and Risa H. Wechsler. Tidal disruption of solitons in self-interacting ultralight axion dark matter. *Phys. Rev. D*, 105(12):123540, 2022.

[100] Maxim Markevitch, A. H. Gonzalez, D. Clowe, A. Vikhlinin, L. David, W. Forman, C. Jones, S. Murray, and W. Tucker. Direct constraints on the dark matter self-interaction cross-section from the merging galaxy cluster 1E0657-56. *Astrophys. J.*, 606:819–824, 2004.

[101] Scott W. Randall, Maxim Markevitch, Douglas Clowe, Anthony H. Gonzalez, and Marusa Bradac. Constraints on the Self-Interaction Cross-Section of Dark Matter from Numerical Simulations of the Merging Galaxy Cluster 1E 0657-56. *Astrophys. J.*, 679:1173–1180, 2008.

[102] Felix Kahlhoefer, Kai Schmidt-Hoberg, Mads T. Frandsen, and Subir Sarkar. Colliding clusters and dark matter self-interactions. *Mon. Not. Roy. Astron. Soc.*, 437(3):2865–2881, 2014.

[103] Douglas Clowe, Anthony Gonzalez, and Maxim Markevitch. Weak lensing mass reconstruction of the interacting cluster 1E0657-558: Direct evidence for the existence of dark matter. *Astrophys. J.*, 604:596–603, 2004.

[104] John Preskill, Mark B. Wise, and Frank Wilczek. Cosmology of the Invisible Axion. *Phys. Lett. B*, 120:127–132, 1983.

[105] L. F. Abbott and P. Sikivie. A Cosmological Bound on the Invisible Axion. *Phys. Lett. B*, 120:133–136, 1983.

[106] Michael Dine and Willy Fischler. The Not So Harmless Axion. *Phys. Lett. B*, 120:137–141, 1983.

[107] S. T. H. Hartman, H. A. Winther, and D. F. Mota. Constraints on self-interacting Bose-Einstein condensate dark matter using large-scale observables. *JCAP*, 02(02):005, 2022.

[108] Gia Dvali and Sebastian Zell. Classicality and Quantum Break-Time for Cosmic Axions. *JCAP*, 07:064, 2018.

[109] Gia Dvali, Cesar Gomez, and Sebastian Zell. Quantum Break-Time of de Sitter. *JCAP*, 06:028, 2017.

[110] Lasha Berezhiani, Giordano Cintia, and Michael Zantedeschi. Background-field method and initial-time singularity for coherent states. *Phys. Rev. D*, 105(4):045003, 2022.

[111] Kyle A. Oman, Julio F. Navarro, Azadeh Fattahi, Carlos S. Frenk, Till Sawala, Simon D. M. White, Richard Bower, Robert A. Crain, Michelle Furlong, Matthieu Schaller, Joop Schaye, and Tom Theuns. The unexpected diversity of dwarf galaxy rotation curves. *Monthly Notices of the Royal Astronomical Society*, 452(4):3650–3665, 08 2015.

[112] Peter S. Behroozi, Risa H. Wechsler, and Charlie Conroy. The Average Star Formation Histories of Galaxies in Dark Matter Halos from z=0-8. *The Astrophysical Journal*, 770(1):57, may 2013.

[113] Mark Vogelsberger, Jesus Zavala, and Abraham Loeb. Subhaloes in self-interacting galactic dark matter haloes. *Monthly Notices of the Royal Astronomical Society*, 423(4):3740–3752, may 2012.

[114] D. Boyanovsky, M. D'Attanasio, H. J. de Vega, R. Holman, and D. S. Lee. New aspects of reheating. *NATO Sci. Ser. C*, 476:451–491, 1996.

[115] Jurgen Baacke, Katrin Heitmann, and Carsten Patzold. On the choice of initial states in nonequilibrium dynamics. *Phys. Rev. D*, 57:6398–6405, 1998.

[116] Gia Dvali and Cesar Gomez. Black Hole's Quantum N-Portrait. *Fortsch. Phys.*, 61:742–767, 2013.

[117] Gia Dvali and Cesar Gomez. Black Holes as Critical Point of Quantum Phase Transition. *Eur. Phys. J. C*, 74:2752, 2014.

[118] Gia Dvali and Cesar Gomez. Black hole macro-quantumness. *arXiv preprint arXiv:1212.0765*, 2012.

[119] Gia Dvali and Cesar Gomez. Quantum Compositeness of Gravity: Black Holes, AdS and Inflation. *JCAP*, 01:023, 2014.

[120] Lasha Berezhiani. On Corpuscular Theory of Inflation. *Eur. Phys. J. C*, 77(2):106, 2017.

[121] A. M. Polyakov. De Sitter space and eternity. *Nucl. Phys. B*, 797:199–217, 2008.

[122] A. M. Polyakov. Infrared instability of the de Sitter space. *arXiv preprint arXiv:1209.4135*, 2012.

[123] Lasha Berezhiani and Mark Trodden. How Likely are Constituent Quanta to Initiate Inflation? *Phys. Lett. B*, 749:425–430, 2015.

[124] Lasha Berezhiani and Mark Trodden. A relativistic gas of inflatons as an initial state for inflation. *Phys. Lett. B*, 840:137852, 2023.

[125] Gia Dvali, Daniel Flassig, Cesar Gomez, Alexander Pritzel, and Nico Wintergerst. Scrambling in the Black Hole Portrait. *Phys. Rev. D*, 88(12):124041, 2013.

[126] A Kovtun and M Zantedeschi. Breaking BEC: the fast and the quantum. *Physical Review D*, 105(8):085019, 2022.

[127] A. Kovtun and M. Zantedeschi. Breaking BEC. *JHEP*, 07:212, 2020.

[128] Gia Dvali and Mischa Panchenko. Black hole type quantum computing in critical bose-einstein systems. 2015.

[129] Gia Dvali. A Microscopic Model of Holography: Survival by the Burden of Memory. 10 2018.

[130] Gia Dvali, Lukas Eisemann, Marco Michel, and Sebastian Zell. Black hole metamorphosis and stabilization by memory burden. *Phys. Rev. D*, 102(10):103523, 2020.

[131] J. Bardeen, L. N. Cooper, and J. R. Schrieffer. Theory of Superconductivity. *Phys. Rev.*, 108:1175–1204, Dec 1957.

[132] Juergen Berges. Introduction to nonequilibrium quantum field theory. *AIP Conf. Proc.*, 739(1):3–62, 2004.

[133] Esteban A. Calzetta and Bei-Lok B. Hu. *Nonequilibrium Quantum Field Theory*. Oxford University Press, 2009.

[134] Lasha Berezhiani, Giordano Cintia, and Michael Zantedeschi. To appear.

[135] E. Schrödinger. Der stetige Übergang von der Mikro- zur Makromechanik. *Naturwissenschaften*, 14(28):664–666, July 1926.

[136] Roy J. Glauber. Coherent and Incoherent States of the Radiation Field. *Phys. Rev.*, 131:2766–2788, Sep 1963.

[137] Wei-Min Zhang, Da Hsuan Feng, and Robert Gilmore. Coherent states: Theory and some applications. *Rev. Mod. Phys.*, 62:867–927, Oct 1990.

[138] Wei-Min Zhang. Coherent states in field theory. *arXiv preprint hep-th/9908117*, 1999.

[139] Lasha Berezhiani and Michael Zantedeschi. Evolution of coherent states as quantum counterpart of classical dynamics. *Phys. Rev. D*, 104(8):085007, 2021.

[140] Tanmay Vachaspati. Quantum backreaction on classical dynamics. *Phys. Rev. D*, 95:125002, Jun 2017.

[141] Gia Dvali and Lukas Eisemann. Perturbative understanding of nonperturbative processes and quantumization versus classicalization. *Phys. Rev. D*, 106(12):125019, 2022.

[142] Michael Edward Peskin and Daniel V. Schroeder. *An Introduction to Quantum Field Theory*. Westview Press, 1995. Reading, USA: Addison-Wesley (1995) 842 p.

[143] E. C. G. Stueckelberg. Relativistic Quantum Theory for Finite Time Intervals. *Phys. Rev.*, 81:130–133, Jan 1951.

[144] N. N. Bogolyubov and D. V. Shirkov. *Introduction to the theory of quantized fields*, volume 3. 1959.

[145] Fred Cooper and Emil Mottola. Initial-value problems in quantum field theory in the large-n approximation. *Phys. Rev. D*, 36:3114–3127, Nov 1987.

[146] D. Boyanovsky, H. J. de Vega, R. Holman, and M. Simionato. Dynamical renormalization group resummation of finite temperature infrared divergences. *Phys. Rev. D*, 60:065003, Aug 1999.

[147] J. Baacke, D. Boyanovsky, and H. J. de Vega. Initial time singularities in nonequilibrium evolution of condensates and their resolution in the linearized approximation. *Phys. Rev. D*, 63:045023, Jan 2001.

[148] Hael Collins and R Holman. An Effective theory of initial conditions in inflation. *arXiv preprint hep-th/0507081*, 2005.

[149] Viatcheslav Mukhanov and Sergei Winitzki. *Introduction to Quantum Effects in Gravity*. Cambridge University Press, 2007.

[150] Sidney Coleman and Erick Weinberg. Radiative Corrections as the Origin of Spontaneous Symmetry Breaking. *Phys. Rev. D*, 7:1888–1910, Mar 1973.

[151] Pierre Ramond. *FIELD THEORY. A MODERN PRIMER*, volume 51. 1981.

[152] Tobias Mistele. A novel cherenkov radiation constraint for hybrid mond dark matter models. *arXiv preprint arXiv:2208.14308*, 2022.

[153] Lasha Berezhiani, Giordano Cintia, Justin Khoury, and Valerio De Luca. Dynamical friction in dark matter superfluids: The evolution of black hole binaries, To appear.

[154] Lasha Berezhiani, Gia Dvali, and Otari Sakhelashvili. de Sitter space as a BRST invariant coherent state of gravitons. *Phys. Rev. D*, 105(2):025022, 2022.